The Cryosphere

Using ice core measurements from Taylor Glacier, Antarctica, to calibrate in situ cosmogenic ^{14}C production rates by muons

Michael N. Dyonisius[1,2], Vasilii V. Petrenko[1], Andrew M. Smith[3], Benjamin Hmiel[1,a], Peter D. Neff[4,1], Bin Yang[3], Quan Hua[3], Jochen Schmitt[5], Sarah A. Shackleton[6,b], Christo Buizert[7], Philip F. Place[1,c], James A. Menking[7,d], Ross Beaudette[6], Christina Harth[6], Michael Kalk[7], Heidi A. Roop[4], Bernhard Bereiter[6], Casey Armanetti[7,e], Isaac Vimont[8,f], Sylvia Englund Michel[8], Edward J. Brook[7], Jeffrey P. Severinghaus[6], Ray F. Weiss[6], and Joseph R. McConnell[9]

[1]Department of Earth and Environmental Sciences, University of Rochester, Rochester, NY 14627, USA
[2]Physics of Ice, Climate, and Earth, Niels Bohr Institute, University of Copenhagen, Copenhagen 2200, Denmark
[3]Centre for Accelerator Science (CAS), Australian Nuclear Science and Technology Organization (ANSTO), Lucas Heights, NSW 2234, Australia
[4]Department of Soil, Water, and Climate, University of Minnesota, Saint Paul, MN 55108, USA
[5]Climate and Environmental Physics, Physics Institute and Oeschger Centre for Climate Change Research, University of Bern, 3012 Bern, Switzerland
[6]Scripps Institution of Oceanography (SIO), University of California, San Diego, La Jolla, CA 92037, USA
[7]College of Earth, Ocean and Atmospheric Sciences, Oregon State University, Corvallis, OR 97331, USA
[8]Institute of Arctic and Alpine Research, University of Colorado Boulder, Boulder, CO 80303, USA
[9]Division of Hydrologic Science, Desert Research Institute, Reno, NV 89512, USA
[a]present address: Environmental Defense Fund, Austin, TX, USA
[b]present address: Department of Geosciences, Princeton University, Princeton, NJ 08544, USA
[c]present address: University Instrumentation Center, University of New Hampshire, Durham, NH 03824, USA
[d]present address: Australian Antarctic Partnership Program, University of Tasmania, Hobart, Tasmania, Australia
[e]present address: Graduate School of Design, Harvard University, Cambridge, MA, USA
[f]present address: National Oceanic and Atmospheric Administration, Global Monitoring Division, Boulder, CO, USA

Correspondence: Michael N. Dyonisius (michael.dyonisius@nbi.ku.dk)

Abstract. Cosmic rays entering the Earth's atmosphere produce showers of secondary particles such as protons, neutrons, and muons. The interaction of these particles with oxygen-16 (^{16}O) in minerals such as ice and quartz can produce carbon-14 (^{14}C). In glacial ice, ^{14}C is also incorporated through trapping of ^{14}C-containing atmospheric gases (^{14}CO$_2$, ^{14}CO, and ^{14}CH$_4$). Understanding the production rates of in situ cosmogenic ^{14}C is important to deconvolve the in situ cosmogenic and atmospheric ^{14}C signals in ice, both of which contain valuable paleoenvironmental information. Unfortunately, the in situ ^{14}C production rates by muons (which are the dominant production mechanism at depths of > 6 m solid ice equivalent) are uncertain. In this study, we

use measurements of in situ ^{14}C in ancient ice (> 50 ka) from the Taylor Glacier, an ablation site in Antarctica, in combination with a 2D ice flow model to better constrain the compound-specific rates of ^{14}C production by muons and the partitioning of in situ ^{14}C between CO$_2$, CO, and CH$_4$. Our measurements show that 33.7 % ($\pm$11.4 %; 95 % confidence interval) of the produced cosmogenic ^{14}C forms ^{14}CO and 66.1 % ($\pm$11.5 %; 95 % confidence interval) of the produced cosmogenic ^{14}C forms ^{14}CO$_2$. ^{14}CH$_4$ represents a very small fraction (< 0.3 %) of the total. Assuming that the majority of in situ muogenic ^{14}C in ice forms ^{14}CO$_2$, ^{14}CO, and ^{14}CH$_4$, we also calculated muogenic ^{14}C production rates that are lower by factors of 5.7 (3.6–13.9; 95 % confidence inter-

val) and 3.7 (2.0–11.9; 95 % confidence interval) for nega-
tive muon capture and fast muon interactions, respectively,
when compared to values determined in quartz from labo-
ratory studies (Heisinger et al., 2002a, b) and in a natural
setting (Lupker et al., 2015). This apparent discrepancy in
muogenic ^{14}C production rates in ice and quartz currently
lacks a good explanation and requires further investigation.

1 Introduction

1.1 Potential applications of ^{14}C measurements in ice
and in situ cosmogenic ^{14}C production from ^{16}O in
Earth's surface minerals

As snow accumulates on ice sheets, it gradually densifies
into firn and ice (Herron and Langway, 1980). During the
firn-to-ice transition, the air in the interstitial space between
the ice grains becomes trapped into bubbles within the ice
matrix (Buizert, 2013). Included in the paleoatmospheric air
trapped in the bubbles are ^{14}C-containing atmospheric gases
($^{14}CO_2$, ^{14}CO, and $^{14}CH_4$; Fireman and Norris, 1982). ^{14}C
in ice is also produced through interactions of secondary cos-
mic rays with ^{16}O directly in the lattice of the ice grains (i.e.,
in situ; Lal et al., 1990). Following the cosmogenic nuclear
reactions, the hot ^{14}C atom interacts with atoms in the sur-
rounding ice lattice to produce $^{14}CO_2$, ^{14}CO, and $^{14}CH_4$ (Lal
et al., 1990; Petrenko et al., 2013).

Both the trapped atmospheric and in situ cosmogenic ^{14}C
signals in ice have unique applications. For example, the pa-
leoatmospheric component of $^{14}CH_4$ in ice cores has been
used to constrain past CH_4 emissions from old carbon reser-
voirs such as methane hydrates, permafrost, and geologic
seeps (Dyonisius et al., 2020; Hmiel et al., 2020; Petrenko
et al., 2009, 2017). Paleoatmospheric $^{14}CO_2$ can be poten-
tially used for the absolute dating of ice core gases (Andree
et al., 1984; Van De Wal et al., 1994) and to improve the
radiocarbon calibration curve (Reimer et al., 2020; Hogg et
al., 2020) in periods where tree ring data are not available.
Measurements of ^{14}CO in the modern atmosphere have been
used to constrain the oxidative capacity of the atmosphere
(Brenninkmeijer et al., 1992; Petrenko et al., 2021), and thus,
paleoatmospheric ^{14}CO in ice cores can be used for a simi-
lar application. The in situ cosmogenic component of ^{14}CO
at ice core sites can be potentially be used to reconstruct the
past cosmic ray flux (BenZvi et al., 2019). Finally, measure-
ments of the in situ cosmogenic component of $^{14}CO_2$ and
^{14}CO can be used to constrain the accumulation/ablation rate
of the ice core site (e.g., Lal et al., 1990; Lal and Jull, 1990).
Unfortunately, the paleoatmospheric and in situ cosmogenic
components of ^{14}C in ice exist in a combined form and can-
not be separated analytically (Petrenko et al., 2016). To sep-
arate these signals, it is important to have accurate estimates
of the cosmogenic ^{14}C production rates and the partitioning

among the in situ produced ^{14}C species ($^{14}CO_2$, ^{14}CO, and
$^{14}CH_4$) in ice.

In situ cosmogenic ^{14}C production in ice is analogous
to the production in quartz because both minerals share
the same target atom (^{16}O). Measurements of in situ cos-
mogenic nuclides (^{3}He, ^{10}Be, ^{14}C, ^{21}Ne, ^{26}Al, and ^{36}Cl)
in near-surface rocks are commonly used as tools to con-
strain various Earth surface processes such as the timing of
glacial retreat and erosion rates (Gosse and Phillips, 2001;
Balco, 2020). Due to its short half-life of 5700 ±30 years
(Kutschera, 2019), ^{14}C in quartz is uniquely suited to charac-
terize surface processes on millennial timescales (e.g., Spec-
tor et al., 2019; Pendleton et al., 2019). In situ cosmogenic
^{14}C measurements are also often paired with measurements
of longer-lived nuclides such as ^{10}Be and ^{26}Al (e.g., Hippe,
2017; Skov et al., 2019) to study complex surface processes
such as subglacial erosion and millennial-scale glacier re-
treats and/or re-advances.

In situ cosmogenic ^{14}C in Earth's surface minerals is pro-
duced from ^{16}O by three nuclear reactions, namely (1) nu-
cleon (neutron and proton)-induced spallation (Lal and Pe-
ters, 1967), (2) negative muon capture (Heisinger et al.,
2002b), and (3) interactions with fast muons (Heisinger et al.,
2002a). The depth dependence of the ^{14}C production rate for
each mechanism in ice is shown in Fig. 1. Nucleon-induced
spallation dominates the ^{14}C production at the surface but is
quickly attenuated with depth. On the other hand, the relative
contributions from the two muon mechanisms are lower near
the surface but dominate at larger depths, as muons can pene-
trate deeper than nucleons (Fig. 1). Characterizing the in situ
cosmogenic ^{14}C production rates from muons is especially
important for applications of cosmogenic surface exposure
dating where the samples might be exposed to the subsurface
cosmic ray flux for an extended period. One example of this
would be a bedrock that is covered by a relatively thin (e.g.,
tens of meters) glacier.

Understanding the muogenic ^{14}C component is especially
important for ^{14}C studies in ice. Prior studies have shown
that, at snow accumulation sites, most of the in situ ^{14}C pro-
duced in the firn (including the majority of neutron-produced
^{14}C) is lost to the atmosphere via gas movement in the firn
open porosity (Petrenko et al., 2013; Van der Kemp et al.,
2000; Wilson and Donahue, 1990). In situ cosmogenic ^{14}C
mainly starts to accumulate in deeper ice where gas exchange
with the atmosphere no longer happens, and at these depths,
the ^{14}C production is entirely from the muon mechanisms.
Thus, the in situ cosmogenic ^{14}C signal in traditional deep
ice cores is dominated by production from muons, and con-
straining the muogenic ^{14}C production rates is critical to dis-
entangle the in situ cosmogenic and atmospheric ^{14}C signals
in ice cores. Unfortunately, the in situ ^{14}C production rates
by muons in both ice and quartz are still highly uncertain
(Hippe, 2017).

The production rates of cosmogenic nuclides are usually
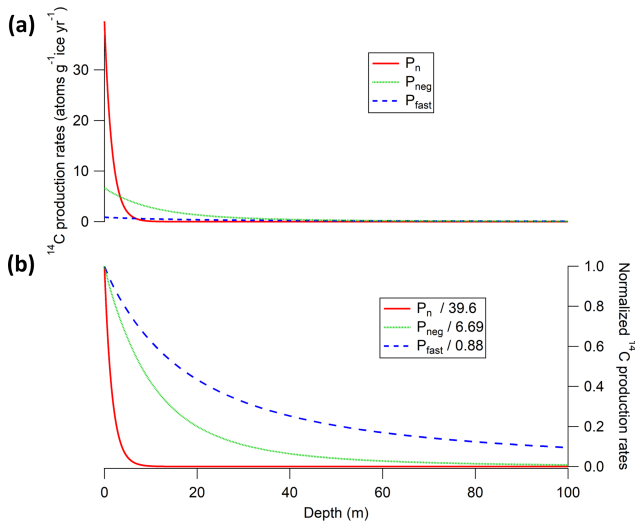determined from calibration sites where independent con-

Figure 1. (a) In situ cosmogenic ^{14}C production rates scaled for the Taylor Glacier study site (77°44′ S, 162°10′ E; 526 m elevation) from the three nuclear mechanisms, i.e., nucleon-induced spallation (P_n), negative muon capture (P_{neg}), and fast muon interactions (P_{fast}). **(b)** Depth profiles of the three production mechanisms normalized to their respective surface production rates (the respective surface production rates are shown in the legend). For ^{14}C production from neutron spallation, we used the surface production rate estimate from Young et al. (2014) with scaling from the Lifton et al. (2014) LSDn model. For the two muon mechanisms (negative and fast muons), we used the production rate model from Balco et al. (2008), which follows parameterizations by Heisinger et al. (2002a, b).

trols on exposure history are available, such as ^{14}C dating from organic materials (e.g., Lifton et al., 2015) or argon (^{40}Ar/^{39}Ar) dating from lava flows (e.g., Balbas and Farley, 2020; Fenton et al., 2019). However, the commonly used estimates of muogenic ^{14}C production rates (for both negative muon capture and fast muon reactions) were derived through the laboratory irradiation of artificial target compounds (Heisinger et al., 2002a, b). To our knowledge, there is only one prior study (Lupker et al., 2015) that provided estimates of total muogenic in situ ^{14}C production rates based on measurements in a natural setting. Using ^{14}C measurements from a 15.5 m deep quartzite core from Leymon High, Spain, Lupker et al. (2015) estimated a sea level high latitude (SLHL) surface production rate of 3.34 (+0.43/ − 1.07) ^{14}C atoms per gram of quartz per year for negative muon capture and 0 (+0.42/ − 0.00) ^{14}C atoms per gram of quartz per year for fast muon interactions (1σ uncertainties). The large uncertainties in the ^{14}C production rates (especially the production rate from fast muons) estimated by Lupker et al. (2015) were due to relatively large measurement uncertainty for their deepest samples and a small contribution to the ^{14}C signal from fast muons. Balco (2017) also refitted the Leymon High data and obtained similar results regarding

the magnitude of the SLHL ^{14}C production rate from negative muon capture.

Petrenko et al. (2016) used ^{14}C measurements (^{14}CO, ^{14}CO$_2$, and ^{14}CH$_4$) in > 50 ka ice for the 2–20 m depth range from Taylor Glacier, Antarctica, to constrain the ^{14}C production rates in ice. The old age of the ice ensured that all in situ cosmogenic and paleoatmospheric ^{14}C inherited from the ice accumulation site had decayed away. Unfortunately, Petrenko et al. (2016) were unable to accurately constrain the total ^{14}C production rates because of the high uncertainty resulting from the melt–extraction technique used to obtain their ^{14}CO$_2$ measurements (see Sect. 1.3).

1.2 Overview of ^{14}C production from muons

Following Heisinger et al. (2002b), the production rate of ^{14}C (atoms per gram per year) by negative muon capture (P_{neg}) as a function of lithospheric depth (h; typically in g cm^{-2}) is given by the following:

$$P_{neg}(h) = R_{\mu -}(h) \cdot f_{tot} \qquad (1)$$
$$f_{tot} = f_C \cdot f_D \cdot f^*, \qquad (2)$$

where $R_{\mu -}(z)$ is the stopping rate of negative muons (muons per gram per year) at lithospheric depth h, and f_{tot} is the overall probability of ^{14}C production in ice from a stopped negative muon (unitless). The stopping rate of negative muons at the given depth $R_{\mu -}(h)$ has been empirically determined from measurements at deep underground laboratories (Heisinger et al., 2002b). The lithospheric depth (h) is a product of actual depth (z) and density (ρ) of the target mineral ($\rho_{ice} = 0.92$ g cm^{-3}).

The total probability (f_{tot}) of ^{14}C production from negative muon capture is expressed by the product of the chemical compound factor (f_C), representing the probability that the stopped muon is captured by one of the target atoms (^{16}O in case of ^{14}C production), the probability that the negative muon does not decay in the K shell before nuclear capture (f_D), and the effective probability for the production of cosmogenic nuclides after μ- capture by the target atom (f^*; Eq. 2; Heisinger et al., 2002b; Lupker et al., 2015). All probability (f) terms in Eq. (2) are unitless. From experiments involving laboratory irradiation of artificial targets, the overall probability (f_{tot}) for ^{14}C production in ice from negative muon was estimated to be 0.025 ± 0.002 (Heisinger et al., 2002b).

An expression for the production rate of nuclides by fast muon interactions (P_{fast}) as a function of lithospheric depth (h) is given by Heisinger et al. (2002a):

$$P_{fast}(h) = \sigma_0 \cdot \beta(h)\phi(h) \cdot \overline{E}(h)\alpha \cdot N \qquad (3)$$
$$\beta(h) = 0.846 - 0.015\ln(h+1) + 0.003139(\ln(h+1))^2, \qquad (4)$$

where $\phi(h)$ is the total muon flux at depth z (muons per centimeter squared per year per steradian), σ_0 is the reference nuclear reaction cross section at muon energy of 1 GeV

(millibarn, mb), $\beta(h)$ is the unitless parameterized depth-dependence factor (Eq. 4), $\overline{E}(h)$ is the mean muon energy at depth h (GeV), α is a power factor that describes the energy dependence of the cross section (unitless; $\alpha = 0.75$), and N is the number of target nuclei per gram of the target mineral. The overall production rate of ^{14}C from fast muons provided by Heisinger et al. (2002a) has a high ($\pm 50\%$) uncertainty because of the uncertainty in the reference nuclear reaction cross section σ_0 ($\sigma_0 = 0.0088 \pm 0.0049$ mb). Following Lupker et al. (2015), in this study we used f_{tot} and σ_0 as tuning parameters for the two muogenic production mechanisms in a cosmogenic nuclide production model (Sect. 3.2) to fit our ^{14}C measurements.

1.3 Gas extraction methods for ice core ^{14}C analysis

Common methods to liberate gas trapped in ice core bubbles include melting (wet extraction; e.g., Sowers et al., 1992; Mitchell et al., 2011) and mechanical destruction of the ice lattice (dry extraction; e.g., Bereiter et al., 2013; Ahn et al., 2009; Zumbrunn et al., 1982). Dry extraction is generally preferable for CO_2 analysis because the presence of liquid water in a wet extraction introduces extraneous CO_2 from the carbonate–acid reaction between the meltwater and impurities in the ice (e.g., Delmas et al., 1980; Raynaud et al., 1982). Multiple studies of $^{14}CO_2$ in ice have used dry extraction methods (e.g., Van De Wal et al., 1994, 2007; Smith et al., 2000; Van der Kemp et al., 2000). However, dry extraction systems (e.g., Lüthi et al., 2008) can potentially introduce biases in the CO_2 mole fraction [CO_2] due to incomplete gas extraction (Bereiter et al., 2015). Considering that the in situ cosmogenic production of ^{14}C occurs directly in the ice lattice (Lal et al., 1990), it has been argued that dry extraction may also not liberate all of the ^{14}C from the ice (e.g., van Roijen et al., 1994).

Other studies of ^{14}C in ice (e.g., Lal et al., 1990, 1997, 2001; Jull et al., 1994) have used wet extraction methods. These wet extraction studies involved an addition of acid to drive off all dissolved CO_2 from the meltwater (Lal et al., 1990, 1997, 2001; Jull et al., 1994). The acidification process may have resulted in an additional CO_2 release from impurities in the ice (e.g., carbonate dust). In dust-rich Greenland ice, the presence of liquid water in a wet extraction produced excess CH_4 artifacts (Lee et al., 2020). It is thus possible that a wet extraction approach for ^{14}C analysis may also result in additional C release from organics in the ice which are not ^{14}C free.

A third method to liberate gases trapped in ice cores is sublimation under vacuum (e.g., Wilson and Donahue, 1989, 1990; Wilson and Long, 1997; Siegenthaler et al., 2005; Schmitt et al., 2011). Sublimation can occur when the pressure and temperature on the surface of the ice are below the triple point of the water-phase-change diagram. In addition to being free of problems associated with wet extraction methods, sublimation guarantees 100 % gas extraction efficiency

(Schmitt et al., 2011; Bereiter et al., 2013, 2015), which includes any ^{14}C trapped in the ice lattice. Therefore, sublimation is likely an optimal method for $^{14}CO_2$ measurements in ice.

This study presents new ^{14}C measurements in three gas species (^{14}CO, $^{14}CO_2$, and $^{14}CH_4$) in ancient (> 50 ka) ice from the ablation zone of the Taylor Glacier, Antarctica, to constrain the compound-specific ^{14}C production rates in ice by muons. Ice at this location does not contain a significant amount of ^{14}C inherited from the accumulation site (Petrenko et al., 2016), and the ^{14}C content is entirely due to production by muons during transport within the glacier. We improved on the earlier work by Petrenko et al. (2016) by (1) using a newly developed ice sublimation extraction device for $^{14}CO_2$ measurements (see Sect. 2.3.2), (2) collecting deeper samples to ~ 72 m to better characterize the ^{14}C production rate from the fast muon mechanism, and (3) using a more realistic 2D ice flow model from Buizert et al. (2012) to account for the flow trajectory and exposure history of the samples (see Sect. 3.1).

2 Field sampling and analytical methods

2.1 Site description

The blue ice area of the Taylor Glacier (Fig. 2) provides access to near-unlimited amounts of well-dated ancient ice (Baggenstos et al., 2017; Bauska et al., 2016; Menking et al., 2019; Schilt et al., 2014; Shackleton et al., 2020). This allows ice from Taylor Glacier to be measured for ultra-trace-gas species that require a very large amount of ice (Dyonisius et al., 2020; Petrenko et al., 2016, 2017; Buizert et al., 2014). In this study, we used the same site as Petrenko et al. (2016; 77°43.699′ S, 161°43.179′), where ice > 50 ka in age at the surface has been previously identified.

2.2 Field sampling

Approximately 1000 kg of ice is needed to obtain both the necessary CH_4-derived and CO-derived C mass for ^{14}C analyses. Because of this large sample requirement, and to avoid post-coring in situ ^{14}C production at the surface, the melt extraction for $^{14}CH_4$ and ^{14}CO samples was performed on site using the large-volume melter apparatus and technique described in Petrenko et al. (2016). The liberated air was transferred to 34.9 L electropolished stainless steel canisters and shipped to our laboratories for processing and analyses. Similar to other studies using this large-volume ice melter (e.g., Dyonisius et al., 2020; Petrenko et al., 2016, 2017), four procedural blanks (two with modern $^{14}CH_4$ standard gas and two with ^{14}C dead $^{14}CH_4$ standard gas) were collected in the field. These field procedural blanks allow us to characterize the addition of extraneous ^{14}C to the samples. The standard gases used in the field procedural blanks were passed through
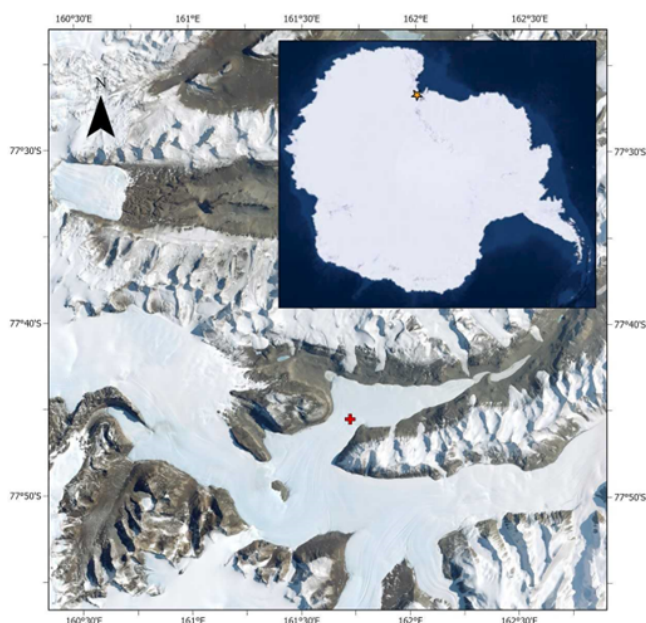
Figure 2. Map of the Taylor Glacier study site. The sampling location is marked by a red cross on the map. The orange star in the inset map shows the location of the Taylor Glacier relative to the Antarctic continent. The map was made using ArcGIS Pro, with imagery layers from Esri and Earthstar Geographics.

a Sofnocat 423 reagent, which removes CO (and thus ^{14}CO) but leaves CH_4 (and $^{14}CH_4$) intact.

The sampling scheme for this study is shown in Fig. S1 in the Supplement. We used the 9.5 in. (241 mm) diameter Blue Ice Drill (BID; Kuhl et al., 2014) to collect seven large-volume samples during the 2015/2016 austral summer field season for ^{14}CO and $^{14}CH_4$ analyses. The surface sample was collected from 21×1.5 m deep shallow cores, each with an average mid-depth of ~ 0.75 m. Six additional deep samples with mid-depths of 19.5, 30, 40.5, 51, 61.5, and 72 m were also collected by combining ice from three ~ 78 m deep boreholes. Each of the deep large-volume samples spanned approximately 10.5 m depth. Continuous sticks of ice subsamples (3×3 cm; spanning the whole length of the core) were taken from one of the three ice core boreholes (TGDeep3) for age control (see Sect. S3 in the Supplement). The continuous sample sticks were measured for the CH_4 mole fraction $[CH_4]$ using the continuous flow analysis (CFA) system described in Rhodes et al. (2013) at Oregon State University (OSU).

In addition to the large-volume samples, we collected 26 smaller subsamples (~ 1.5–2 kg) from 13 depth levels and two boreholes for $^{14}CO_2$ measurements. Each depth level contained a pair of replicates; however, only 9 out of the 13 replicate pairs were true replicates (i.e., collected from the same borehole and cut from the same depth interval; Fig. S1). Collecting same depth-adjacent samples below 50 m depth from a single borehole was challenging because of the re-

duced core quality (i.e., more fractures in the ice), and thus, the replicates had to be collected from a different borehole. Immediately after removal from the borehole, ice samples become exposed to a more intense cosmic ray bombardment (post-coring in situ cosmogenic ^{14}C production). Five artificial bubble-free ice (BFI) samples were manufactured in the field, following methods from Mitchell et al. (2011), but upscaled to produce 1.5–2 kg samples. The field-produced BFI samples were shipped together with the collected glacial ice samples to characterize the effects of the post-coring in situ cosmogenic $^{14}CO_2$ production in the samples.

2.3 Laboratory analytical methods

2.3.1 Large-volume samples for ^{14}CO and $^{14}CH_4$ measurements

The detailed approach for sample processing, measurements, and associated procedural corrections for the large-volume samples have been previously described in detail (Petrenko et al., 2016). In this section, we only provide a brief overview and highlight the differences between our methods and those of Dyonisius et al. (2020). First, the $\delta^{13}CH_4$ measurements were conducted at the Institute of Arctic and Alpine Research (INSTAAR), following the methods described by Miller et al. (2002; Table S1 in the Supplement). The $\delta^{13}CH_4$ measurements were not corrected for gravitational (Sowers et al., 1992) and diffusive isotopic fractionation (Buizert et al., 2013) because these corrections are only necessary to reconstruct the paleoatmospheric $\delta^{13}CH_4$ signal. In this study, the $\delta^{13}CH_4$ values are only used to normalize and calculate the absolute $^{14}CH_4$ abundance (in molec. per gram of ice).

The large-volume samples and field procedural blanks were measured for $[CH_4]$ using a gas chromatograph–multidetector (GC-MD) system (Prinn et al., 2008; Table S2). Pressure in the sample canisters was measured using a Paroscientific, Inc., Digiquartz® series 740 absolute pressure transducer at the Scripps Institution of Oceanography (SIO) for total air content (TAC) determination (Table S3). Two of the field procedural blanks were also measured for the Kr/N_2, Xe/N_2, and Xe/Kr ratio (Table S4) at the Scripps Institution of Oceanography (SIO), following the procedures described in Bereiter et al. (2018). The noble gas ratios were used to constrain the degree of gas solubility during the melt extraction. The large-volume samples were measured for CO mole fraction $[CO]$ using a Picarro G2401 analyzer (Table S5) and again for pressure at the University of Rochester (UR; Table S4).

The CH_4 in the large-volume samples and blanks was combusted to CO_2, cryogenically separated, and flame-sealed in glass ampules using the air processing line at the University of Rochester (Dyonisius et al., 2020). We also processed 3×100 μg of CH_4-derived C samples each from the modern $^{14}CH_4$ standard gas and ^{14}C dead standard gas used for the field procedural blanks. The sample air

that remained after CH_4 processing (~ 10 L standard temperature pressure, STP) was diluted with a gas containing 10.02 ± 0.26 µmol mol^{-1} (95 % confidence interval, CI) of ^{14}C-depleted CO (^{14}CO = 0.19 ± 0.08 pMC; 95 % CI) to increase the CO-derived C mass for the accelerator mass spectrometry (AMS) measurements. The dilutant gas was measured for δ^{13}CO using methods described in Vimont (2017; δ^{13}CO = -23.36 ± 0.2‰; 95 %CI).

The CO- and CH_4-derived CO_2 was graphitized using the Australian Nuclear Science and Technology Organization (ANSTO) micro-furnaces, following Yang and Smith (2017). We used the ^{14}C activity measured on the 100 µg samples as the true ^{14}C activity of the standard gases (Table S6). Because of the larger sample size, the effect of extraneous C introduced by graphitization on these 100 µg samples is assumed to be negligible. Using a mass balance approach described in Petrenko et al. (2017), the total extraneous C mass for the $^{14}CH_4$ samples was determined to be 0.63 ± 0.28 µgC, and the corresponding ^{14}C activity for the extraneous C was 16.7 ± 10.2 pMC (95 % CI).

In prior studies (e.g., Dyonisius et al., 2020; Petrenko et al., 2017), ^{14}CO measurements from the field procedural blanks were used to characterize the effects of extraneous ^{14}C addition from sample extraction, handling, storage, transport, and processing (including the graphitization step). For this study, the field procedural blanks were still used to characterize the effects from in situ production of ^{14}CO in the sample air canisters by cosmic rays during storage and transport. However, to better characterize the effects from the addition of extraneous C during the graphitization process, we used a linear empirical correction from 10 commensurately sized ^{14}C standards and blanks at ANSTO (see Fig. S2a; Table S7), following Petrenko et al. (2021). This approach has the benefit of bracketing the effects of extraneous C from graphitization at ANSTO with low and high ^{14}C standards, similar to the approach for the $^{14}CH_4$ samples. The ^{14}CO blank for this sample set is 22.45 ± 3.24 molec. ^{14}CO per cc of air STP (95 % CI), which is higher than the ^{14}CO blanks reported in Dyonisius et al. (2020). This is mainly because there was an extra year between the retrieval and processing of the samples (thus, there was more in situ ^{14}CO production in sample canisters during storage). The amount of ^{14}C per gram of ice for ^{14}CO, $^{14}CH_4$, and $^{14}CO_2$ (Table 1) is calculated using the same method as in Petrenko et al. (2016) and is consistent with the Hippe and Lifton (2014) formulations for in situ ^{14}C concentrations. $^{14}CH_4$ and ^{14}CO measurements in our samples after all associated corrections, in addition to earlier Taylor Glacier results from Petrenko et al. (2016), are shown in Table 1 and Fig. 3.

2.3.2 Sublimation and processing of samples for $^{14}CO_2$ measurements

CO_2 was liberated from ice samples using a newly developed ice sublimation device at the University of Rochester (Hmiel, 2020), roughly following the design of Schmitt et al. (2011). To briefly summarize the procedure, 1.5–2 kg ice samples were loaded into a vacuum glass vessel. The vessel was then evacuated, and the ice was sublimated at vacuum with six infrared emitters (Emitted Energy, USA) for 8–10 h. We did not sublimate 100 % of the samples because, as the ice sublimates away, impurities such as dust and organics start to accumulate on the surface. The aggregation of impurities on the sublimation front might enhance unwanted chemical reactions that produce extraneous carbon (Schmitt et al., 2011). Furthermore, towards the end of the extraction, the sublimation became less efficient as less surface area was available to absorb radiation. Approximately 1 kg of ice was sublimated in 8–10 h. However, the incomplete sublimation does not compromise the 100 % extraction efficiency, as all the gases trapped in the ice that is sublimated away are still released (Schmitt et al., 2011).

The liberated CO_2 was cryogenically trapped with liquid nitrogen, and the air was also cryogenically trapped with 5Å molecular sieve (Sigma-Aldrich, USA) under liquid nitrogen. After the sublimation was completed, the trapped CO_2 and air were expanded into separate volume-calibrated manometers in which pressure measurements were taken to calculate the [CO_2]. Finally, the isolated CO_2 was cryogenically transferred to and flame-sealed into a Pyrex glass ampule. The CO_2 was graphitized at ANSTO using the micro-furnaces (Yang and Smith, 2017), and the graphitized samples were measured for ^{14}C activity at the ANTARES AMS facility (Smith et al., 2010). One $^{14}CO_2$ sample (replicate for 30 m depth sample) was unfortunately lost during sublimation because the ice fractured under vacuum during the evacuation step.

A ~ 50–75 g ice subsample was taken from every $^{14}CO_2$ sample and shipped to OSU. The aliquots were measured for [CO_2], following Ahn et al. (2009), and [CH_4] and TAC, following Mitchell et al. (2013; Table S8). Five field-produced bubble-free ice (BFI) samples and nine laboratory-produced BFI samples were also sublimated along with the glacial ice samples. During the sublimation of the BFI samples, a standard gas with known $^{14}CO_2$ activity and [CO_2] was introduced into the bottom of the glass sublimation vessel at 0.15 scc min^{-1} flow rate for 8–10 h. The flow rate was set to mimic the rate of air liberation from glacial ice samples and the processing time also mimicked the amount of time needed to sublimate glacial ice samples. We used a standard gas with dead $^{14}CO_2$ activity for four laboratory-produced BFI samples and a standard gas with modern $^{14}CO_2$ activity for the other five laboratory-produced BFI samples. The CO_2 was cryogenically trapped downstream, processed, and measured for ^{14}C activity, following the same methods as the ice samples. In combination with the OSU [CO_2] and TAC measurements, the BFI samples were used to constrain the amount of extraneous carbon and ^{14}C introduced by sample transport, storage, and processing (see Sect. S1; Table S9). Finally, 11 commensurately sized ^{14}C standards

Table 1. Measured $^{14}CO_2$, ^{14}CO, and $^{14}CH_4$ after all associated corrections and calculated total ^{14}C, $^{14}CH_4/^{14}CO$ ratios, $^{14}CO_2$, and ^{14}CO fractions. All errors presented indicate the 95 % CI. NA – not available.

Mid-depth (m)	$^{14}CO_2$ (molec. per gram of ice)	^{14}CO (molec. per gram of ice)	$^{14}CH_4$ (molec. per gram of ice)	Total ^{14}C (atoms per gram of ice)	$^{14}CH_4/^{14}CO$ ratio	$^{14}CO_2$ fraction	^{14}CO fraction
2.25	145.5 ± 32.0	45.2 ± 3.2[a]	0.418 ± 0.052[a]	191.1 ± 32.2	0.0092 ± 0.0013	0.76 ± 0.18	0.24 ± 0.04
	123.3 ± 28.5			168.9 ± 28.7		0.73 ± 0.18	0.27 ± 0.05
3.65	88.5 ± 7.8	41.9 ± 2.2[a]	0.327 ± 0.026[a]	130.7 ± 8.1	0.0078 ± 0.0007	0.68 ± 0.07	0.32 ± 0.03
	98.0 ± 7.8			140.2 ± 8.1		0.70 ± 0.07	0.30 ± 0.02
6.85	64.2 ± 7.8	36.4 ± 1.8[a]	0.273 ± 0.020[a]	100.9 ± 8.0	0.0075 ± 0.0007	0.64 ± 0.08	0.36 ± 0.03
	69.4 ± 7.8			106.1 ± 8.0		0.65 ± 0.08	0.34 ± 0.03
10[b]	50.6 ± 7.8	31.4 ± 1.6[a]	NA	82.2 ± 8.0[b]	NA	0.62 ± 0.10	0.38 ± 0.04
	54.3 ± 7.8			86 ± 7.9[b]		0.63 ± 0.10	0.37 ± 0.04
15	60.9 ± 7.8	26.9 ± 1.4[a]	0.206 ± 0.016[a]	88.0 ± 7.9	0.0077 ± 0.0007	0.69 ± 0.10	0.31 ± 0.03
	54.6 ± 7.8			81.7 ± 7.9		0.67 ± 0.10	0.33 ± 0.04
19.5	52.4 ± 7.8	23.9 ± 1.2[a]	0.182 ± 0.016[a]	76.5 ± 7.9	0.0076 ± 0.0008	0.69 ± 0.11	0.31 ± 0.04
	49.6 ± 7.8			73.7 ± 7.9		0.67 ± 0.11	0.32 ± 0.04
40.5	36.4 ± 7.8	15.8 ± 1.0	0.119 ± 0.013	52.3 ± 7.8	0.0075 ± 0.0010	0.70 ± 0.15	0.30 ± 0.05
	37.2 ± 7.8			53.1 ± 7.9		0.70 ± 0.15	0.30 ± 0.05
51	31.1 ± 7.8	13.2 ± 0.9	0.097 ± 0.014	44.4 ± 7.8	0.0073 ± 0.0012	0.70 ± 0.18	0.30 ± 0.06
	28.0 ± 7.8			41.3 ± 7.8		0.68 ± 0.19	0.32 ± 0.06
61.5	22.1 ± 7.8	11.3 ± 0.7	0.079 ± 0.013	33.5 ± 7.8	0.0070 ± 0.0012	0.66 ± 0.24	0.34 ± 0.08
	31.0 ± 7.8			42.4 ± 7.8		0.73 ± 0.19	0.27 ± 0.05
72	11.8 ± 7.8	10.8 ± 0.7	0.080 ± 0.013	22.7 ± 7.8	0.0074 ± 0.0013	0.52 ± 0.34	0.48 ± 0.17
	13.6 ± 7.8			24.5 ± 7.8		0.55 ± 0.32	0.44 ± 0.14

[a] Data from Petrenko et al. (2016). [b] The total ^{14}C value for the 10 m sample was scaled by a factor of 1.003 ± 0.003 (95 % CI) to account for the lack of $^{14}CH_4$ measurements (Sect. 4.2).

and blanks (14–16 µgC) with known ^{14}C activities (in 0–135 pMC range) were prepared, graphitized, and measured at ANSTO, concurrently with all the samples (Table S7), to characterize the effects from the addition of extraneous C during the graphitization process.

The detailed corrections for the $^{14}CO_2$ samples are discussed in the Supplement. We correct for the effects of extraneous C from graphitization and other ANSTO processing using a linear empirical correction from the commensurately sized ^{14}C standards (Sect. S1.1; Fig. S2b). The effects of extraneous carbon from ice sublimation/CO_2 extraction are calculated from the difference in measured ^{14}C activity of the laboratory-produced BFI samples relative to the measured ^{14}C activity of the standard gases with a mass balance approach (Sect. S1.2; Tables S8 and S9). Finally, the samples were corrected for the effects of post-coring in situ $^{14}CO_2$ production in ice using results from the field-produced BFI samples (Sect. S1.3; Table S10). The $^{14}CO_2$ measurements in our samples after all associated corrections with their error-propagated uncertainties are shown in Table 1 and Fig. 3.

An in-depth discussion about the analytical uncertainty in the $^{14}CO_2$ measurements obtained from the sublimation method (which is important for the interpretation of the data because it is the largest source of uncertainty for total ^{14}C) is provided in Sect. S1.4. In brief, we used the pooled standard deviation of replicate pairs (± 7.8 $^{14}CO_2$ molec. per gram of ice; 2σ) as the uncertainty for all $^{14}CO_2$ measurements, except the 2.25 m sample pair (where we used the error-propagated uncertainties instead; Table 1). For the rest of the paper, we refer to the sum of measured ^{14}CO, $^{14}CO_2$, and $^{14}CH_4$ as the total ^{14}C. The $^{14}CH_4/^{14}CO$, ^{14}CO/total and $^{14}CO_2$/total ^{14}C ratio of the samples are shown in Fig. 4.

2.4 Sample integrity

Several samples were excluded from the data analysis; the detailed reasoning for rejecting these samples is discussed in Sects. S2 and S3. The surface samples (0.75 m depth) for all three ^{14}C species (^{14}CO, $^{14}CH_4$, and $^{14}CO_2$) are rejected because of ambient air contamination from abundant fractures in the ice sample (due to thermal stresses in near-surface ice)

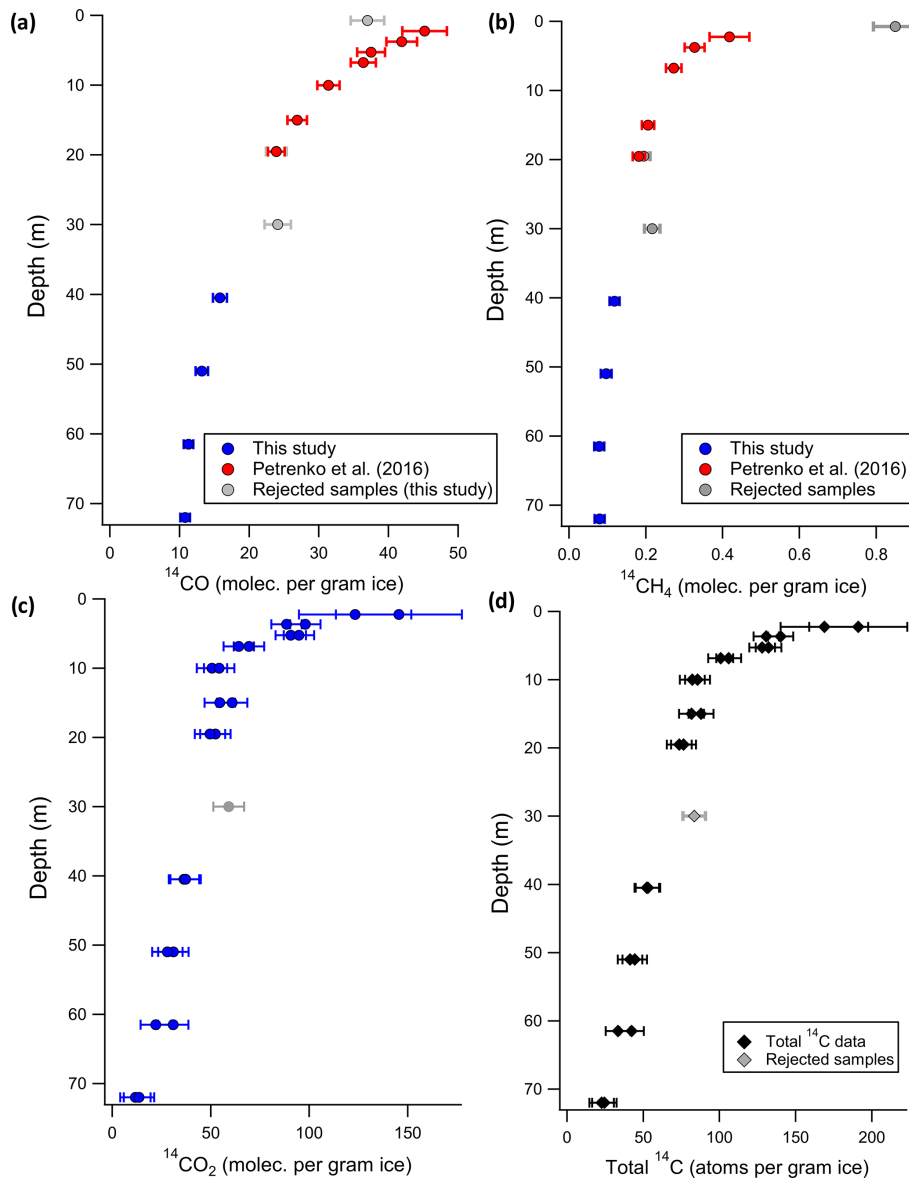**Figure 3. (a)** Measured ^{14}CO molec. per gram of ice after all corrections. **(b)** Measured $^{14}CH_4$ molec. per gram of ice after all corrections. **(c)** Measured $^{14}CO_2$ molec. per gram of ice after all corrections. **(d)** Total measured ^{14}C atoms per gram of ice. This represents the sum of ^{14}CO, $^{14}CH_4$, and sublimation-based $^{14}CO_2$ measurements. All error bars shown in this figure are 95 % CI.

and the likely chemical and/or biological alteration of CH_4, CO, and CO_2. The 19.5 and 30 m ^{14}CO and $^{14}CH_4$ samples from the 2015/2016 season were rejected because of anomalous alterations in TAC, [CO], and [CH_4]. The 30 m $^{14}CO_2$ sample was also rejected due to alteration in [CO_2].

3   Estimating the muogenic ^{14}C production rates

3.1   Ice flow model to constrain sample exposure history

We used a 2D ice flow model from Buizert et al. (2012) to generate flow trajectories for the ice parcels corresponding to each sample depth (Fig. 5). The model first computes the 2D steady-state ice flow velocity field based on the observed surface velocities, ablation rates, and glacier thickness and then generates an ice parcel back-trajectory using a 2D linear interpolation of the ice flow velocity field (Kavanaugh et al., 2009a, b; Kavanaugh and Cuffey, 2009; Bliss et al., 2011). The largest source of uncertainty for the trajectories are the ablation rates (Buizert et al., 2012), which are based on measurements of 163 poles initially planted in 2002/2003 (Kavanaugh et al., 2009b; Bliss et al., 2011). All survey poles were measured a year later, providing 1-year average ablation rate estimates (Kavanaugh et al., 2009b) and again in
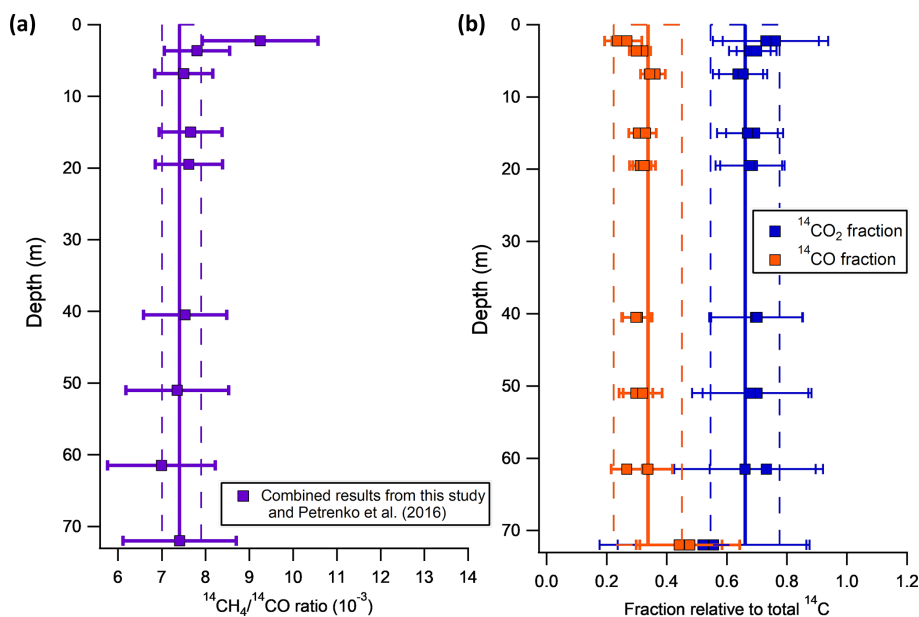
Figure 4. (a) $^{14}CH_4/^{14}CO$. **(b)** $^{14}CO/$total ^{14}C and $^{14}CO_2/$total ^{14}C ratio. The solid lines represent the mean, and the dashed lines represent 2 standard deviations of the $^{14}CH_4/^{14}CO$ ratio, $^{14}CO_2$, and ^{14}CO fractions for samples deeper than 6.85 m where production by muons dominates. The ratios for rejected samples (Sects. 4.1, S2) are not shown. All error bars shown in this figure are 95 % CI.

the 2006/2007 season. Additionally, 17 poles were remeasured in the 2009/2010 and 2010/2011 seasons (Buizert et al., 2012). The 4-year average ablation rates were 4.7 cm yr^{-1} higher than the 1-year average (Kavanaugh et al., 2009b); following Buizert et al. (2012), the ablation rate uncertainty for each pole was calculated by dividing 4.7 cm yr^{-1} with $\sqrt{N}$, where N is the length of the observation period in years ($N = 1, 4, 7,$ or 8). Figure S3 shows the ablation rates along the glacier and their uncertainties inferred from the survey pole data.

The ice flow model used a bedrock profile from Kavanaugh et al. (2009a); however, the bedrock profile only extends to 72 km away from the glacier terminus, a point which we refer to as the glacier head (Fig. 5). This bedrock profile corresponds to 5–6 kyr of ice flow history and approximately one ^{14}C half-life. Beyond the constraints from the bedrock profile, we had to make assumptions about the depth of the long-term transport (z_{deep}). Morse et al. (1998) provided a radar-based bedrock profile that includes the Taylor Glacier snow accumulation area (Baggenstos et al., 2018) north of the Taylor Dome – approximately 60 km upstream from the glacier head, where the Kavanaugh et al. (2009a) bedrock profile ends. Based on the bedrock profile from Morse et al. (1998), at the Taylor Glacier accumulation area, the depth of ~ 80 kyr ice (which corresponds to our 72 m sample) is ~ 575 m. We thus assumed that the depth of long-term transport (z_{deep}) for the 72 m sample under the best-estimate ablation rate scenario (which we define as the reference sample) is 575 m. For other ice parcel trajectories (i), we scaled the

depth of long-term transport (z_{deep}) as follows:

$$z_{deep}(i) = 575 - (z_{ref} - z_{head}(i)), \tag{5}$$

where z_{ref} represents the depth of the 72 m reference sample in the model at the glacier head under the best-estimate flowline (z_{ref} is 699 m), and z_{head} represents the depth of the ice parcel of interest at the glacier head. We assumed that the difference in depth between the reference sample and the sample of interest (i) at the glacier head and during long-term transport within the glacier is the same.

3.2 ^{14}C production in sample ice parcel

We used the model for in situ cosmogenic nuclide production by muons from Balco et al. (2008) and Balco (2017; model 1A in Balco, 2017), with all relevant parameters adjusted for ice (Fig. 1). This model in turn uses the Heisinger et al. (2002a, b) parameterizations described above and the additional altitude scaling of the muon fluxes described in Balco et al. (2008). We then used a forward model that numerically integrates the total ^{14}C in the ice sample along its flow path. For the initial condition, we assumed that, at the depth of long-term transport (z_{deep}), the ^{14}C concentration in the ice parcel is at the steady state, as follows:

$$\frac{dC}{dt}(\text{at } z_{deep}) = 0 = P_{neg}(z_{deep}) + P_{fast}(z_{deep}) - C_0\lambda. \tag{6}$$

The steady-state assumption means that, at z_{deep}, the rate of radioactive decay ($C_0\lambda$) is balanced by production from negative muon capture (P_{neg}) and fast muon reaction (P_{fast}). We
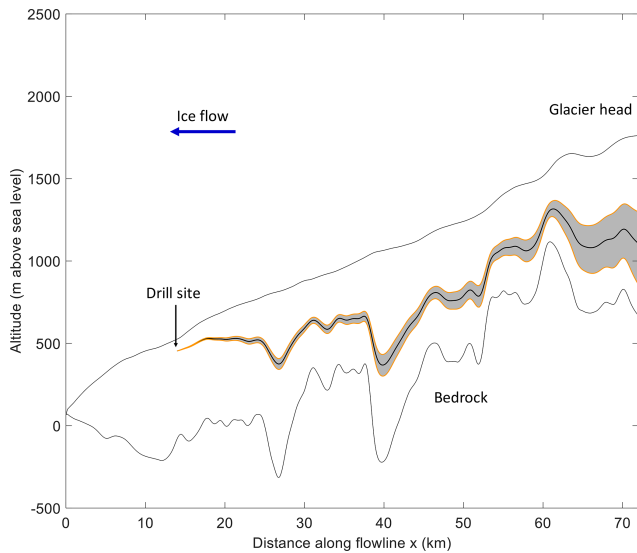
Figure 5. Example of the ice parcel back-trajectory and associated uncertainties. For the Monte Carlo estimate of uncertainties (Sect. 5.4.2), for each given sample depth (72 m in this figure), 10 000 back-trajectories are generated. Each back-trajectory corresponds to a different ablation rate scenario (the ablation rates are perturbed within their experimental measurement uncertainties to generate the scenarios). The shaded region represents the 68 % CI uncertainty envelope of the flow trajectory.

use a ^{14}C decay constant $\lambda = 1.216 \times 10^{-4}$ yr^{-1} for all our calculations (including the conversion of ^{14}C units in the previous section), which corresponds to the recommended ^{14}C half-life of 5700 years (Kutschera, 2019). For each ice parcel, we calculated the steady state, the initial ^{14}C concentration (C_0) from Eq. (6), and then used the following differential equation,

$$\frac{dC}{dt} = P_{\text{neg}}(z(t)) + P_{\text{fast}}(z(t)) - C\lambda, \tag{7}$$

to numerically integrate the ^{14}C concentration of the ice parcel along the flow trajectory. To avoid interference from spallogenic ^{14}C, we only considered samples with mean depths greater than 6.85 m depth.

We sampled the parameter space in a grid search approach to obtain the best-estimate values for muogenic ^{14}C production parameters σ_0 and f_{tot}. Using the best-estimate flow trajectory, we calculated the expected ^{14}C in the samples corresponding to all combinations of σ_0 and f_{tot}, with each of the parameters ranging between 0 % and 100 % of the values from Heisinger et al. (2002a, b). To save computational time, we first conducted the grid search at a coarse resolution of 10 % increments (Fig. S4a). The goodness of the fit ($\chi 2$) for each simulation was calculated as follows:

$$\chi^2 = \sum \frac{(C_{\text{obs}(z)} - C_{\text{exp}}(z))^2}{C_{\text{exp}}(z)}, \tag{8}$$

where $C_{\text{obs}}(z)$ is the measured total ^{14}C, and $C_{\text{exp}}(z)$ is the total ^{14}C (^{14}CO$_2$ + ^{14}CO + ^{14}CH$_4$; Fig. 3d) calculated by the forward model at sample depth z. To find more precise best-estimate σ_0 and f_{tot}, we conducted the grid search again at a higher resolution in 0.2 % increments from the Heisinger et al. (2002a, b) values near the $\chi 2$ minimum, between 0 and 0.0352 mb for σ_0 and 0 to 0.01 for f_{tot} (Fig. S4b).

To estimate the uncertainties in σ_0 and f_{tot}, we used a Monte Carlo sampling of model parameters. We assumed that the ablation rate uncertainties (Fig. S3) represent 2σ normally distributed uncertainties. We then perturbed the ablation rates within their uncertainties and generated a pool of 10 000 possible flow trajectories for each sample depth. However, in 69 out of 10 000 flow scenarios, the ice parcel back-trajectories hit the bedrock and became unphysical afterwards. These unphysical trajectories were removed from the pool of possible ice flow trajectories. Next, we started with the best-estimate σ_0 and f_{tot} and assumed a normally distributed and large 200 % (1σ) error for each parameter (Fig. S5a) as the prior distribution for the Monte Carlo method. We removed σ_0 and f_{tot} values that are below zero from the prior distribution because they are unphysical and conducted 100 000 Monte Carlo simulations using the forward ^{14}C production model. For each Monte Carlo simulation, we randomly picked one of the previously generated possible ice flow trajectories and a random pair of σ_0 and f_{tot} from the generated prior distributions (Fig. S5a). We then calculated the expected ^{14}C concentrations for each sample depth using the forward model and compared the model–data fit. We accept all pairs of σ_0 and f_{tot} values that produce the model-calculated total ^{14}C within the 95 % CI (7.8 ^{14}C atoms per gram of ice) and 67 % CI (3.9 ^{14}C atoms per gram of ice) analytical uncertainty of the best-fit, model-calculated total ^{14}C (black line in Fig. 6). The ranges of accepted σ_0 and f_{tot} pairs are shown in Fig. 7a as contours. The discussion about the selection of acceptance criteria for estimating σ_0 and f_{tot} uncertainties is provided in Sect. S1.4.

3.3 ^{14}CO production model in sample ice parcel

The in situ cosmogenic ^{14}CO production rates in ice are of specific interest, as discussed in Sect. 1.1. To characterize the ^{14}CO production rates, we introduced additional scaling factors f_{neg} and f_{fast} for negative muon and fast muon mechanisms, respectively, as tuned model parameters. The differential equation of Eq. (7) is modified into the following:

$$\frac{d(^{14}\text{CO})}{dt} = f_{\text{neg}} P_{\text{neg}}(z(t)) + f_{\text{fast}} P_{\text{fast}}(z(t)) - (^{14}\text{CO})\lambda. \tag{9}$$

We note that P_{neg} and P_{fast} in Eq. (9) are the total ^{14}C production rates calculated from the Balco et al. (2008) model. The scaling factors f_{neg} and f_{fast} each encompass two terms, i.e., one that adjusts the total ^{14}C production rates and another that accounts for the ^{14}CO fraction of total ^{14}C. The determination of best-estimate f_{neg} and f_{fast} and their uncer-
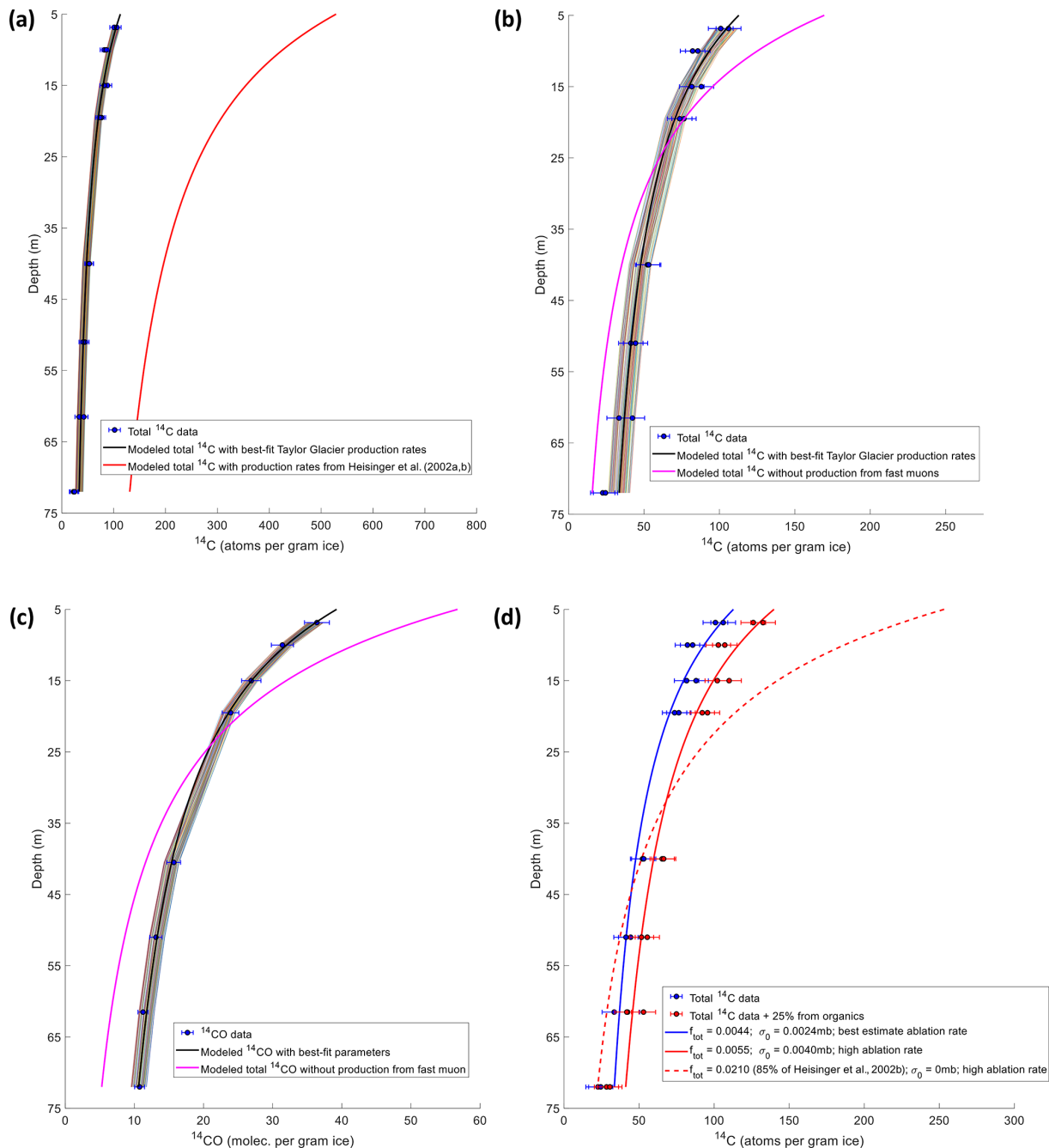
Figure 6. (a) Comparison between total ^{14}C measurements with modeled best-estimate σ_0 and f_{tot} parameters from this study and Heisinger et al. (2002a, b). **(b)** Comparison between total ^{14}C measurements with modeled best-estimate σ_0 and f_{tot} parameters from this study and modeled total ^{14}C with best-fit f_{tot} when σ_0 is forced to be zero. **(c)** Comparison between ^{14}CO measurements with modeled best-estimate f_{neg} and f_{fast} parameters from this study and modeled ^{14}CO with best-fit f_{neg} when f_{fast} is forced to be zero. **(d)** Comparison between total ^{14}C measurements with modeled best-estimate σ_0 and f_{tot} parameters from this study and modeled total ^{14}C from the sensitivity analyses when we assume 25 % contribution from organics and high ablation rate scenario (Fig. S9). The thin colored lines represent the 95 % CI envelope of the model results (corresponding to the contour plot of Fig. 7a for Fig. 6a and b and the contour plot of Fig. 7b for Fig. 6c). The error bars shown in the data are 95 % CI. In Fig. 6d, the solid blue line represents the ^{14}C profile from the modeled best-estimate f_{tot} and σ_0 under the best-estimate ablation rate. The solid red line represents the ^{14}C profile from the sensitivity analysis when f_{tot} and σ_0 are tuned to fit the total ^{14}C data that are scaled by 25 % to account for contribution from organics (red dots) under high ablation rate scenario (Fig. S9). The dashed red line represents the ^{14}C profile from the sensitivity analysis when f_{tot} is kept constant at 0.021 (which is the minimum value provided by Heisinger et al., 2002b) and $\sigma_0 = 0$ (which provides the best-fit against the data).
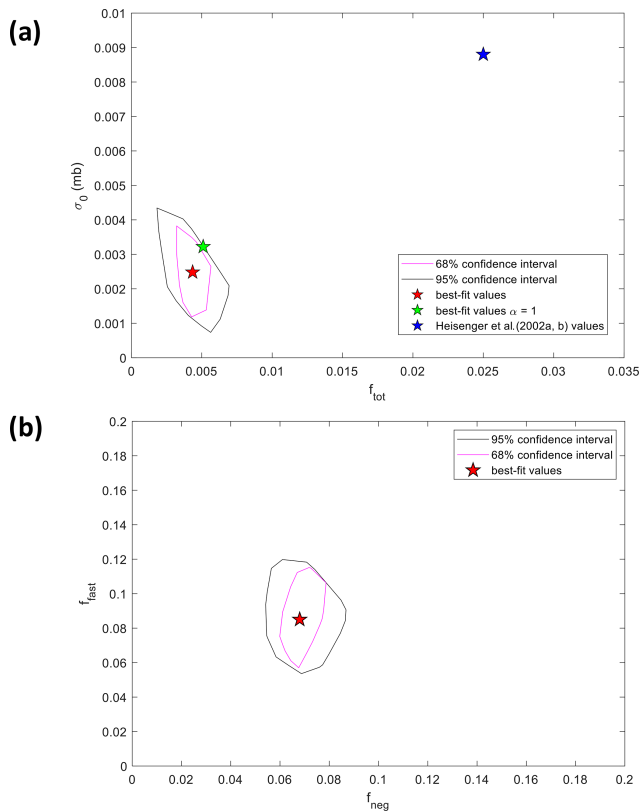
Figure 7. (a) The 68 % and 95 % CI contours of accepted σ_0 and f_{tot} values for total ^{14}C. **(b)** The 68 % and 95 % CI contours of accepted f_{neg} and f_{fast} values for ^{14}CO (see Sect. 5.4.3). For comparison, the σ_0 and f_{tot} values from Heisinger et al. (2002a, b) are shown as a blue star. The best-fit values for σ_0, f_{tot}, f_{neg}, and f_{fast} are shown as a red star in both figures. The best-fit values for σ_0 and f_{tot} are when α (energy scaling in Eq. 3).

tainties was similar to the approach for σ_0 and f_{tot} described above. The $\chi 2$ grid search was conducted with all combinations of f_{neg} and f_{fast} values ranging from 0 to 0.2 at 0.001 resolution (Fig. S4c). Similar to the total ^{14}C data, we used the average analytical uncertainty in the ^{14}CO sample set as the acceptance criteria for the Monte Carlo simulations to estimate the uncertainties of f_{neg} and f_{fast}. We accepted all sets of f_{neg} and f_{fast} from the 100 000 Monte Carlo simulations that yielded model-predicted ^{14}CO within 1.2 ^{14}CO molec. per gram of ice (95 % CI uncertainty) and 0.6 ^{14}CO molec. per gram of ice (68 % CI uncertainty) from the best-fit model (Fig. 8). Figure 7b shows (as contours) the accepted sets of f_{neg} and f_{fast} values.

3.4 Comparison with Scharffenbergbotnen ablation site

Van der Kemp et al. (2002) measured ^{14}CO$_2$ and ^{14}CO in ice from the Scharffenbergbotnen ice ablation site, Antarctica. Using a 1D ablation model, we examined how the esti-

mates of muogenic ^{14}C production rates from Taylor Glacier compare to the Scharffenbergbotnen data. We assumed that the measured ^{14}CO$_2$ plus ^{14}CO from Scharffenbergbotnen are comparable to our measurements of total ^{14}C in Taylor Glacier (since our data show that less than 0.3 % of the total ^{14}C from muon production forms ^{14}CH$_4$; Sect. 4.1). We then used the ^{14}C concentration from the deepest Scharffenbergbotnen sample (45 m) as the initial condition. In the 1D ablation model, the Scharffenbergbotnen ice parcel moves upward at a rate ($\mathrm{d}z/\mathrm{d}t$) equal to the ablation rate from stake measurements (Eq. 10; $a = 16 \pm 4 \,\text{cm yr}^{-1}$).

$$\frac{\mathrm{d}z}{\mathrm{d}t} = -a \tag{10}$$

$$\frac{\mathrm{d}C}{\mathrm{d}t} = P'_n(z(t)) + P'_{\text{neg}}(z(t)) + P'_{\text{fast}}(z(t)) - C\lambda. \tag{11}$$

The expected ^{14}C concentration in the ice is given by the differential equation (Eq. 11), where P'_n is the ^{14}C spallogenic production rate from Young et al. (2014; 12.0 ± 0.9 atoms per gram of quartz per year at the surface), first scaled to the SLHL production rate in ice (20.0 ± 1.5 atoms per gram of ice per year at the surface) accounting for the number of ^{16}O atoms per gram of ice vs. quartz (variable N; Eq. 3; Petrenko et al., 2016) and then to the production rate at the Scharffenbergbotnen site (1173 m above sea level or m a.s.l.) using the Lifton et al. (2014) LSDn nuclide-specific model ($P'_n = 71.2 \pm 3.6$ atoms per gram of ice per year at the surface). P'_{neg} and P'_{fast} are the muogenic production rates inferred from the Taylor Glacier data scaled to the elevation of Scharffenbergbotnen (1173 m a.s.l.), using the altitude scaling factors from Balco (2017). We also repeated this calculation for ^{14}CO only to compare the muogenic ^{14}CO production rates with the ^{14}CO data from Scharffenbergbotnen.

4 Results and discussion

4.1 Measured ^{14}C values and partitioning of ^{14}CO$_2$, ^{14}CO, and ^{14}CH$_4$

Table 1 and Fig. 3a–c show the depth profiles of ^{14}CO, ^{14}CH$_4$, and ^{14}CO$_2$ after all corrections. For the ^{14}CO$_2$ measurements, comparison with prior results that used a wet extraction approach (Fig. S6) confirms the caveats discussed by Petrenko et al. (2016) in that their ^{14}CO$_2$ measurements were uncertain and represent the upper bound. The ^{14}CH$_4/^{14}$CO ratios from the new samples (0.0074 ± 0.0004; 95 % CI; $n = 4$; from all samples below 19.5 m) appear to be constant within uncertainties (Fig. 4a), which is in agreement with earlier results (0.0076 ± 0.0004; 95 % CI; $n = 4$) from Petrenko et al. (2016). This confirms that the two muon reactions produce ^{14}C in a constant ^{14}CH$_4/^{14}$CO ratio. The ^{14}CO and ^{14}CO$_2$ fractions of total ^{14}C are also relatively constant at depth (Fig. 4b), suggesting that the two muon reactions produce all three ^{14}C species in constant ratios.
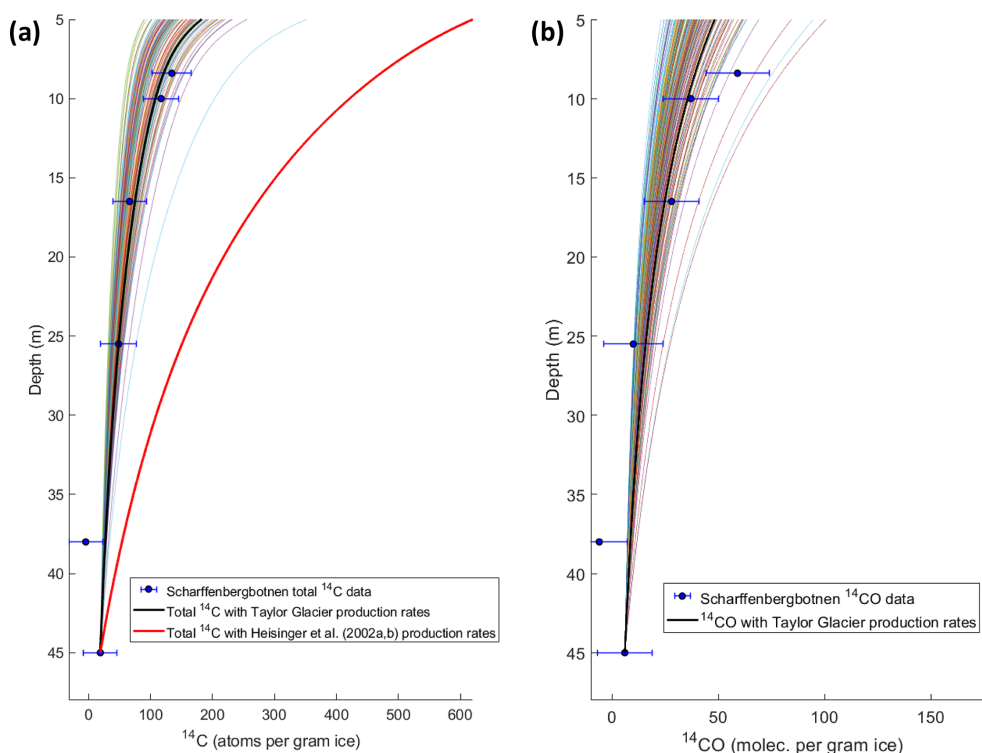
Figure 8. (a) Comparison between measured total ^{14}C from Scharffenbergbotnen, expected total ^{14}C using the production rates inferred in this study, and expected total ^{14}C using the Heisinger et al. (2002a, b) production rates. **(b)** Comparison between measured ^{14}CO from Scharffenbergbotnen and expected ^{14}CO, using the production rates inferred from Taylor Glacier. The colored lines in both figures represent the 95 % CI envelope of the model results. At the depths plotted in this figure (deeper than 5 m), the production from neutron-induced spallation is negligible.

For samples deeper than 6.85 m, on average 33.7 % (± 11.4 %; 95 % CI) of the produced cosmogenic ^{14}C becomes ^{14}CO and 66.1 % (± 11.5 %; 95 % CI) of the produced cosmogenic ^{14}C becomes $^{14}CO_2$ (Fig. b). The uncertainties of ^{14}CO and $^{14}CO_2$ fractions on the deepest samples (72 m depth) are relatively large because of the small $^{14}CO_2$ signal (11.8 to 13.6 $^{14}CO_2$ molec. per gram of ice) relative to the uncertainty in our measurements (± 7.8 $^{14}CO_2$ molec. per gram of ice; 95 % CI). The $^{14}CO_2$ fraction in samples that are deeper than 6.85 m (0.66 ± 0.12; 95 % CI) is also in agreement with prior reported $^{14}CO_2$ fraction of 0.69 from the Scharffenbergbotnen ablation site (Van der Kemp et al., 2002). Finally, the shallow samples (< 6 m ice equivalent) show higher $^{14}CH_4/^{14}CO$ ratios (Fig. 4a) and $^{14}CO_2$ / total ^{14}C ratios. This may indicate that spallation produces higher amounts of $^{14}CH_4$ and $^{14}CO_2$ relative to ^{14}CO (Petrenko et al., 2016) or that CO (and ^{14}CO) is not well-preserved in near-surface ice of the Taylor Glacier.

At depths where production from muons dominates (> 6 m), less than 0.3 % of the produced cosmogenic ^{14}C in ice forms $^{14}CH_4$ (Table 1; Fig. 4). Although the $^{14}CH_4$ measurement from the 10 m depth sample is not available (Petrenko et al., 2016), we still include the 10 m data point in the total ^{14}C dataset used to infer σ_0 and f_{tot} values and their un-

certainties. The contribution from $^{14}CH_4$ (which would have been on the order of ~ 0.2 $^{14}CH_4$ molec. per gram of ice; Fig. 3b) is insignificant compared to the uncertainty in total ^{14}C. We account for the lack of $^{14}CH_4$ measurement at this depth by scaling the total ^{14}C of the 10 m sample by a factor of 1.003 ± 0.003 (95 % CI; Table 1).

4.2 Inferred muogenic ^{14}C production rates in ice and comparison with production rates in quartz

Assuming that the majority of in situ cosmogenic ^{14}C in ice forms $^{14}CO_2$, ^{14}CO, and $^{14}CH_4$, the muogenic ^{14}C production parameters from Heisinger et al. (2002a, b; f_{tot} for negative muon capture and σ_0 for fast muon reaction) are well outside the confidence intervals of our measurements (Table 2; Figs. 6a and 7a). Using the larger uncertainty for $^{14}CO_2$ measurements obtained from step-by-step error propagation (Sect. S1.4; Fig. S7) does not change this conclusion. We calculated factors of 5.7 (3.6–13.9; 95 % CI) and 3.7 (2.0–11.9; 95 % CI) lower probability of the negative muon capture reaction (f_{tot}) and the reference cross section for the fast muon mechanism (σ_0) compared to the values given by Heisinger et al. (2002a, b).

Table 2. Probability of the ^{14}C production from stopped negative muons (f_{tot}), reference nuclear reaction cross section for production via fast muon interactions (σ_0), and total ^{14}C production rates in ice at the surface from the two muon reactions rescaled to SLHL (sea level high latitude), using the Lifton et al. (2014) LSDn scaling. All errors shown represent the 95 % confidence interval.

	Overall probability of negative muon capture reaction (f_{tot})	Reference nuclear reaction cross section (σ_0; mb)	SLHL total ^{14}C production rate in ice by negative muons (atoms per gram of ice per year)	SLHL total ^{14}C production rate in ice by fast muons (atoms per gram of ice per year)
This study	0.0044 (+0.0026/ − 0.0026)	0.0024 (+0.0017/ − 0.0018)	0.79 (+0.47/ − 0.46)	0.21 (+0.16/ − 0.15)
Heisinger et al. (2002a, b)	0.025 ± 0.004	0.0088 (+0.0098/ − 0.0088)	4.76 ± 0.76	0.74 (+0.83/ − 0.74)
Lupker et al. (2015)	0.024 (+0.006/ − 0.016)*	0 (+0.0118/ − 0)	4.70 (+1.22/ − 3.04)	0 (+1.52/ − 0)

* Adjusted to ice, assuming that the chemical compound factor (f_c) of ice is 1.0, and f_c for quartz is 0.704 (Heisinger et al., 2002b).

One possible explanation for the disagreement between our results and those of Heisinger et al. (2002a, b) is that our ^{14}C measurements (mostly either ^{14}CO or ^{14}CO$_2$, as ^{14}CH$_4$ only constitutes < 0.3 % of total ^{14}C) might be incorrect. However, in the following we thoroughly explore this possibility and argue that it is very unlikely. Our ^{14}CO measurements used a well-established analytical technique (e.g., Dyonisius et al., 2020; Hmiel et al., 2020; Petrenko et al., 2013, 2017, 2021). With regards to ^{14}CO measurements in air, this analytical technique (Petrenko et al., 2021) yields comparable results to independent, atmospheric ^{14}CO measurements from other research groups (e.g., Manning et al., 2005; Mak and Southon, 1998). We also have no reason to believe that there is a systematic loss of ^{14}CO during the ice melting process. The ice melting (wet extraction) ensures that all ^{14}C and CO are liberated. CO is not very soluble in water (the dissolved CO fraction at equilibrium in our system is on the order of 1 %), and we used the measured δXe/Kr (Table S4) to correct for the solubility effects for both [CO] and [CH$_4$]. The on-site field extraction within hours of the sample retrieval ensures that there is minimal post-coring gas loss. Finally, ice core and firn air ^{14}CO measurements at Summit, Greenland, are consistent within uncertainties with muogenic ^{14}CO production rates inferred from Taylor Glacier (Hmiel et al., 2020; Hmiel, 2020).

The sublimation technique used for our ^{14}CO$_2$ measurements also ensures the 100 % extraction efficiency of gases (Schmitt et al., 2011). We tested the system performance by sublimating BFI (bubble-free ice) samples while adding standard gases with known ^{14}CO$_2$ activities. As mentioned in Sect. 2.3.2, we used two standard gases with known ^{14}CO$_2$ activities, i.e., one with modern ^{14}CO$_2$ activity and the other with dead ^{14}CO$_2$ activity, when sublimating the BFI samples. There is neither a significant alteration in the CO$_2$ mole fraction and ^{14}CO$_2$ activity of both standard gases (Table S8) nor in the CO$_2$ mole fraction of the ice samples (Table S9), which suggests that the processes of sublimating ice and flowing gas through the system components do not result in loss of ^{14}CO$_2$. Finally, we can also rule out the possibility of post-coring ^{14}CO$_2$ loss. In a separate measurement campaign (Hmiel, 2020), we brought the sublimation system to Summit, Greenland, and sublimated the ice samples on site

(within days from the time when the ice core was drilled). We compared the ^{14}CO$_2$ from the on-site field sublimation with the ^{14}CO$_2$ from depth-adjacent replicates sublimated at the University of Rochester laboratory and found that they are indistinguishable within uncertainty.

We argue that another strong indication that our measurements are robust is the good agreement with independent results from Van der Kemp et al. (2002). Van der Kemp et al. (2002) measured ^{14}CO$_2$ and ^{14}CO in ice from the Scharffenbergbotnen ice ablation site using a dry extraction technique. The total measured ^{14}C values were significantly lower than the expected values, based on the stake-measured ablation rates and muogenic production rates based on laboratory irradiations of quartz targets (Heisinger et al., 2000a, b). Van der Kemp et al. (2002) initially hypothesized that the low extraction efficiency of dry mechanical extraction (which can result in an incomplete release of the in situ produced ^{14}C from the ice grains) might be responsible for this discrepancy. However, we used a sublimation method for our ^{14}CO$_2$ measurements and a melt extraction method for our ^{14}CO measurements; both methods guarantee that all in situ cosmogenic ^{14}C in the ice lattice is released. Figure 8 shows that the Scharffenbergbotnen data are consistent with the expected total ^{14}C and ^{14}CO from the Taylor-Glacier-derived production rates.

The good agreement in the ratio of ^{14}C compounds (^{14}CO$_2$ fraction is 0.66±0.12 in this study and 0.69 in Van der Kemp et al., 2002) suggests that our extraction methods and analytical techniques were not systematically losing ^{14}CO or ^{14}CO$_2$ (which would then bias the ^{14}CO$_2$ and ^{14}CO fraction). It is theoretically possible that both our measurements and Van der Kemp et al. (2002) are wrong. However, to produce the same ratio of ^{14}C compounds, it would require all three analytical systems from these studies to be systematically wrong in the same direction and by the same magnitude, which is highly unlikely. The good agreement between the Taylor Glacier and Scharffenbergbotnen data suggests that dry mechanical extraction used by Van der Kemp et al. (2002) is a valid technique for extracting ^{14}CO$_2$ and ^{14}CO from bubbly, non-clathrated ice cores. One possible explanation is that, after production, in situ ^{14}CO$_2$ and ^{14}CO quickly migrates from the ice matrix to the air bubbles. This result is consistent

with previous observations that the retention of in situ cosmogenic ^{14}C in firn grains is very low (Petrenko et al., 2013; Van der Kemp et al., 2000; Wilson and Donahue, 1990).

One way to reconcile our measurements and those of Van der Kemp et al. (2002) with the Heisinger et al. (2002a, b) production rates would be to have much higher (factor of 3 or greater) long-term (hundreds to thousands of years) ablation rates at Taylor Glacier and Scharffenbergbotnen compared to recent ablation stakes measurements. The ablation rate over the last 100 years is especially important with regards to in situ ^{14}C production rate from negative muon capture (Fig. S9). The ablation rate at blue ice areas is controlled by climate via a combination of temperature, insolation, and wind (mainly katabatic; e.g., Bintanja, 1999). To obtain much higher long-term ablation rates at both Taylor Glacier and Scharffenbergbotnen (which are on opposite sides of Antarctica), we would need either the temperatures to have dropped sharply in the last couple of decades, the winds to have slowed dramatically, or for insolation to have sharply decreased. However, the two deep ice cores nearest to Taylor Glacier, namely Taylor Dome (Steig et al., 2000) and RICE (Roosevelt Island Climate Evaluation; Bertler et al., 2018) have not shown large climate changes in the region over the last 1000 years. The European Project for Ice Coring in Antarctica (EPICA) Dronning Maud Land (EDML) ice core drilled nearby Scharffenbergbotnen blue ice area also has not shown large climate variability in the region over the Holocene period (EPICA Community Members, 2010). The glaciological survey of Taylor Glacier also indicated that the glacier is approximately at steady state, given the stake-measured ablation rates (Kavanaugh et al., 2009a, b). The 30-year record of weather observations over the McMurdo Dry Valleys area show that the recent climate in this region has been stable (Obryk et al., 2020). Finally, a 14-year-long observation study (Sinisalo et al., 2003) over the Scharffenbergbotnen blue ice area has also shown no significant recent change in the ablation rates. We thus argue that a large decrease in ablation rates in recent years, as compared to the long-term average (over the last hundreds to thousands of years), does not seem to be a realistic explanation.

For direct comparison with other studies, we used the scaling factors from the Lifton et al. (2014) LSDn model to calculate the corresponding sea level high latitude (SLHL) total ^{14}C and ^{14}CO-specific production rates in ice (Tables 2 and 3). Our estimates of the ^{14}CO-specific production rates agree with those of Petrenko et al. (2016), within errors (Table 3). Compared with the results from Petrenko et al. (2016), we also calculated a slightly smaller uncertainty in the ^{14}CO-specific production rate by negative muon capture (Table 3). We converted the Lupker et al. (2015) estimates of f_{tot} in quartz into f_{tot} for ice (Table 2), using the chemical compound factors (f_C) for quartz and ice from Heisinger et al. (2002b). With regards to the negative muon capture, the Lupker et al. (2015) estimate of f_{tot} is in close agreement with Heisinger et al. (2002b; Table 2). This result is sup-

ported by Balco (2017), who refitted the Leymon High data and obtained similar f_{tot} estimates. However, the high f_{tot} in Lupker et al. (2015), as compared to our result, was offset by their best σ_0 estimate of zero (lower than our result). For a direct comparison with results from Lupker et al. (2015), we fit our data, while forcing σ_0 (and hence ^{14}C production from fast muons) to be zero (Fig. 6b) and cannot find a scenario with reasonable model–data agreement.

Because of the relatively large uncertainty in the ^{14}CO$_2$ measurements, the total ^{14}C data still allow σ_0 to be close to zero, given a sufficiently large f_{tot} (Fig. 7a). However, our ^{14}CO data (which have much lower relative uncertainties and use a more established measurement technique) unambiguously show that σ_0 and ^{14}C production from fast muons cannot be zero (Figs. 8, 7b). As discussed in Lupker et al. (2015) and Balco (2017), the ^{14}C data from the 15.5 m Leymon High quartzite core might not cover the depth range in which production from fast muons dominates. In contrast, when integrated over the whole flow history, production from fast muons represents the dominant source of ^{14}C in our deeper samples. The very high-end estimate of our reference nuclear reaction cross section σ_0 (for ^{14}C production from fast muons) is still within the large uncertainty of σ_0 from both Heisinger et al. (2002a) and Lupker et al. (2015; Table 2). However, our estimated total probability of negative muon capture (f_{tot}; and hence the ^{14}C production rate from negative muon) is well outside the confidence intervals of f_{tot} reported by both Heisinger et al. (2002b) and Lupker et al. (2015; Table 2).

One caveat to our estimated in situ muogenic ^{14}C production rates in ice (and that of Van der Kemp et al., 2002) is that the total ^{14}C from the gas species we measured (^{14}CO, ^{14}CO$_2$, and ^{14}CH$_4$) might not account for all the muogenic in situ ^{14}C. Although ^{14}CO$_2$ and ^{14}CO likely constitute the large majority (Lal et al., 1997, 2000), a small amount of in situ ^{14}C can also form ^{14}C-bearing organic materials. Measurements of ^{14}C in organic carbon from alpine ice for the purpose of radiocarbon dating have shown elevated ^{14}C values attributed to in situ cosmogenic production (Fang et al., 2021; Hoffmann, 2016). A laboratory irradiation experiment of glacier ice with an artificial neutron flux showed that 11 %–25 % of produced ^{14}C form organic compounds (Hoffmann, 2016). Earlier work involving the irradiation of ice samples to produce ^{14}C (e.g., Roessler et al., 1984) also found that organics accounted for a minor fraction of the total ^{14}C. However, we are not aware of any existing studies that specifically investigated production of ^{14}C-bearing organic materials in ice from muons. Measuring ^{14}C in organic compounds is unfortunately beyond the scope of this study, as it requires an entirely different analytical setup.

Another possible explanation for the disagreement is that the 2D ice flow model (and thus the time-dependent exposure history of the ice parcels) might be inaccurate. In the following, we conducted sensitivity analyses to combine both uncertainties by using the $+2.4\sigma$ maximum ablation rate sce-

Table 3. ^{14}CO-specific surface production rates in ice from the two muon mechanisms normalized to the SLHL (sea level high latitude) site using the Lifton et al. (2014) LSDn scaling. All errors shown represent the 95 % confidence interval.

	SLHL ^{14}CO production rate in ice by negative muons (molec. per gram of ice per year)	SLHL ^{14}CO production rate in ice by fast muons (molec. per gram of ice per year)
This study	0.310 (+0.075/ − 0.063)	0.063 (+0.022/ − 0.018)
Petrenko et al. (2016)	0.24 (+0.14/ − 0.14)	0.053 (+0.028/ − 0.028)

nario (which corresponds to the deepest physically possible ice trajectory; Fig. S8) and scaling our total ^{14}C upward by 25 % to account for the in situ produced ^{14}C in organics (red dots in Fig. 6d). First, we kept f_{tot} as a constant ($f_{tot} = 0.021$, which is the minimum f_{tot} from the reported uncertainty in Heisinger et al., 2002b) and tuned σ_0 to fit the measurements (dashed red line in Fig. 6d) under the high ablation rate scenario. We find that the best-fit σ_0 (and in situ ^{14}C production from fast muon) is zero. The modeled total ^{14}C under this scenario underestimates the total ^{14}C at lower depths where production from fast muon dominates (> 20 m depth) and overestimates the total ^{14}C at depths where production from negative muon capture dominates (< 20 m depth). This means that, even under these extreme scenarios, the ^{14}C production rate from negative muon capture has to be lower than the lower-bound estimate of Heisinger et al. (2002b), and some production from fast muons is needed to compensate for the lower production rate from negative muon capture to improve the fit. We then repeated our grid search approach (Sect. 3.2) to find the best-fit f_{tot} and σ_0 that correspond to the 25 % higher total ^{14}C and maximum ablation rate scenario (solid red line in Fig. 6d). The best-fit f_{tot} is 0.0055, which is 22 % of the Heisinger et al., 2002b, value) and the best-fit σ_0 is 0.0040 mb (which is 46 % of the Heisinger et al., 2002a, value). We note that these values are within uncertainties in our original best-fit f_{tot} and σ_0 (Table 2) and still cannot be reconciled with values from Heisinger et al. (2002a, b). We conclude that additional uncertainties from the ice flow history and ^{14}C contribution from organics likely cannot reconcile the difference between the negative muon capture ^{14}C production rate inferred by our data and that of Heisinger et al. (2002b).

In their experimental determination of the ^{14}C production rate by fast muons, Heisinger et al. (2002a) used a single muon energy of 190 GeV ($\sigma(E)$). The reference nuclear reaction cross section at 1 GeV (σ_0) was then scaled using the following equation:

$$\sigma(E) = \sigma_0 \overline{E}^{\alpha}, \tag{12}$$

where α is a power factor that describes the energy dependence of the cross section (unitless). However, the mean muon energy ($\overline{E}$) of 190 GeV used by Heisinger et al. (2002a) and the muon flux intensity were much higher than those expected in the first few hundred meters of ice in natural settings (for the top 200 m of Taylor Glacier, $\overline{E} =$

32 GeV; Fig. S10). It may be possible that the power factor α of 0.75 is incorrect. Balco (2017) has tried fitting the calibration data with $\alpha = 1$ (which simplifies Eq. 12 into a linear relationship between σ and E). Following Balco (2017), we conducted a sensitivity analysis, fitting our data with similar methods to those described above but with $\alpha = 1$. Increasing α from 0.75 to 1, while keeping σ_0 constant, reduces the overall ^{14}C production rate from fast muons (Fig. S13). To compensate for the lower production rate from fast muons, the new best-fit σ_0 is now 0.0032 mb, which is 29.8 % higher than the best-fit σ_0 when $\alpha = 0.75$ and 36.6 % that of Heisinger et al. (2002b) value. The best-fit f_{tot} (overall probability of ^{14}C production from negative muon capture) becomes 0.0051, which is 17.2 % higher than the best-fit f_{tot} when $\alpha = 0.75$ and 20.4 % that of Heisinger et al. (2002a) value (Fig. 7a). These values are within the uncertainties in the f_{tot} and σ_0 derived with $\alpha = 0.75$ that we presented (Table 2; Fig. 7a) and still cannot be reconciled with original Heisinger et al. (2002a, b) values.

5 Conclusions

This study presents ^{14}CO$_2$ measurements in ablating ice obtained via a new ice sublimation technique, combined with ^{14}CO and ^{14}CH$_4$ measurements obtained from a well-established large-volume melt–extraction method to estimate the species-specific and total in situ muogenic ^{14}C production rates in ice. Under the assumption that the majority of in situ ^{14}C in ice exists as ^{14}CO, ^{14}CO$_2$, and ^{14}CH$_4$, we estimated lower muogenic in situ ^{14}C production rates in ice (by a factor of 5.7 (3.6–13.9) and 3.7 (2.0–11.9) with 95 % CI for negative muon capture and fast muon interactions, respectively) compared to values inferred from laboratory irradiation experiments (Heisinger et al., 2002a, b) and measurements in quartz (Lupker et al., 2015; Balco 2017). Prior ice core measurements from Scharffenbergbotnen (Van der Kemp et al., 2002) obtained with an independent technique also appear to be consistent with these lower muogenic ^{14}C production rates in ice. This comparison with the Van der Kemp et al. (2002) results also suggests that a dry extraction technique appears to release essentially all in situ ^{14}C in bubbly (non-clathrated) ice.

At present, there does not appear to be a way to reconcile our Taylor Glacier ice core results and the independent

ice core measurements from Scharffenbergbotnen (Van der Kemp et al., 2002) with the muogenic ^{14}C production rates determined in quartz (Heisinger et al., 2002a, b; Lupker et al., 2015). This is a problem that needs further investigation, and we recommend that future studies address this via laboratory muon irradiation experiments involving both ice and quartz targets and studies that include a quantification of the organic fraction of muogenic ^{14}C in ice.

Finally, the constraints on muogenic ^{14}C production rates in ice and the partitioning between the in situ produced ^{14}C-bearing gas species provided by this study will allow for future measurements of ^{14}C-containing gases in other ice cores to be used for several applications, including using ^{14}CO$_2$ measurements for the absolute dating of the bubbles in ice cores (Andree et al., 1984; Van De Wal et al., 1994) and using ^{14}CO measurements to either constrain the past oxidative capacity of the atmosphere (Brenninkmeijer et al., 1992; Petrenko et al., 2021) or reconstruct the past cosmic ray flux (BenZvi et al., 2019).

References

Ahn, J., Brook, E. J., and Howell, K.: A high-precision method for measurement of paleoatmospheric CO$_2$ in small polar ice samples, J. Glaciol., 55, 499–506, 2009.

Andree, M., Moor, E., Beer, J., Oeschger, H., Stauffer, B., Bonani, G., Hofmann, H. J., Morenzoni, E., Nessi, M., and Suter, M.: ^{14}C dating of polar ice, Nucl. Instrum. Meth. B, 5, 385–388, 1984.

Baggenstos, D., Bauska, T. K., Severinghaus, J. P., Lee, J. E., Schaefer, H., Buizert, C., Brook, E. J., Shackleton, S., and Petrenko, V. V.: Atmospheric gas records from Taylor Glacier, Antarctica, reveal ancient ice with ages spanning the entire last glacial cycle, Clim. Past, 13, 943–958, https://doi.org/10.5194/cp-13-943-2017, 2017.

Baggenstos D., Severinghaus J. P., Mulvaney R., McConnell J. R., Sigl M., Maselli O., Petit J.-R., Grente B., and Steig E. J.: A horizontal ice core from Taylor Glacier, its implications for Antarctic climate history, and an improved Taylor Dome ice core time scale, Paleoceanogr. Paleoclimatol., 33, 778–794, 2018.

Balbas, A. M. and Farley, K. A.: Constraining in situ cosmogenic nuclide paleo-production rates using sequential lava flows during a paleomagnetic field strength low, Chem. Geol., 532, 119355, https://doi.org/10.1016/j.chemgeo.2019.119355, 2020.

Balco, G.: Production rate calculations for cosmic-ray-muon-produced ^{10}Be and ^{26}Al benchmarked against geological calibration data, Quat. Geochronol., 39, 150–173, 2017.

Balco, G.: Glacier change and paleoclimate applications of cosmogenic-nuclide exposure dating, Annu. Rev. Earth. Pl. Sc., 48, 21–48, 2020.

Balco, G., Stone, J. O., Lifton, N. A., and Dunai, T. J.: A complete and easily accessible means of calculating surface exposure ages or erosion rates from ^{10}Be and ^{26}Al measurements, Quat. Geochronol., 3, 174–195, 2008.

Bauska, T. K., Baggenstos, D., Brook, E. J., Mix, A. C., Marcott, S. A., Petrenko, V. V., Schaefer, H., Severinghaus, J. P., and Lee, J. E.: Carbon isotopes characterize rapid changes in atmospheric carbon dioxide during the last deglaciation, P. Natl. Acad. Sci. USA, 113, 3465–3470, 2016.

BenZvi, S., Petrenko, V. V., Hmiel, B., Dyonisius, M., Smith, A. M., Yang, B., and Hua, Q.: Obtaining a History of the Flux of Cosmic Rays using In Situ Cosmogenic ^{14}C Trapped in Polar Ice, arXiv [preprint], https://doi.org/10.48550/arXiv.1909.07994, 2019.

Bereiter, B., Stocker, T. F., and Fischer, H.: A centrifugal ice microtome for measurements of atmospheric CO_2 on air trapped in polar ice cores, Atmos. Meas. Tech., 6, 251–262, https://doi.org/10.5194/amt-6-251-2013, 2013.

Bereiter, B., Eggleston, S., Schmitt, J., Nehrbass-Ahles, C., Stocker, T. F., Fischer, H., Kipfstuhl, S., and Chappellaz, J.: Revision of the EPICA Dome C CO_2 record from 800 to 600 kyr before present, Geophys. Res. Lett., 42, 541–549, 2015.

Bereiter, B., Kawamura, K., and Severinghaus, J. P.: New Methods for Measuring Atmospheric Heavy Noble Gas Isotope and Elemental Ratios in Ice Core Samples, Rapid. Commun. Mass. Sp., 32, 801–814, 2018.

Bertler, N. A. N., Conway, H., Dahl-Jensen, D., Emanuelsson, D. B., Winstrup, M., Vallelonga, P. T., Lee, J. E., Brook, E. J., Severinghaus, J. P., Fudge, T. J., Keller, E. D., Baisden, W. T., Hindmarsh, R. C. A., Neff, P. D., Blunier, T., Edwards, R., Mayewski, P. A., Kipfstuhl, S., Buizert, C., Canessa, S., Dadic, R., Kjær, H. A., Kurbatov, A., Zhang, D., Waddington, E. D., Baccolo, G., Beers, T., Brightley, H. J., Carter, L., Clemens-Sewall, D., Ciobanu, V. G., Delmonte, B., Eling, L., Ellis, A., Ganesh, S., Golledge, N. R., Haines, S., Handley, M., Hawley, R. L., Hogan, C. M., Johnson, K. M., Korotkikh, E., Lowry, D. P., Mandeno, D., McKay, R. M., Menking, J. A., Naish, T. R., Noerling, C., Ollive, A., Orsi, A., Proemse, B. C., Pyne, A. R., Pyne, R. L., Renwick, J., Scherer, R. P., Semper, S., Simonsen, M., Sneed, S. B., Steig, E. J., Tuohy, A., Venugopal, A. U., Valero-Delgado, F., Venkatesh, J., Wang, F., Wang, S., Winski, D. A., Winton, V. H. L., Whiteford, A., Xiao, C., Yang, J., and Zhang, X.: The Ross Sea Dipole – temperature, snow accumulation and sea ice variability in the Ross Sea region, Antarctica, over the past 2700 years, Clim. Past, 14, 193–214, https://doi.org/10.5194/cp-14-193-2018, 2018.

Bintanja, R.: On the glaciological, meteorological, and climatological significance of Antarctic blue ice areas, Rev. Geophys., 37, 337–359, https://doi.org/10.1029/1999RG900007, 1999.

Bliss, A. K., Cuffey, K. M., and Kavanaugh, J. L.: Sublimation and surface energy budget of Taylor Glacier, Antarctica, J. Glaciol., 57, 684–696, 2011.

Brenninkmeijer, C. A. M., Manning, M. R., Lowe, D. C., Wallace, G., Sparks, R. J., and Volz-Thomas, A.: Interhemispheric asymmetry in OH abundance inferred from measurements of atmospheric ^{14}CO, Nature, 356, 50–52, 1992.

Buizert, C.: ICE CORE METHODS – Studies of Firn Air, in: Encyclopedia of Quaternary Science (Second Edition), edited by: Mock, S. A. E. J., Elsevier, Amsterdam, 361–372, https://doi.org/10.1016/B978-0-444-53643-3.00330-7, 2013.

Buizert, C., Petrenko, V. V., Kavanaugh, J. L., Cuffey, K. M., Lifton, N. A., Brook, E. J., and Severinghaus, J. P.: In situ cosmogenic radiocarbon production and 2-D ice flow line model-

ing for an Antarctic blue ice area, J. Geophys. Res., 117, F2, https://doi.org/10.1029/2011JF002086, 2012.

Buizert, C., Sowers, T., and Blunier, T.: Assessment of diffusive isotopic fractionation in polar firn, and application to ice core trace gas records, Earth. Planet. Sc. Lett., 361, 110–119, 2013.

Buizert, C., Baggenstos, D., Jiang, W., Purtschert, R., Petrenko, V. V., Lu, Z.-T., Müller, P., Kuhl, T., Lee, J., Severinghaus, J. P., and Brook, E. J.: Radiometric 81Kr dating identifies 120,000-year-old ice at Taylor Glacier, Antarctica, P. Natl. Aacad. Sci. USA, 111, 6876–6881, 2014.

Delmas, R. J., Ascencio, J.-M., and Legrand, M.: Polar ice evidence that atmospheric CO_2 20,000 yr BP was 50 % of present, Nature, 284, 155–157, 1980.

Dyonisius, M. N. and Petrenko, V.: Taylor Glacier in situ cosmogenic ^{14}C data, U.S. Antarctic Program (USAP) Data Center [data set], https://www.usap-dc.org/view/project/p0000283, last access: 16 February 2023.

Dyonisius, M. N., Petrenko, V. V., Smith, A. M., Hua, Q., Yang, B., Schmitt, J., Beck, J., Seth, B., Bock, M., Hmiel, B., Vimont, I., Menking, J. A., Shackleton, S. A., Baggenstos, D., Bauska, T. K., Rhodes, R. H., Sperlich, P., Beaudette, R., Harth, C., Kalk, M., Brook, E. J., Fischer, H., Severinghaus, J. P., and Weiss, R. F.: Old carbon reservoirs were not important in the deglacial methane budget, Science, 367, 907–910, https://doi.org/10.1126/science.aax0504, 2020.

EPICA Community Members: Stable oxygen isotopes of ice core EDML, PANGAEA, https://doi.org/10.1594/PANGAEA.754444, 2010.

Fang, L., Jenk, T. M., Singer, T., Hou, S., and Schwikowski, M.: Radiocarbon dating of alpine ice cores with the dissolved organic carbon (DOC) fraction, The Cryosphere, 15, 1537–1550, https://doi.org/10.5194/tc-15-1537-2021, 2021.

Fenton, C. R., Niedermann, S., Dunai, T., and Binnie, S. A.: The SPICE project: Production rates of cosmogenic ^{21}Ne, ^{10}Be, and ^{14}C in quartz from the 72 ka SP basalt flow, Quat. Geochronol., 54, 101019, https://doi.org/10.1016/j.quageo.2019.101019, 2019.

Fireman, E. L. and Norris, T. L.: Ages and composition of gas trapped in Allan Hills and Byrd core ice, Earth Planet. Sc. Lett., 60, 339–350, https://doi.org/10.1016/0012-821X(82)90072-3, 1982.

Gosse, J. C. and Phillips, F. M.: Terrestrial in situ cosmogenic nuclides: theory and application, Quaternary Sci. Rev., 20, 1475–1560, 2001.

Heisinger, B., Lal, D., Jull, A. J. T., Kubik, P., Ivy-Ochs, S., Neumaier, S., Knie, K., Lazarev, V., and Nolte, E.: Production of selected cosmogenic radionuclides by muons: 1. Fast muons, Earth. Planet. Sc. Lett., 200, 345–355, 2002a.

Heisinger, B., Lal, D., Jull, A. J. T., Kubik, P., Ivy-Ochs, S., Knie, K., and Nolte, E.: Production of selected cosmogenic radionuclides by muons: 2. Capture of negative muons, Earth. Planet. Sc. Lett., 200, 357–369, 2002b.

Herron, M. M. and Langway, C. C.: Firn densification: an empirical model, J. Glaciol., 25, 373–385, 1980.

Hippe, K.: Constraining processes of landscape change with combined in situ cosmogenic ^{14}C-^{10}Be analysis, Quaternary Sci. Rev., 173, 1–19, 2017.

Hippe, K. and Lifton, N. A.: Calculating Isotope Ratios and Nuclide Concentrations for In Situ Cosmogenic ^{14}C Analyses, Radiocarbon, 56, 1167–1174, 2014.

Hmiel, B.: A Study of In Situ Cosmogenic ^{14}C and Pale-oatmospheric ^{14}CH$_4$ From Accumulating Ice at Summit, Greenland, PhD Thesis, University of Rochester, https://search.proquest.com/openview/35ca42e03ab8952d735e2962e9fcd3cc/1?pq-origsite=gscholar&cbl=18750&diss=y (last access: 27 January 2023), 2020.

Hmiel, B., Petrenko, V. V., Dyonisius, M., Buizert, C., Smith, A. M., Place, P. F., Harth, C. M., Beaudette, R., Hua, Q., Yang, B., Vimont, I., Michel, S. E., Severinghaus, J. P., Etheridge, D. M., Bromley, T. M., Schmitt, J., Fain, X., Weiss, R. F., and Dlugokencky, E. J.: Preindustrial ^{14}CH$_4$ indicates that anthropogenic fossil CH$_4$ emissions are underestimated, Nature, 578, 409–412, 2020.

Hoffmann, M.: Micro radiocarbon dating of the particulate organic carbon fraction in Alpine glacier ice: method refinement, critical evaluation and dating applications, PhD Dissertation, University of Heidelberg, http://archiv.ub.uni-heidelberg.de/volltextserver/20712/1/Dissertation_Helene_Hoffmann.pdf (last access: 27 January 2023), 2016.

Hogg, A. G., Heaton, T. J., Hua, Q., Palmer, J. G., Turney, C. S., Southon, J., Bayliss, A., Blackwell, P. G., Boswijk, G., and Ramsey, C. B.: SHCal20 Southern Hemisphere calibration, 0–55,000 years cal BP, Radiocarbon, 62, 759–778, 2020.

Jull, A. T., Lal, D., Donahue, D. J., Mayewski, P., Lorius, C., Raynaud, D., and Petit, J. R.: Measurements of cosmic-ray-produced ^{14}C in firn and ice from Antarctica, Nucl. Instrum. Meth. B, 92, 326–330, 1994.

Kavanaugh, J. L. and Cuffey, K. M.: Dynamics and mass balance of Taylor Glacier, Antarctica: 2. Force balance and longitudinal coupling, J. Geophys. Res., 114, F04011, https://doi.org/10.1029/2009JF001329, 2009.

Kavanaugh, J. L., Cuffey, K. M., Morse, D. L., Conway, H., and Rignot, E.: Dynamics and mass balance of Taylor Glacier, Antarctica: 1. Geometry and surface velocities, J. Geophys. Res., 114, F04010, https://doi.org/10.1029/2009JF001309, 2009a.

Kavanaugh, J. L., Cuffey, K. M., Morse, D. L., Bliss, A. K., and Aciego, S. M.: Dynamics and mass balance of Taylor Glacier, Antarctica: 3. State of mass balance, J. Geophys. Res., 114, F04012, https://doi.org/10.1029/2009JF001331, 2009b.

Kuhl, T. W., Johnson, J. A., Shturmakov, A. J., Goetz, J. J., Gibson, C. J., and Lebar, D. A.: A new large-diameter ice-core drill: the Blue Ice Drill, Ann. Glaciol., 55, 1–6, 2014.

Kutschera, W.: The Half-Life of ^{14}C–Why Is It So Long?, Radiocarbon, 61, 1135–1142, 2019.

Lal, D. and Jull, A. J. T.: On determining ice accumulation rates in the past 40,000 years using in situ cosmogenic ^{14}C, Geophys. Res. Lett., 17, 1303–1306, 1990.

Lal, D. and Peters, B.: Cosmic Ray Produced Radioactivity on the Earth, in: Kosmische Strahlung II/Cosmic Rays II, edited by: Sitte, K., Springer Berlin Heidelberg, Berlin, Heidelberg, 551–612, https://doi.org/10.1007/978-3-642-46079-1_7, 1967.

Lal, D., Jull, A. J. T., Donahue, D. J., Burtner, D., and Nishiizumi, K.: Polar ice ablation rates measured using in situ cosmogenic ^{14}C, Nature, 346, 350–352, 1990.

Lal, D., Jull, A. T., Burr, G. S., and Donahue, D. J.: Measurements of in situ ^{14}C concentrations in Greenland Ice Sheet Project 2 ice covering a 17-kyr time span: Implications to ice flow dynamics, J. Geophys. Res.-Oceans, 102, 26505–26510, 1997.

Lal, D., Jull, A. J. T., Burr, G. S., and Donahue, D. J.: On the characteristics of cosmogenic in situ ^{14}C in some GISP2 Holocene and late glacial ice samples, Nucl. Instrum. Meth. B, 172, 623–631, 2000.

Lal, D., Jull, A. J. T., Donahue, D. J., Burr, G. S., Deck, B., Jouzel, J., and Steig, E.: Record of cosmogenic in situ produced ^{14}C in Vostok and Taylor Dome ice samples: Implications for strong role of wind ventilation processes, J. Geophys. Res., 106, 31933–31941, 2001.

Lee, J. E., Edwards, J. S., Schmitt, J., Fischer, H., Bock, M., and Brook, E. J.: Excess methane in Greenland ice cores associated with high dust concentrations, Geochim. Cosmochim. Ac., 270, 409–430, 2020.

Lifton, N., Sato, T., and Dunai, T. J.: Scaling in situ cosmogenic nuclide production rates using analytical approximations to atmospheric cosmic-ray fluxes, Earth. Planet. Sc. Lett, 386, 149–160, 2014.

Lifton, N., Caffee, M., Finkel, R., Marrero, S., Nishiizumi, K., Phillips, F. M., Goehring, B., Gosse, J., Stone, J., Schaefer, J., Theriault, B., Jull, A. J. T., and Fifield, K.: In situ cosmogenic nuclide production rate calibration for the CRONUS-Earth project from Lake Bonneville, Utah, shoreline features, Quat. Geochronol., 26, 56–69, 2015.

Lupker, M., Hippe, K., Wacker, L., Kober, F., Maden, C., Braucher, R., Bourlès, D., Romani, J. R. V., and Wieler, R.: Depth-dependence of the production rate of in situ ^{14}C in quartz from the Leymon High core, Spain, Quat. Geochronol., 28, 80–87, 2015.

Lüthi, D., Le Floch, M., Bereiter, B., Blunier, T., Barnola, J.-M., Siegenthaler, U., Raynaud, D., Jouzel, J., Fischer, H., Kawamura, K., and Stocker, T. F.: High-resolution carbon dioxide concentration record 650,000–800,000 years before present, Nature, 453, 379, https://doi.org/10.1038/nature06949, 2008.

Mak, J. E. and Southon, J. R.: Assessment of tropical OH seasonality using atmospheric ^{14}CO measurements from Barbados, Geophys. Res. Lett., 25, 2801–2804, 1998.

Manning, M. R., Lowe, D. C., Moss, R. C., Bodeker, G. E., and Allan, W.: Short-term variations in the oxidizing power of the atmosphere, Nature, 436, 1001, https://doi.org/10.1038/nature03900, 2005.

Obryk, M. K., Doran, P. T., Fountain, A. G., Myers, M., and McKay, C. P.: Climate From the McMurdo Dry Valleys, Antarctica, 1986–2017: Surface Air Temperature Trends and Redefined Summer Season, J. Geophys. Res.-Atmos., 125, e2019JD032180, https://doi.org/10.1029/2019JD032180, 2020.

Petrenko, V. V., Severinghaus, J. P., Smith, A. M., Riedel, K., Baggenstos, D., Harth, C., Orsi, A., Hua, Q., Franz, P., Takeshita, Y., Brailsford, G. W., Weiss, R. F., Buizert, C., Dickson, A., and Schaefer, H.: High-precision ^{14}C measurements demonstrate production of in situ cosmogenic ^{14}CH$_4$ and rapid loss of in situ cosmogenic ^{14}CO in shallow Greenland firn, Earth Planet. Sc. Lett., 365, 190–197, https://doi.org/10.1016/j.epsl.2013.01.032, 2013.

Petrenko, V. V., Smith, A. M., Schaefer, H., Riedel, K., Brook, E., Baggenstos, D., Harth, C., Hua, Q., Buizert, C., Schilt, A., Fain, X., Mitchell, L., Bauska, T., Orsi, A., Weiss, R. F., and Severinghaus, J. P.: Minimal geological methane emissions during the

Younger Dryas–Preboreal abrupt warming event, Nature, 548, 443–446, https://doi.org/10.1038/nature23316, 2017.

Petrenko, V. V., Smith, A. M., Crosier, E. M., Kazemi, R., Place, P., Colton, A., Yang, B., Hua, Q., and Murray, L. T.: An improved method for atmospheric ^{14}CO measurements, Atmos. Meas. Tech., 14, 2055–2063, https://doi.org/10.5194/amt-14-2055-2021, 2021.

Sinisalo, A., Moore, J. C., Wal, R. S. W. V. D., Bintanja, R., and Jonsson, S.: A 14 year mass-balance record of a blue-ice area in Antarctica, Ann. Glaciol., 37, 213–218, https://doi.org/10.3189/172756403781816013, 2003.

Steig, E. J., Morse, D. L., Waddington, E. D., Stuiver, M., Grootes, P. M., Mayewski, P. A., Twickler, M. S., and Whitlow, S. I.: Wisconsinan and Holocene Climate History from an Ice Core at Taylor Dome, Western Ross Embayment, Antarctica, Geogr. Ann. A, 82, 213–235, https://doi.org/10.1111/j.0435-3676.2000.00122.x, 2000.

Menking, J. A., Brook, E. J., Shackleton, S. A., Severinghaus, J. P., Dyonisius, M. N., Petrenko, V., McConnell, J. R., Rhodes, R. H., Bauska, T. K., Baggenstos, D., Marcott, S., and Barker, S.: Spatial pattern of accumulation at Taylor Dome during Marine Isotope Stage 4: stratigraphic constraints from Taylor Glacier, Clim. Past, 15, 1537–1556, https://doi.org/10.5194/cp-15-1537-2019, 2019.

Miller, J. B., Mack, K. A., Dissly, R., White, J. W., Dlugokencky, E. J., and Tans, P. P.: Development of analytical methods and measurements of 13C/12C in atmospheric CH_4 from the NOAA Climate Monitoring and Diagnostics Laboratory Global Air Sampling Network, J. Geophys. Res-Atmos, 107, https://doi.org/10.1029/2001JD000630, 2002.

Mitchell, L., Brook, E., Lee, J. E., Buizert, C., and Sowers, T.: Constraints on the Late Holocene Anthropogenic Contribution to the Atmospheric Methane Budget, Science, 342, 964–966, 2013.

Mitchell, L. E., Brook Edward J., Sowers Todd, McConnell J. R., and Taylor Kendrick: Multidecadal variability of atmospheric methane, 1000–1800 C.E., J. Geophys. Res.-Biogeo., 116, https://doi.org/10.1029/2010JG001441, 2011.

Morse D. L., Waddington E. D., and Steig E. J.: Ice Age storm trajectories inferred from radar stratigraphy at Taylor Dome, Antarctica, Geophys. Res. Lett., 25, 3383–3386, 1998.

Obryk, M. K., Doran, P. T., Fountain, A. G., Myers, M., and McKay, C. P.: Climate From the McMurdo Dry Valleys, Antarctica, 1986–2017: Surface Air Temperature Trends and Redefined Summer Season, J. Geophys. Res.-Atmos., 125, https://doi.org/10.1029/2019JD032180, 2020.

Pendleton, S., Miller, G., Lifton, N., and Young, N.: Cryosphere response resolves conflicting evidence for the timing of peak Holocene warmth on Baffin Island, Arctic Canada, Quaternary Sci. Rev., 216, 107–115, 2019.

Petrenko, V. V., Smith, A. M., Brook, E. J., Lowe, D., Riedel, K., Brailsford, G., Hua, Q., Schaefer, H., Reeh, N., Weiss, R. F., Etheridge, D., and Severinghaus, J. P.: ^{14}CH$_4$ Measurements in Greenland Ice: Investigating Last Glacial Termination CH_4 Sources, Science, 324, 506–508, 2009.

Petrenko, V. V., Severinghaus, J. P., Smith, A. M., Riedel, K., Baggenstos, D., Harth, C., Orsi, A., Hua, Q., Franz, P., Takeshita, Y., Brailsford, G. W., Weiss, R. F., Buizert, C., Dickson, A., and Schaefer, H.: High-precision ^{14}C measurements demonstrate production of in situ cosmogenic ^{14}CH$_4$ and rapid loss of in situ

cosmogenic ^{14}CO in shallow Greenland firn, Earth. Planet. Sc. Lett., 365, 190–197, 2013.

Petrenko, V. V., Severinghaus, J. P., Schaefer, H., Smith, A. M., Kuhl, T., Baggenstos, D., Hua, Q., Brook, E. J., Rose, P., Kulin, R., Bauska, T., Harth, C., Buizert, C., Orsi, A., Emanuele, G., Lee, J. E., Brailsford, G., Keeling, R., and Weiss, R. F.: Measurements of ^{14}C in ancient ice from Taylor Glacier, Antarctica constrain in situ cosmogenic ^{14}CH$_4$ and ^{14}CO production rates, Geochim. Cosmochim. Ac., 177, 62–77, 2016.

Petrenko, V. V., Smith, A. M., Schaefer, H., Riedel, K., Brook, E., Baggenstos, D., Harth, C., Hua, Q., Buizert, C., Schilt, A., Fain, X., Mitchell, L., Bauska, T., Orsi, A., Weiss, R. F., and Severinghaus, J. P.: Minimal geological methane emissions during the Younger Dryas–Preboreal abrupt warming event, Nature, 548, 443–446, 2017.

Petrenko, V. V., Smith, A. M., Crosier, E. M., Kazemi, R., Place, P., Colton, A., Yang, B., Hua, Q., and Murray, L. T.: An improved method for atmospheric ^{14}CO measurements, Atmos. Meas. Tech., 14, 2055–2063, https://doi.org/10.5194/amt-14-2055-2021, 2021.

Prinn, R. G., Weiss, R. F., Krummel, P. B., O'Doherty, S., Fraser, P., Muhle, J., Reimann, S., Vollmer, M., Simmonds, P. G., and Malone, M.: The ALE/GAGE/AGAGE Network, Massachusetts Institute of Technology, Cambridge, MA (USA), https://doi.org/10.3334/CDIAC/atg.db1001, 2008.

Raynaud, D., Delmas, R., Ascencio, J. M., and Legrand, M.: Gas Extraction From Polar Ice Cores: A Critical Issue For Studying The Evolution of Atmospheric CO_2 and Ice-Sheet Surface Elevation, Ann. Glaciol., 3, 265–268, 1982.

Reimer, P. J., Austin, W. E., Bard, E., Bayliss, A., Blackwell, P. G., Ramsey, C. B., Butzin, M., Cheng, H., Edwards, R. L., and Friedrich, M.: The IntCal20 northern hemisphere radiocarbon age calibration curve (0–55 cal kBP), Radiocarbon, 62, 725–757, 2020.

Rhodes, R. H., Faïn, X., Stowasser, C., Blunier, T., Chappellaz, J., McConnell, J. R., Romanini, D., Mitchell, L. E., and Brook, E. J.: Continuous methane measurements from a late Holocene Greenland ice core: Atmospheric and in-situ signals, Earth. Planet. Sc. Lett., 368, 9–19, 2013.

Roessler, K., Jung, H.-J., and Nebeling, B.: Hot atoms in cosmic chemistry, Adv. Space Res., 4.12, 83–95, 1984.

Schilt, A., Brook, E. J., Bauska, T. K., Baggenstos, D., Fischer, H., Joos, F., Petrenko, V. V., Schaefer, H., Schmitt, J., Severinghaus, J. P., Spahni, R., and Stocker, T. F.: Isotopic constraints on marine and terrestrial N$_2$O emissions during the last deglaciation, Nature, 516, 234–237, 2014.

Schmitt, J., Schneider, R., and Fischer, H.: A sublimation technique for high-precision measurements of $\delta^{13}CO_2$ and mixing ratios of CO_2 and N$_2$O from air trapped in ice cores, Atmos. Meas. Tech., 4, 1445–1461, https://doi.org/10.5194/amt-4-1445-2011, 2011.

Shackleton, S., Baggenstos, D., Menking, J. A., Dyonisius, M. N., Bereiter, B., Bauska, T. K., Rhodes, R. H., Brook, E. J., Petrenko, V. V., McConnell, J. R., Kellerhals, T., Häberli, M., Schmitt, J., Fischer, H., and Severinghaus, J. P.: Global ocean heat content in the Last Interglacial, Nat. Geosci., 13, 77–81, 2020.

Siegenthaler, U., Stocker, T. F., Monnin, E., Lüthi, D., Schwander, J., Stauffer, B., Raynaud, D., Barnola, J.-M., Fischer, H., and Masson-Delmotte, V.: Stable carbon cycle–climate relationship during the late Pleistocene, Science, 310, 1313–1317, 2005.

Sinisalo, A., Moore, J. C., Wal, R. S. W. V. D., Bintanja, R., and Jonsson, S.: A 14 year mass-balance record of a blue-ice area in Antarctica, Ann. Glaciol., 37, 213–218, 2003.

Skov, D. S., Egholm, D. L., Jansen, J. D., Sandiford, M., and Knudsen, M. F.: Detecting landscape transience with in situ cosmogenic ^{14}C and ^{10}Be, Quat. Geochronol., 54, 101008, https://doi.org/10.1016/j.quageo.2019.101008, 2019.

Smith, A. M., Levchenko, V. A., Etheridge, D. M., Lowe, D. C., Hua, Q., Trudinger, C. M., Zoppi, U., and Elcheikh, A.: In search of in-situ radiocarbon in Law Dome ice and firn, Nucl. Instrum. Meth. B, 172, 610–622, 2000.

Smith, A. M., Hua, Q., Williams, A., Levchenko, V., and Yang, B.: Developments in micro-sample ^{14}C AMS at the ANTARES AMS facility, Nucl. Instrum. Meth. B, 268, 919–923, 2010.

Sowers, T., Bender, M., Raynaud, D., and Korotkevich, Y. S.: δ^{15}N of N_2 in air trapped in polar ice: A tracer of gas transport in the firn and a possible constraint on ice age-gas age differences, J. Geophys. Res., 97, 15683–15697, 1992.

Spector, P., Stone, J., and Goehring, B.: Thickness of the divide and flank of the West Antarctic Ice Sheet through the last deglaciation, The Cryosphere, 13, 3061–3075, https://doi.org/10.5194/tc-13-3061-2019, 2019.

Steig, E. J., Morse, D. L., Waddington, E. D., Stuiver, M., Grootes, P. M., Mayewski, P. A., Twickler, M. S., and Whitlow, S. I.: Wisconsinan and Holocene Climate History from an Ice Core at Taylor Dome, Western Ross Embayment, Antarctica, Geogr. Ann. A., 82, 213–235, 2000.

van De Wal, R. S. W., Van Roijen, J. J., Raynaud, D., Van der Borg, K., De Jong, A. F. M., Oerlemans, J., Lipenkov, V., and Huybrechts, P.: From ^{14}C/12C measurements towards radiocarbon dating of ice, Tellus B, 46, 94–102, 1994.

van De Wal, R. S. W., Meijer, H. A. J., De Rooij, M., and Van der Veen, C.: Radiocarbon analyses along the EDML ice core in Antarctica, Tellus B, 59, 157–165, 2007.

Van der Kemp, W. J. M., Alderliesten, C., Van der Borg, K., Holmlund, P., de Jong, A. F. M., Karlöf, L., Lamers, R. A. N., Oerlemans, J., Thomassen, M., and Van de Wal, R. S. W.: Very little in situ produced radiocarbon retained in accumulating Antarctic ice, Nucl. Instrum. Meth. B, 172, 632–636, 2000.

Van der Kemp, W. J. M., Alderliesten, C., Van der Borg, K., De Jong, A. F. M., Lamers, R. A. N., Oerlemans, J., Thomassen, M., and Van De Wal, R. S. W.: In situ produced ^{14}C by cosmic ray muons in ablating Antarctic ice, Tellus B, 54, 186–192, 2002.

van Roijen, J. J., Bintanja, R., Van der Borg, K., van den Broeke, M. R., de Jong, A. F. M., and Oerlemans, J.: Dry extraction of $^{14}CO_2$ and ^{14}CO from Antarctic ice, Nuclear Instruments and Methods in Physics Research Section B: Beam Interactions with Materials and Atoms, Nucl. Instrum. Meth. B, 92, 331–334, 1994.

Vimont, I.: Carbon Monoxide Stable Isotopes: Extraction Technique Development and Urban Atmospheric Analysis, PhD Thesis, University of Colorado Boulder, https://www.proquest.com/docview/1985027740?pq-origsite=gscholar&fromopenview=true (last access: 27 January 2023), 2017.

Wilson, A. T. and Donahue, D. J.: The recovery and dating of carbon dioxide in polar ice cores, Radiocarbon, 31, 579–584, 1989.

Wilson, A. T. and Donahue, D. J.: AMS carbon-14 dating of ice: progress and future prospects, Nucl. Instrum. Meth. B, 52, 473–476, https://doi.org/10.1016/0168-583X(90)90460-C, 1990.

Wilson, A. T. and Long, A.: New approaches to CO_2 analysis in polar ice cores, J. Geophys. Res.-Oceans, 102, 26601–26606, 1997.

Yang, B. and Smith, A. M.: Conventionally Heated Microfurnace for the Graphitization of Microgram-Sized Carbon Samples, Radiocarbon, 59, 859–873, 2017.

Zumbrunn, R., Neftel, A., and Oeschger, H.: CO_2 measurements on 1-cm3 ice samples with an IR laserspectrometer (IRLS) combined with a new dry extraction device, Earth. Planet. Sc. Lett., 60, 318–324, 1982.

The Cryosphere

Open Access

EGU

Supplement of

Using ice core measurements from Taylor Glacier, Antarctica, to calibrate in situ cosmogenic ^{14}C production rates by muons

Michael N. Dyonisius et al.

Correspondence to: Michael N. Dyonisius (michael.dyonisius@nbi.ku.dk)

SUPPLEMENTARY MATERIALS

S1. Detailed data reduction and corrections for $^{14}CO_2$ sublimation samples

S1.1. Empirical correction for ANSTO processing

To correct for the effects of graphitization and other processing at ANSTO, we first used a linear empirical correction from commensurately-sized ^{14}C standards (Table S7, Fig. S1). The empirically corrected $^{14}CO_2$ values for the BFI and ice samples are shown in Tables S8-S10.

S1.2. Extraneous carbon added from the sublimation procedure

At the end of each sublimation, we calculated the C mass (M_g, mass before graphitization) of the sample by expanding the cryogenically-trapped CO_2 into a calibrated manometer volume. Assuming the $[CO_2]$ measurement in the subsample from OSU (Table S9) is representative of the larger sublimation sample, the expected C mass (M_s, "true" mass of the sample) can be calculated from the amount of air trapped in the molecular sieve. Based on the elevation of the measured C mass (M_g) over the expected C mass (M_s), we calculated that the extraneous C (M_{ext}) introduced by the sublimation system is non-negligible (0.37 ± 0.38 µgC, 2σ, n = 23, Table S9).

We used the laboratory-produced BFI samples to calculate the ^{14}C activity ($^{14}C_{ext}$) of this extraneous C (with mass M_{ext}) added from sample preparation, handling, and sublimation using the following mass balance equations:

$$M_g \cdot {}^{14}C_g = M_s \cdot {}^{14}C_s + M_{ext} \cdot {}^{14}C_{ext} \qquad \text{Eq.S1}$$

$$M_g = M_s + M_{ext} \qquad \text{Eq.S2}$$

where $^{14}C_g$ is the measured ^{14}C activity after the empirical correction for ANSTO processing (Table S8) and $^{14}C_s$ is the true ^{14}C activity of the CO_2 in the ice sample (corrected for the extraneous C addition from the sublimation system). All ^{14}C terms in Eq. S1 and Eq. S2 are in percent modern carbon (pMC) units, which have been shown to be mass-additive (Petrenko et al., 2008).

For the BFI samples, the "true" ^{14}C activity ($^{14}C_s$) is the $^{14}CO_2$ activity of the standard gas. The expected C mass (M_s) for the BFI samples was calculated from the amount of air trapped in the molecular sieve and the [CO_2] of the standard gas. Using Eq. S1 and Eq. S2, we can solve for $^{14}C_{ext}$ for each laboratory-produced BFI sample. All relevant mass balance variables (M_g, M_s, M_{ext}, $^{14}C_g$, $^{14}C_s$, and $^{14}C_{ext}$) from the laboratory-produced BFI samples are shown in Table S8.

The error-propagated uncertainty of the extraneous carbon ^{14}C activity ($^{14}C_{ext}$) inferred from individual BFI measurements was large, especially in samples that used the modern standard gas because the measured ^{14}C activities of the BFI samples ($^{14}C_g$) were indistinguishable from the "true" ^{14}C activity of the standard gas ($^{14}C_s$). In comparison, for BFI samples that used the ^{14}C-dead standard gas, the measured ^{14}C activities of the blanks were elevated by ~3 pMC compared to the "true" ^{14}C activity of the standard gas (Table S8). This strongly suggests that the main source of the extraneous carbon to the sublimation device is likely CO_2 from ambient air, which has a "modern" ^{14}C signature.

On average, we calculated that $^{14}C_{ext} = 125.9$ pMC; the standard deviation of $^{14}C_{ext}$ is ± 47.1 pMC (1σ), and the standard error of the mean of $^{14}C_{ext}$ is ± 15.7 pMC. We used twice the standard error of the mean (± 31.4 pMC) from all 9 laboratory BFI samples as the 2σ uncertainty for $^{14}C_{ext}$ and solved for $^{14}C_s$ in each sample using Eq. S1 (Table S9), assuming the amount of extraneous carbon and its ^{14}C activity from the BFI measurements were representative of the extraneous carbon that was introduced to the samples. This correction represents the biggest source of uncertainty for the $^{14}CO_2$ measurements. Finally, we used TAC from OSU subsamples (Table S9) to convert between $^{14}CO_2$ molecules per cc STP and $^{14}CO_2$ molecules per g ice (Petrenko et al., 2016 Electronic Annex S1).

S1.3. Corrections for post-coring in situ ^{14}C

After correcting for the extraneous C added from the sublimation process, the sample ^{14}C values were further corrected for post-coring *in situ* $^{14}CO_2$ production (i.e., $^{14}CO_2$ produced by cosmic rays during storage and transport after the ice samples were brought up to the surface). The post-coring production was constrained by comparing the $^{14}CO_2$ content in field-produced BFI against laboratory-produced BFI (which did not contain the

2

additional post-coring $^{14}CO_2$, Table S10). We used the ratio of air from the standard gas collected at the end of the sublimation to the mass of BFI that was sublimated as our BFI "air content." We then used this "air content" of the BFI samples and the [CO_2] measured from the manometers to convert the $^{14}CO_2$ measured in the BFI samples into $^{14}CO_2$ molecules per gram of bubble free ice (Table S10). From 4 laboratory-produced BFI samples that used ^{14}C-dead standard gas and 5 field produced BFI samples that used the same standard gas, we calculated that the post-coring ^{14}C production added 8.2 ± 5.9 $^{14}CO_2$ molecules g^{-1} ice (1σ) to the samples (Table S10). The sample $^{14}CO_2$ content after all corrections and the associated propagated uncertainties is shown in Table S9.

S1.4. $^{14}CO_2$ analytical uncertainty and acceptance criteria for Monte Carlo method to estimate model parameter uncertainties

The uncertainty of the $^{14}CO_2$ measurements is critical to the interpretation of the data, as it is the largest source of uncertainty for total ^{14}C. The uncertainties of our $^{14}CO_2$ measurements from step-by-step error propagation (Table S8, on average ±31.6 $^{14}CO_2$ molecules/g ice, 95% CI) are comparable to the uncertainty reported in prior studies that used a dry extraction method (van De Wal et al., 2007; van Der Kemp et al., 2002, ~21 $^{14}CO_2$ molecules/g ice). The agreement between replicate samples is, however, much better than what would be expected from the error-propagated uncertainties in individual measurements (Table 1, Table S8). We calculated the pooled standard deviation of replicate pair measurements (s_p) for the $^{14}CO_2$ samples following McNaught and Wilkinson (1997)

$$s_p = \sqrt{\frac{\sum (x_{i1} - x_{i2})^2}{2k}} \qquad \text{Eq.S3}$$

where x_{i1} and x_{i2} refer to measurement #1 and measurement #2 from depth interval i and k refers to the number of replicate pairs. The uncertainty derived from pooled standard deviation of replicate pair measurements (±12.4 $^{14}CO_2$ molecules/g ice, 2σ) is notably lower than the error-propagated uncertainties (±31.6 $^{14}CO_2$ molecules/g ice on average, 95% CI). The pooled standard deviation is even lower (±7.8 $^{14}CO_2$ molecules/g ice, 2σ) if

we exclude the replicate pair from 2.25 m depth. The shallow (< 6m) ice in Taylor Glacier has been shown to contain ambient air contamination from near-surface thermal contraction cracks (Baggenstos et al., 2017; Petrenko et al., 2016). These thermal cracks are not homogenous, can heal, and become invisible to the naked eye. Despite being collected from the same depth, the two 2.25 m samples might contain different amounts of ambient air.

Both methods of determining analytical uncertainties (error-propagation vs. pooled standard deviation from replicates) are in principle valid. For the $^{14}CH_4$ and ^{14}CO measurements, we used the error propagation method because we do not have replicates. When replicate measurements are available, it is common practice in ice core analysis to use the pooled standard deviation (e.g., Mitchell et al., 2013). Based on the observation that the ratios of $^{14}CO_2$ to other ^{14}C species (Fig. S4B, Section 4.2) are relatively constant, it is likely that the error propagation method overestimates the uncertainty of our $^{14}CO_2$ measurements.

However, when we use the smaller uncertainty from the pooled standard deviation, the ice flow/^{14}C production model was not able to produce a total ^{14}C profile that can fit all measurements within their 95% CI uncertainties (Fig. 6b). The best-fit ^{14}C profile from the model fell outside the 95% CI uncertainties of total ^{14}C from two depth ranges (10 m and 72 m samples). The samples from these two depth ranges show excellent agreement among their replicates (Table 1, Fig. 6b); there were also no analytical issues that would call these values into question. If the analytical uncertainty of the $^{14}CO_2$ data is truly ±31.6 $^{14}CO_2$ molecules/g ice (95% CI), it is very unlikely that the combined data (^{14}CO, $^{14}CO_2$, and $^{14}CH_4$) can produce the observed $^{14}CO_2$/total ^{14}C ratio of 0.66 ± 0.12 (95% CI, Table 1, Fig. S4B).

One possible explanation for the model-data mismatch at 10 m and 72 m depth ranges is that because of their smaller sample size, the $^{14}CO_2$ samples might be more susceptible to small-scale variations in ice flow that are not captured by the 2D ice-flow model. For example, heterogeneity in ice rheology may play a role. Our samples (from 0 to 72m depth) span a large range of ages (50-92 kyr BP), over several Dansgaard-Oeschger events and

Marine Isotope Stages. As such, they have significantly different impurity content and ice with higher chemical impurities deforms more easily (Stoll et al., 2021). Marine Isotope Stage 4 (MIS4) ice (~55-72 kyr BP), which is characterized by high dust content (Menking et al., 2019) was missing entirely in the cores we drilled (Section 3 of Supplementary Materials). MIS4 ice was also missing from the Taylor Glacier across-flow transect (Baggenstos et al., 2017) but it does outcrop several hundred meters downglacier (Menking et al., 2019; Shackleton et al., 2021). This shows that there is preferential deformation of dusty ice in Taylor Glacier (which might account for why $^{14}CO_2$ values from certain depth ranges show excellent agreement among replicates but are off from the model-predicted ^{14}C) that is not accounted for by the 2D flow model.

Alternatively, it is also possible that the real analytical uncertainty of the $^{14}CO_2$ measurements might be somewhere between the uncertainties estimated via the error-propagation and pooled standard deviation methods. There can be additional sources of uncertainties that are not captured by pooled standard deviation among replicates. For example, processes such as gas loss (especially for the deeper samples) can affect both replicate samples equally and bias the signal. Furthermore, as we are working with a relatively small dataset, the pooled standard deviation among the 9 pairs of replicate measurements might underestimate the analytical uncertainty of the system. More measurements of ice with known exposure history, age, and more sample replicates are needed to better constrain the overall analytical uncertainty of the sublimation system for $^{14}CO_2$ measurements. However, there are also sources of uncertainties in the sublimation system that do not contribute to the overall variability (and thus precision) the analytical measurements. For example, the determination of air content and $[CO_2]$ of the sublimation samples are based on pressure readings with volume-calibrated manometers. Both the pressure gauge readings and the manometer volumes have uncertainties that are propagated through the overall uncertainties with the step-by-step error propagation method. However, the manometer volumes do not change from sample to sample, and thus this kind of uncertainties do not contribute to measurement variability and not accounted by the pooled standard deviation of replicates (which is ultimately a measure of analytical precision).

We argue that the uncertainty derived from pooled standard deviation method is more appropriate to use for our case. We used the pooled standard deviation ($\pm$7.8 $^{14}CO_2$ molecules/g ice, 2σ) as the uncertainty for all $^{14}CO_2$ measurements except the 2.25m sample pair, which are affected by modern air contamination from surface cracks (where we used the error-propagated uncertainties instead, Table 1). However, considering that the model was not able to fit all the data at 95% CI uncertainty even with the best-estimate model parameters (σ_0, f_{tot}, and flow trajectories), it is not surprising that the Monte Carlo simulations also struggle to find a pair of σ_0 and f_{tot} that can fit all measurements within their 95% CI. An alternative acceptance criteria to estimate the uncertainties of the ^{14}C production model parameters is needed. In the Monte Carlo method, we accept all model parameters (σ_0 and f_{tot}) that produce model-calculated, total ^{14}C within the 95% CI and 68% CI measurement uncertainties of the total ^{14}C from the best-fit parameter values (Fig. 6, Fig, 7). This approach essentially cancels out the representation error from the ice flow/^{14}C production model and provides uncertainty estimates for σ_0 and f_{tot} that are based solely on the prescribed analytical uncertainties.

S2. Subsample [CH_4] measurements and sample integrity of the large volume samples

The [CH_4] measurements from continuous flow analysis (CFA) on TG-Deep3 core (borehole #3) and the [CH_4] from the large volume samples (which combine ice from all three boreholes) are shown in Fig. S11. The continuous [CH_4] measurements show high variability near the ice surface. The near-surface elevation in [CH_4] is likely because of contamination from modern air due to thermal cracks (Baggenstos et al., 2017; Petrenko et al., 2016) and the depletion is likely due to consumption of CH_4 by methanotrophic microbes. The $\delta^{13}CH_4$ value of Taylor Glacier surface sample is ~10‰ higher relative to typical atmospheric $\delta^{13}CH_4$ values of -47‰ (Table S1), indicating likely biological fractionation during methane consumption. Alterations of trace gases in the shallowest ice at margin sites are common and not unique to Taylor Glacier (Petrenko et al., 2006; Turney et al., 2013). The ^{14}CO and $^{14}CH_4$ measurements from the "surface" sample are thus also rejected.

Another stand-out feature in the CFA data is the low [CH_4] values between ~24-27 m depth (Fig. S11). Discrete [CH_4] measurements from the gas chromatography (GC) system (Mitchell et al., 2011) were conducted to rule out the possibility of instrument error from the CFA system. The discrete measurements confirmed the validity of the CFA measurements and furthermore showed unusual reduction in total air content (TAC) of the ice in this low-[CH_4] section. The [CH_4] values observed in this section (200-300 nmol/mol) are lower than the lowest observed atmospheric [CH_4] over the past 800 kyr (Loulergue et al., 2008), and thus the possibility that the low CH_4 section represents an ice section from another time period can be ruled out. In this core section we do not have strong evidence for microbial consumption; unlike the surface samples, the $\delta^{13}CH_4$ values in the large volume samples adjacent to this section (19.5m and 30m) are within the range of glacial-interglacial variability (Table S1). Additional measurements of $\delta^{13}CO_2$ and $\delta^{13}CH_4$ would be useful to investigate the microbial consumption hypothesis. The ^{14}CO and $^{14}CH_4$ in the 19.5m large volume sample from 2015/16 were rejected because the samples partially contained ice from this section.

The [CH_4] from the "30m" large volume sample is also strongly elevated relative to the CFA measurements. This sample also contains unusually elevated CO (Table S5) and highly chlorinated compounds measured by the SIO GC-MS system (not shown). However, this contamination is likely unrelated to the anomalous [CH_4] depletion observed by the CFA measurements around this region. Instead, during the on-field processing of this sample at Taylor Glacier, we encountered a problem with the electric bandsaw that was usually used to cut the CFA "stick" subsamples (Fig. S1). The CFA "sticks" for the 30m sample were instead cut with an electric chainsaw (which was significantly dirtier than the electric bandsaw). Thus, the anomalous elevation of [CH_4] on the 30m sample was likely due to contamination from the electric chainsaw. Because of this contamination, the 30m sample results are rejected.

The 40.5m, 51m, and 61.5m large-volume samples also show slightly elevated [CH_4] relative to the CFA measurements, although not to the extent of the 30m sample (Fig. S11). Unlike the 30m sample, the 40.5m, 51m, and 61.5m sample do not contain anomalously

high CO or chlorinated compounds. For these samples, the discrepancy between the $[CH_4]$ measurement from the bulk large volume sample and CFA subsamples is likely be due to slight age offsets between the boreholes (only borehole #3 was subsampled and measured with CFA system).

S3. Sample age determination and integrity of $^{14}CO_2$ samples

The age-scale for the samples used in this study was established via matching the measured CFA $[CH_4]$ from the continuous subsample sticks onto other ice core records with well-established chronologies. The continuous $[CH_4]$ from TG-Deep3 was matched to the continuous $[CH_4]$ from the NEEM (North Greenland EEMian Ice Drilling) ice core (Chappellaz et al., 2013) using manually picked tie points. From the CH_4 synchronization, it is clear that the samples used in this study are all older than 55 ka (Fig. S12). Thus, we do not expect any ^{14}C inheritance from the accumulation site.

We also compared the measured $[CO_2]$ in our samples to $[CO_2]$ from other Antarctic ice cores (Bereiter et al., 2015) to confirm the integrity of the $^{14}CO_2$ samples. However, for a direct comparison with existing CO_2 records, we have to transfer the TG-Deep3 / NEEM gas age scale onto the AICC12 (Antarctic Ice Core Chronology) age scale (Veres et al., 2013). Currently the NEEM gas age is not included in AICC12. However, in the GICC05 (Greenland Ice Core Chronology) framework (Rasmussen et al., 2006; Rasmussen et al., 2013) the NEEM ice age is synchronized with NGRIP ice age (North Greenland Ice Core Project). NGRIP ice and gas age were included in AICC12 (Veres et al., 2013). This allows us to transfer our TG-Deep3/NEEM gas age onto AICC12 gas age by first interpolating the TG-Deep3(NEEM) gas age onto NEEM & NGRIP ice age and then onto NGRIP/AICC12 gas age.

The $[CO_2]$ measurements from our samples agree well with $[CO_2]$ from EDML ice core, except for the "30m" sample (~72 ka) which has a significantly lower $[CO_2]$ than the Antarctic ice core composite (Fig. S12). As discussed above, at this depth the $[CH_4]$ is also anomalously depleted (Fig. S11), and the [CO] in the large volume sample is anomalously

elevated (Table S5). This depth range is also associated with a large age discontinuity (Fig. S11). The "30m" $^{14}CO_2$ sample was thus rejected.
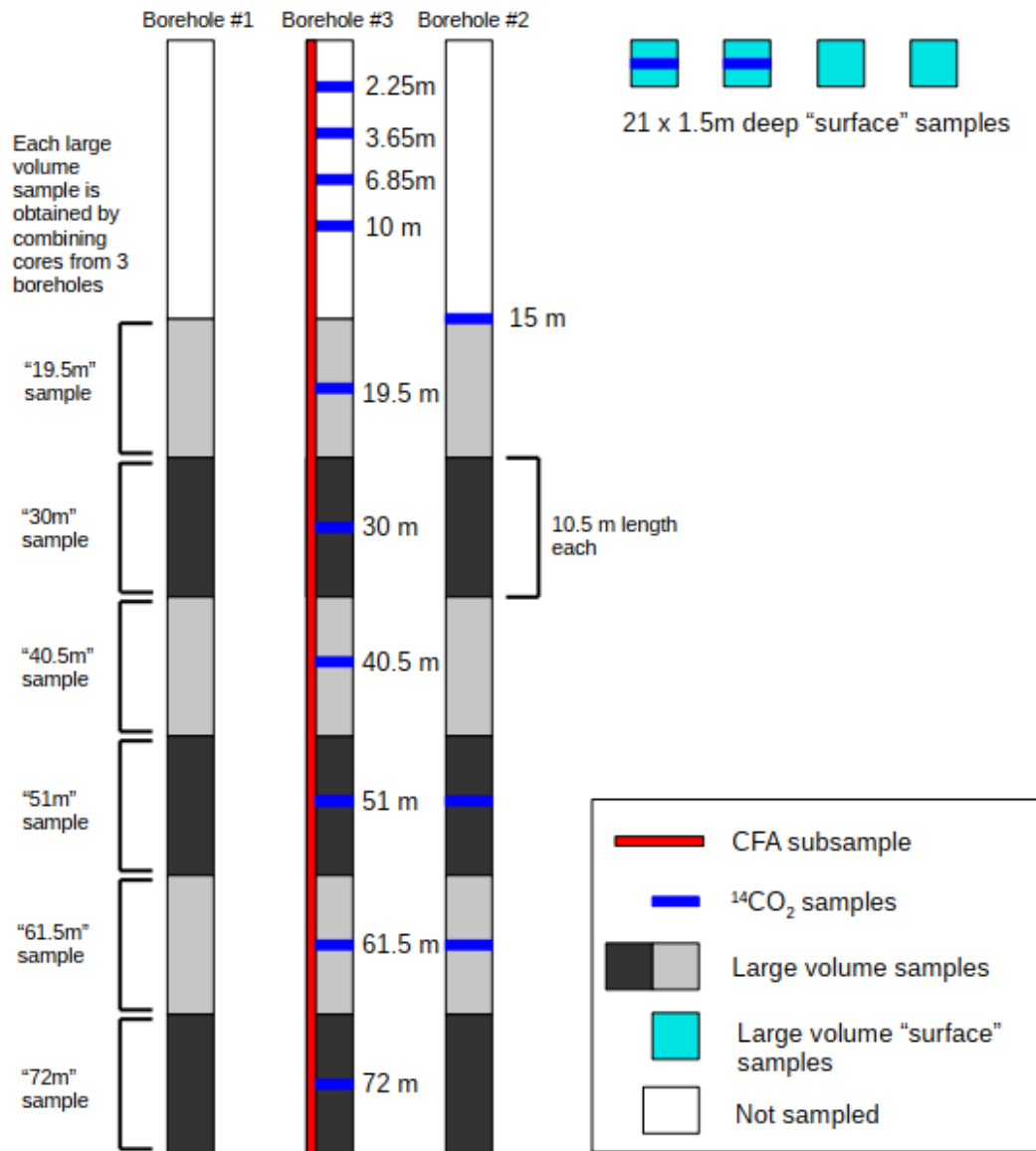
Fig. S1. Sampling scheme for the Taylor Glacier 2015/2016 field season ^{14}C samples. Each large-volume sample for $^{14}CH_4$ and ^{14}CO measurements requires ~1000kg of ice. For the deep samples (>19.5 m, shown in light and dark grey), this is achieved by combining same depth samples from 3 Blue Ice Drill (BID) boreholes, 10.5 m in length from each borehole. For the "surface" large-volume sample (shown in light blue), we combined 21 surface BID ice cores, 1.5 m length each into one large-volume sample. 3x3 cm CFA "stick" subsamples (shown in red) were cut from the whole length of borehole #3 for age control. 2-3 kg discrete samples for $^{14}CO_2$ measurements (shown in dark blue) were taken from the large-volume mid-depths of borehole #3 and borehole #2. Additional discrete $^{14}CO_2$ samples were taken from the mid-depths of Petrenko et al. (2016) large-volume samples (2.25-15 m) to complement their ^{14}CO and $^{14}CH_4$ measurements.
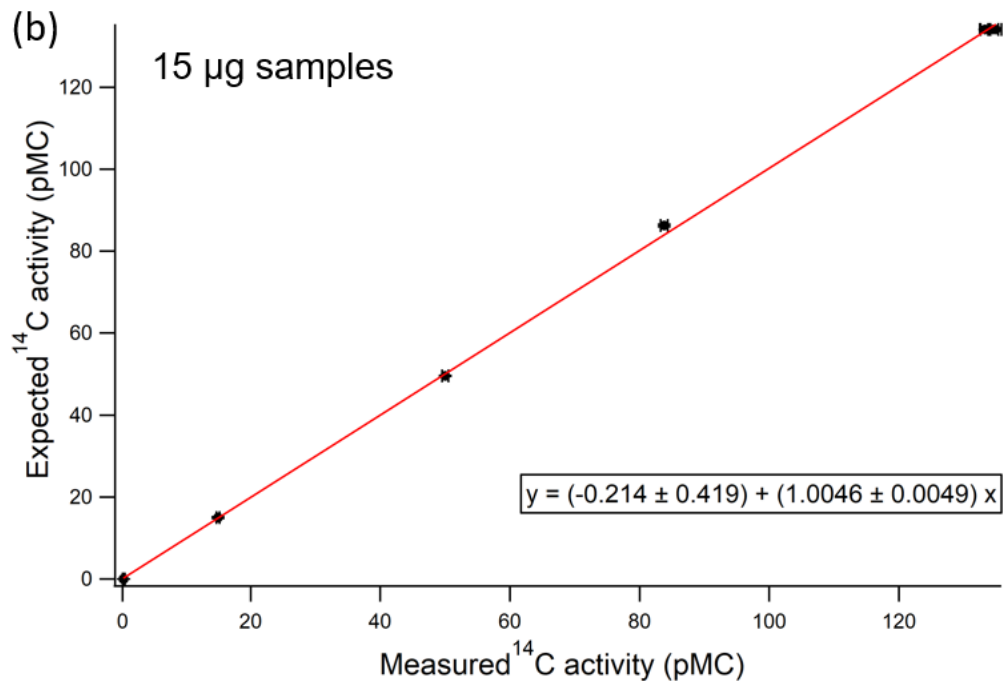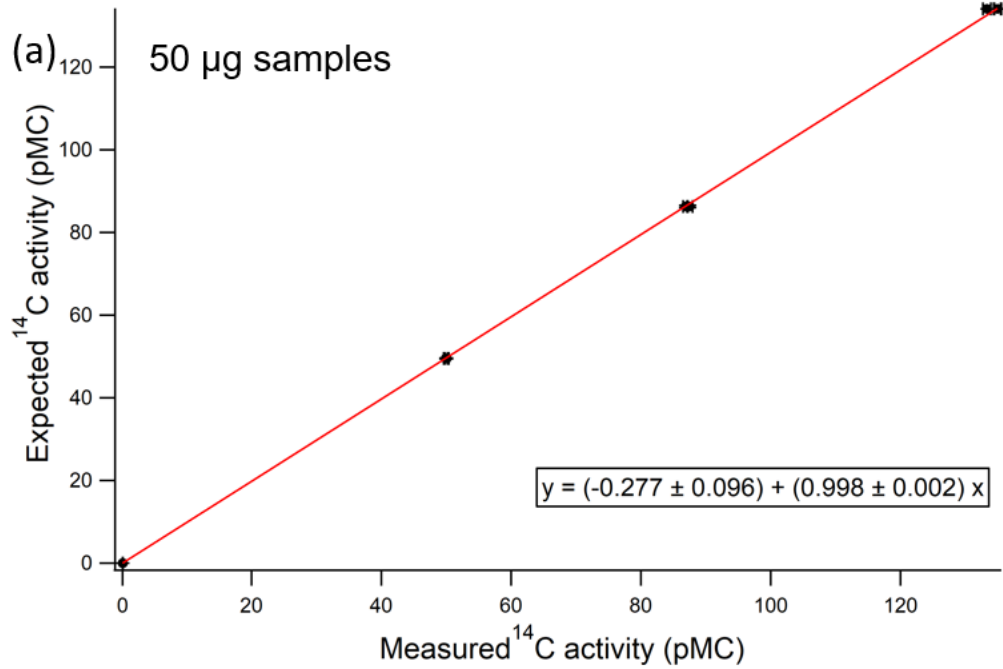
Fig. S2. Linear empirical correction from commensurately-sized ^{14}C standards for the (a) ^{14}CO samples and (b) $^{14}CO_2$ samples. The errors on the coefficients represent 68% CI (1σ). The measured and expected ^{14}C activities of these standards are shown in Table S7.
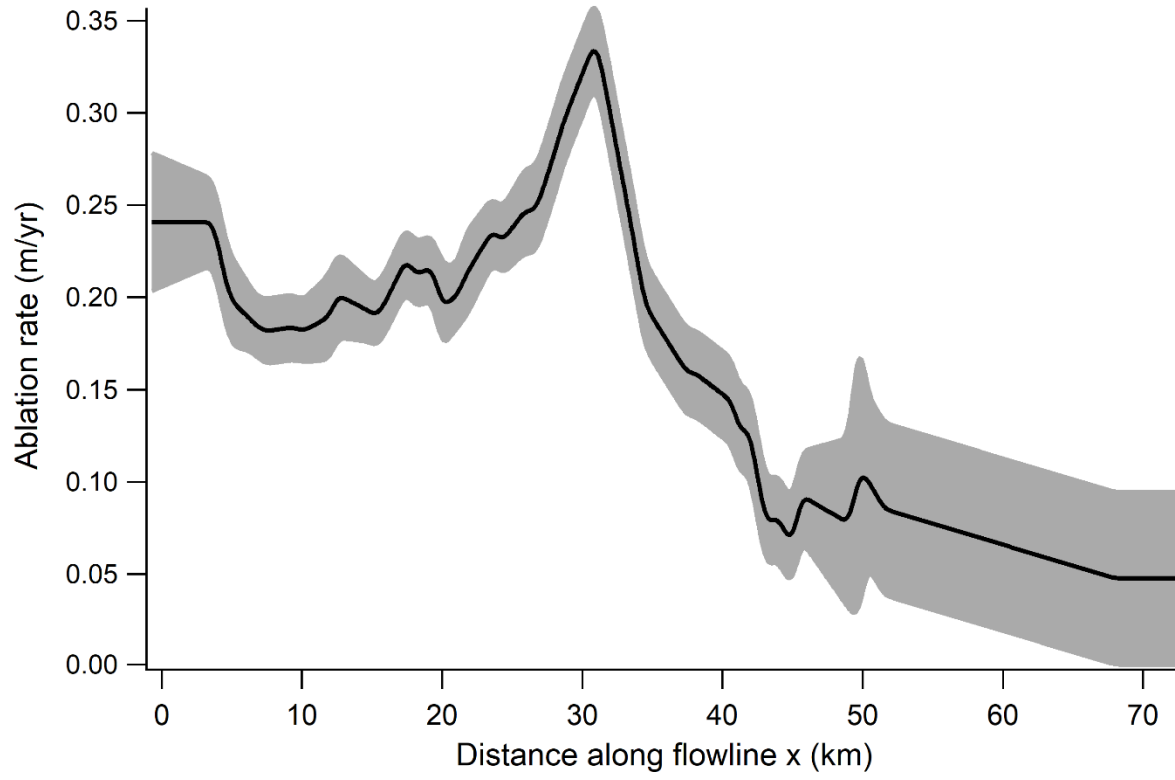
Fig. S3. Ablation rates along the glacier inferred from survey pole data. The shaded region represents 2σ uncertainties.

Fig. S4. (A). Goodness of the fit (χ^2) for the coarse grid-search under best-estimate ablation rate scenario to find best-estima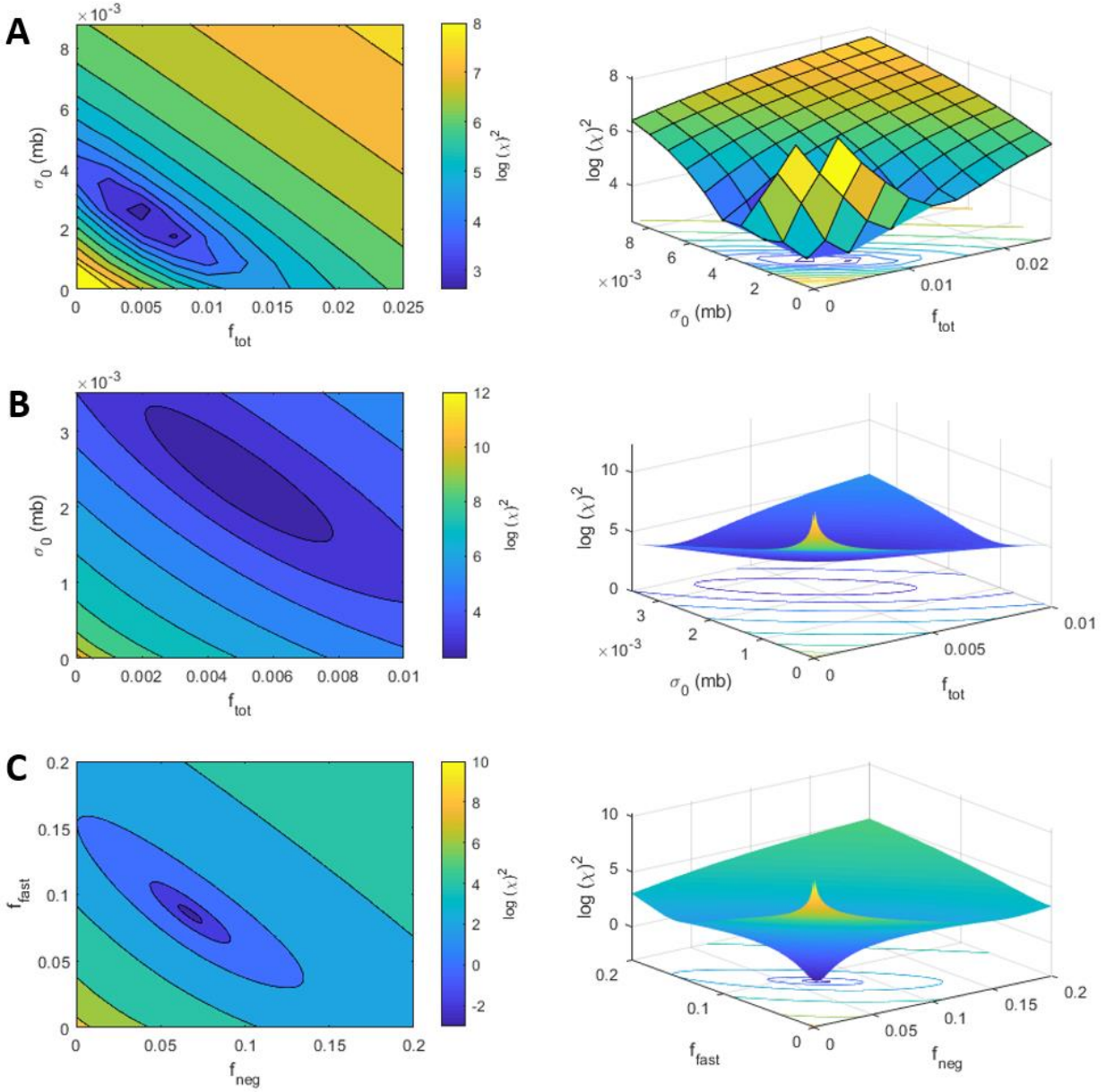te f_{tot} and σ_0. (B). Goodness of the fit (χ^2) for the high-resolution grid-search under best-estimate ablation rate scenario to find best-estimate f_{tot} and σ_0. (C). Goodness of the fit (χ^2) under best-estimate ablation rate scenario to find best-estimate f_{neg} and f_{fast} for ^{14}CO-specific muogenic production rates
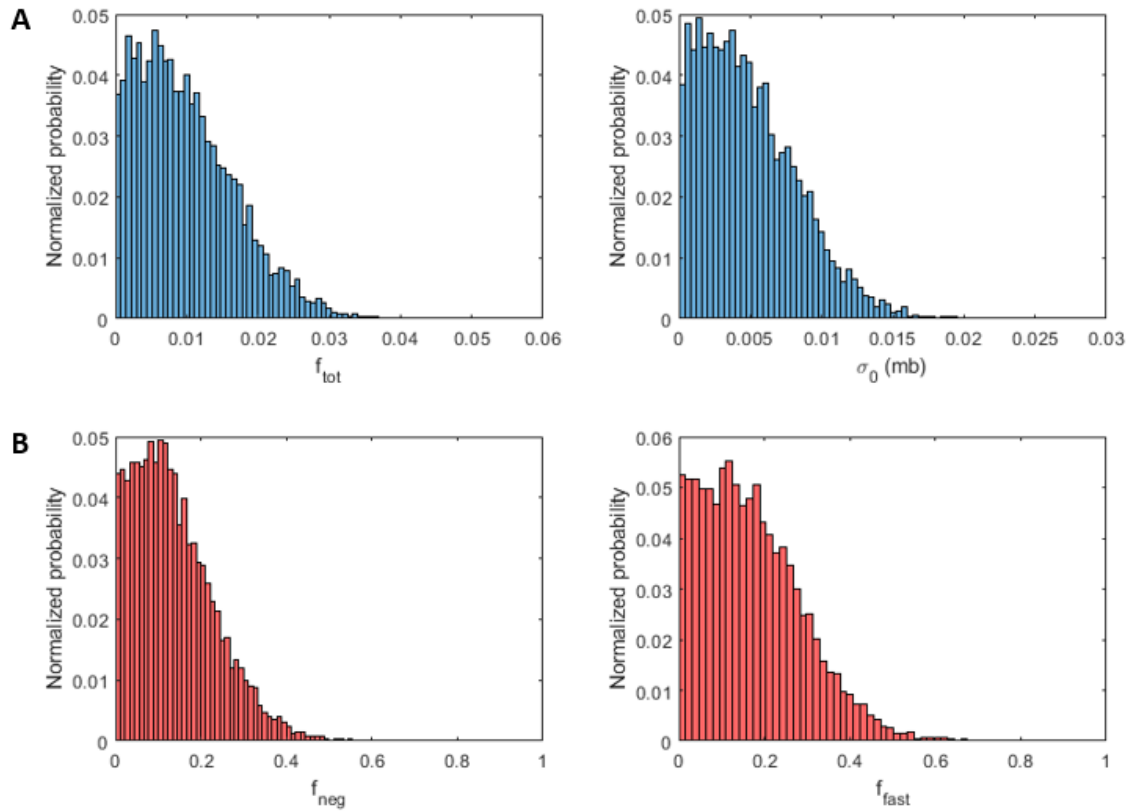
Fig. S5. (A). Prior distribution of model parameters f_{tot} and σ_0 for total ^{14}C production used in the Monte-Carlo simulations to estimate total muogenic ^{14}C production rates. (B). Prior distribution of model parameters f_{neg} and f_{fast} used in the Monte-Carlo simulations to estimate [14]CO-specific muogenic production rates.
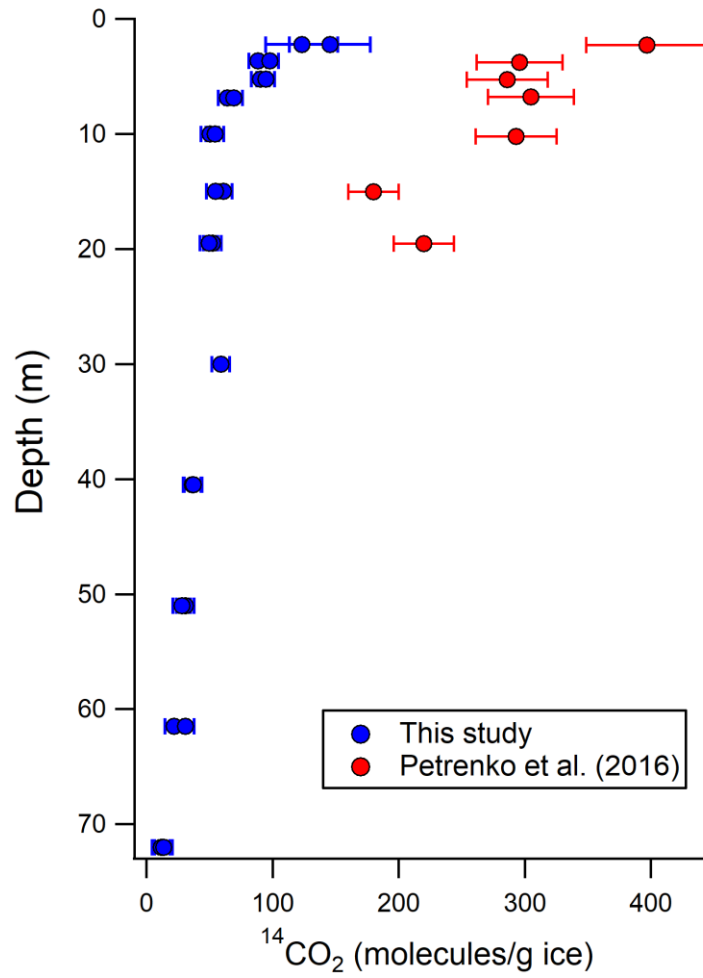
Fig. S6. Comparison between sublimation-based $^{14}CO_2$ measurements (this study) and melt-extraction based $^{14}CO_2$ measurements from Petrenko et al. (2016). Both dataset are obtained from the same site (Taylor Glacier, Antarctica).
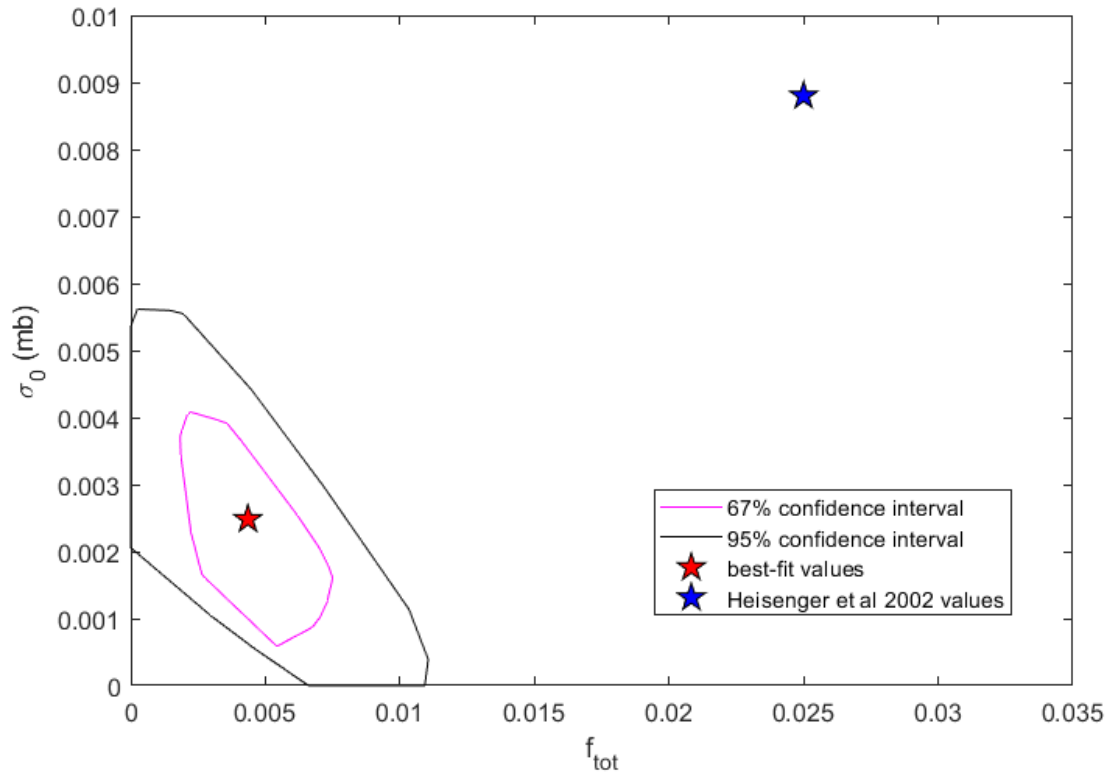
Fig.S7. 68% and 95% CI contours of accepted σ_0 and f_{tot} values for total ^{14}C when the ±31.6 ^{14}CO$_2$ molecules/g ice, 95% CI uncertainty from step-by-step error propagation method was used for the ^{14}CO$_2$ data as the Monte Carlo acceptance criteria. Even when using the larger and likely overestimated ^{14}CO$_2$ uncertainty, our data still clearly show what the Heisinger et al. (2002a, 2002b) values are overestimated.
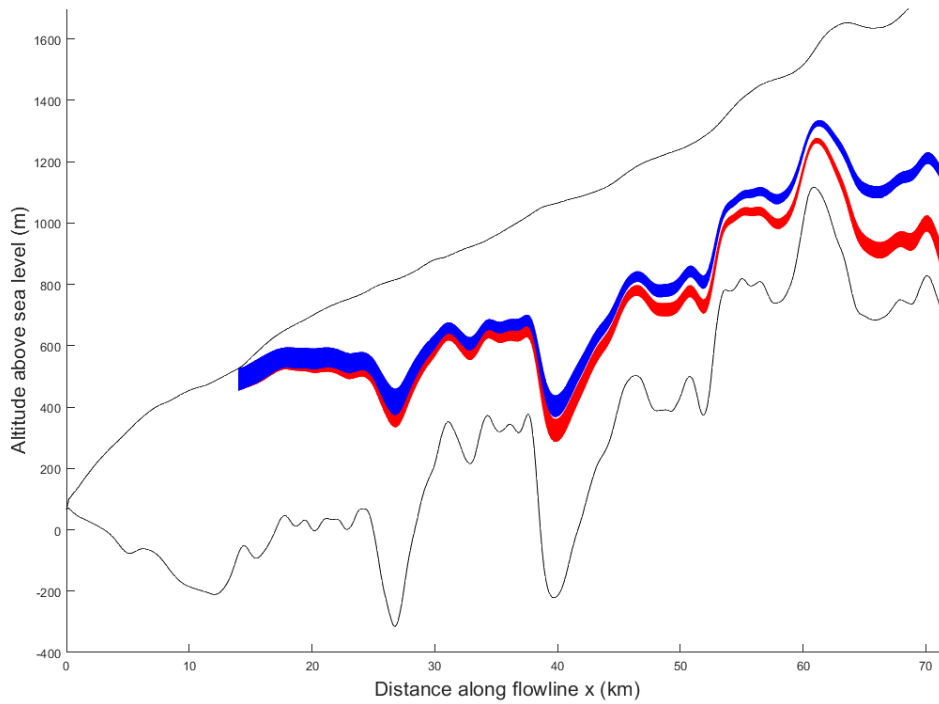
Fig. S8. Ice parcel trajectories under best-estimate ablation rate (blue) and +2.4σ high ablation rate (red) used in sensitivity analysis
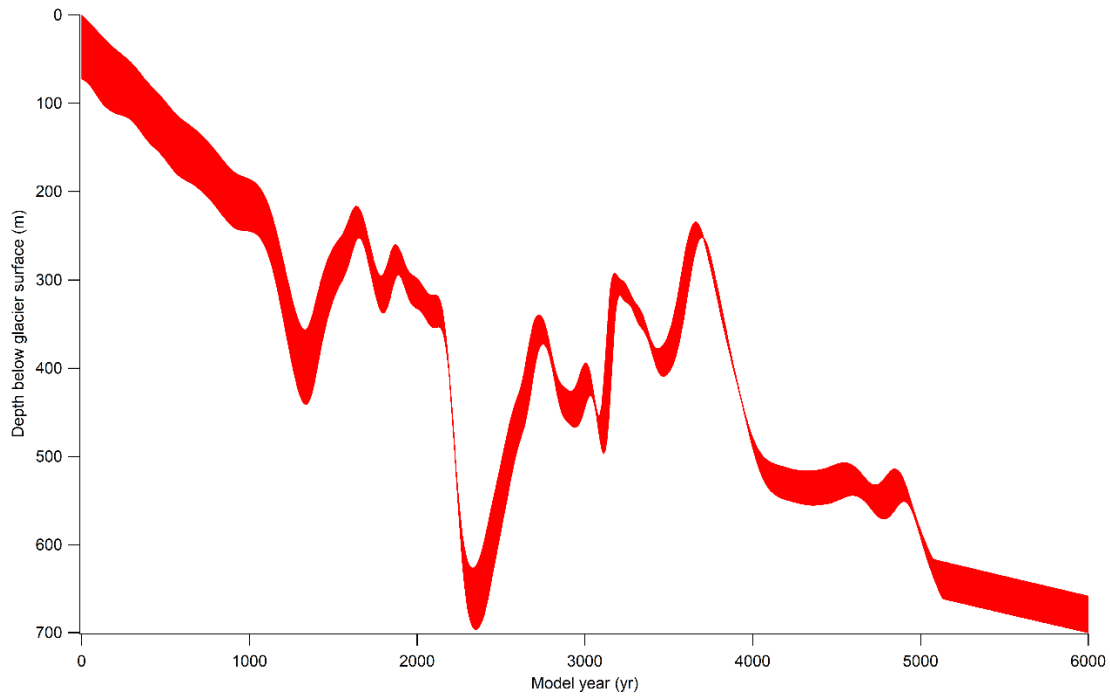
Fig. S9. Trajectories of our ice samples as function of model year.
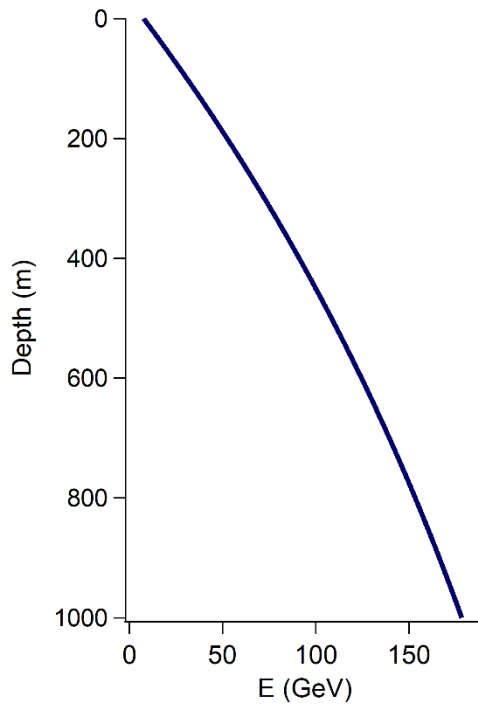
Fig. S10. Calculated mean muon energy (Ē) versus depth at Taylor Glacier from Balco et al. (2008) cosmogenic nuclide production model.
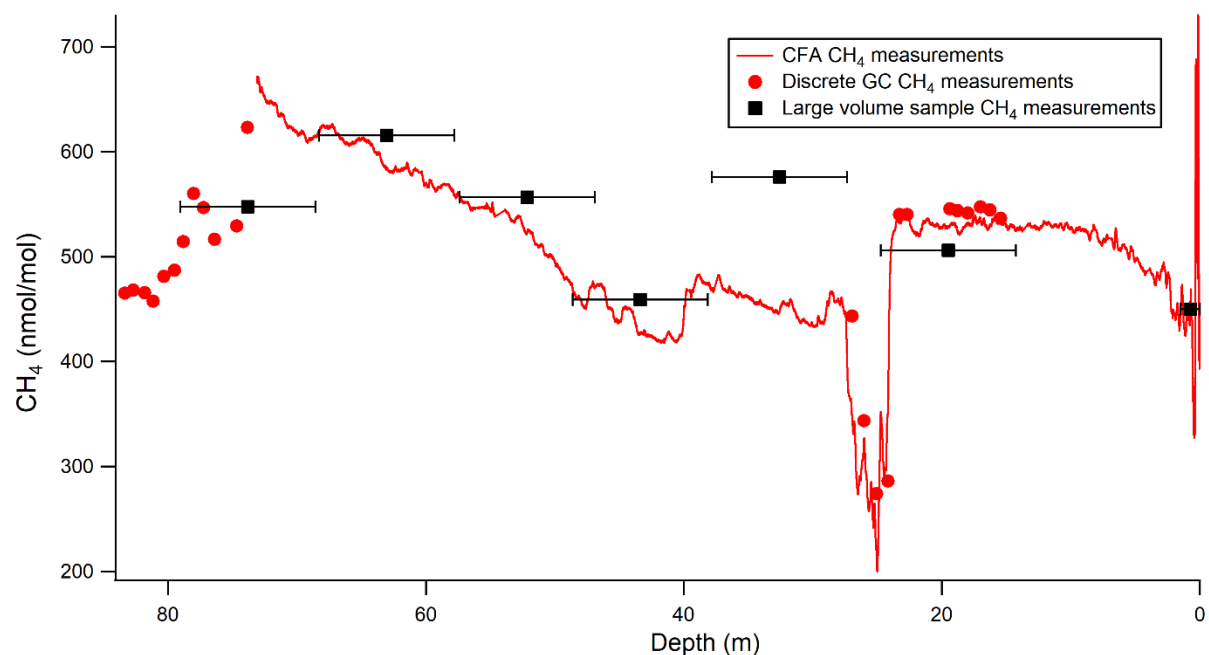
Fig. S11. Depth profile of "TG-Deep3" [CH₄] measurements from CFA, discrete measurements using a GC-FID system, and [CH₄] measurements from large volume samples. The large volume samples combine ice from all three 2015/16 deep boreholes. The horizontal error bars illustrate the depth span of the large volume samples.
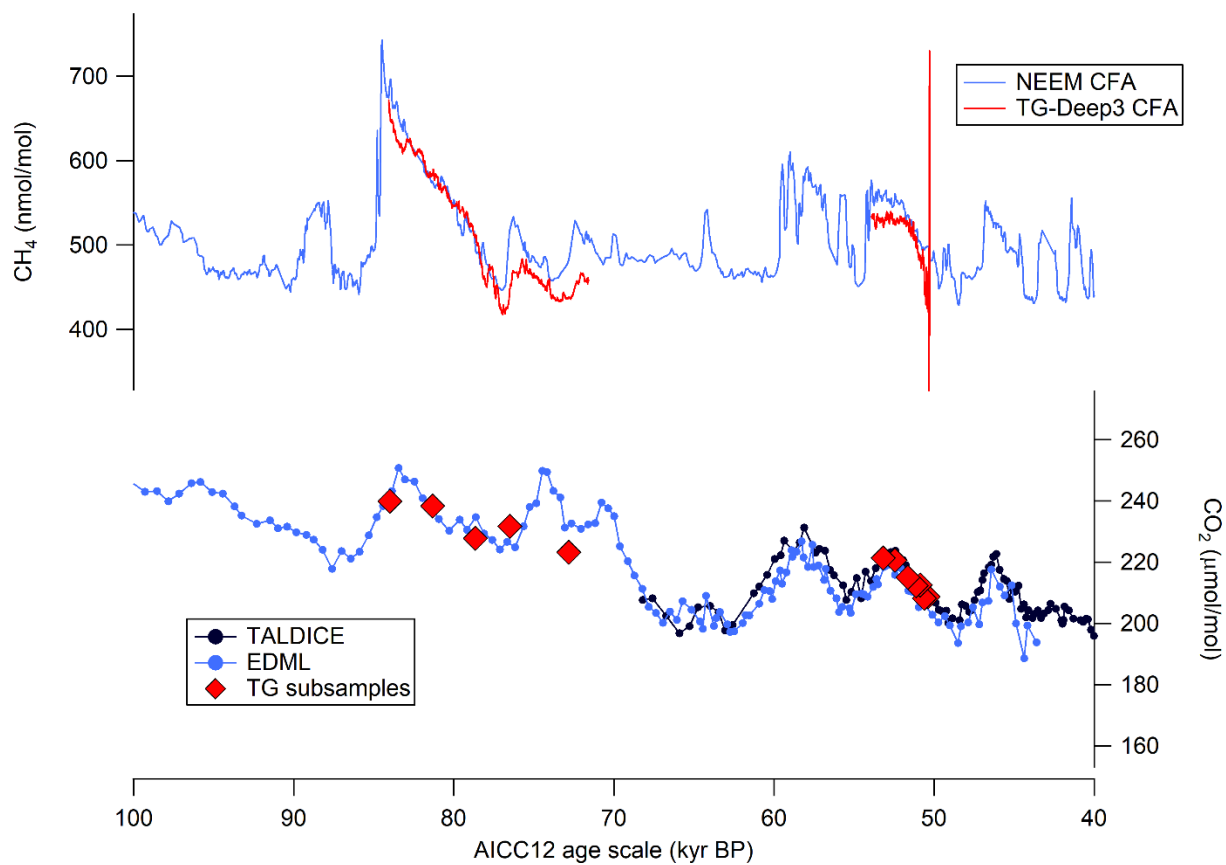
Fig. S12. Continuous flow analysis (CFA) [CH₄] from "TG-Deep3" core (this study), CFA [CH₄] mole fraction from NEEM (Chappellaz et al., 2013), [CO₂] from $^{14}CO_2$ samples used in this study, and composite Antarctic ice core [CO₂] (Bereiter et al., 2015). All data are plotted onto the synchronized AICC12 gas age (Veres et al., 2013).
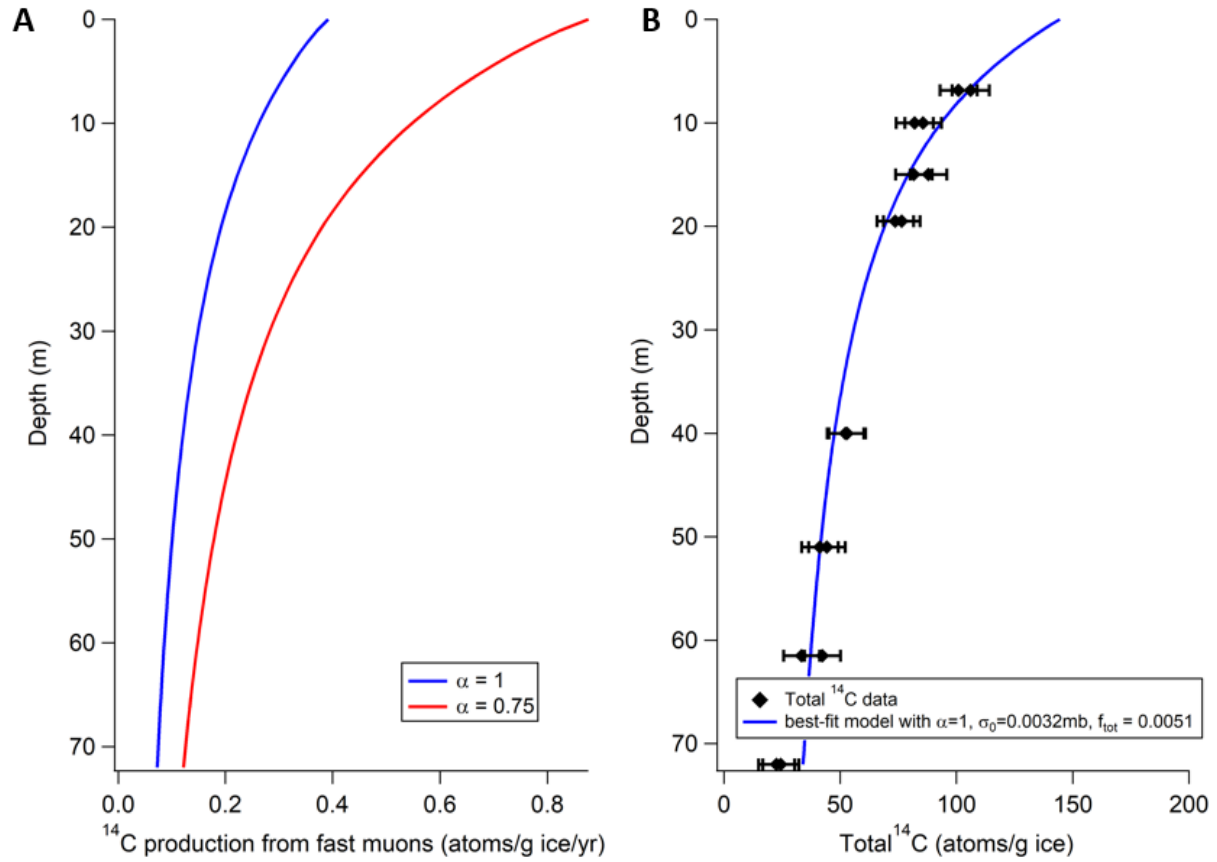
Fig. S12. (A). ^{14}C production rate from fast muons with default α = 0.75 (blue) and α = 1 (red). **(B).** Total ^{14}C data and best-fit model with α = 1.

Table S1. δ¹³C measurements on the large volume samples. All errors presented indicate the 95% confidence interval.

Sample name	δ¹³CH₄ (‰)
Sfc sample	-34.7 ± 0.2
19.5m	-45.1 ± 0.2
30m	-46.8 ± 0.2
40.5m	-47.9 ± 0.2
51m	-48.1 ± 0.2
61.5m	-47.9 ± 0.2
72m	-47.2 ± 0.2

Table S2. Measured CH₄ mole fraction in the large volume samples, field procedural blanks, and associated corrections. All errors presented indicate the 95% confidence interval.

| Sample name	CH₄ measured (nmol/mol)	CH₄ solubility correction factor	CH₄ solubility corrected (nmol/mol)	Fraction ultrapure air remaining	Final CH₄* (nmol/mol)
SFC	433.7 ± 0.6	1.034 ± 0.007	448.4 ± 3.0		442.3 ± 3.9
19.5m	495.6 ± 0.4	1.030 ± 0.006	510.2 ± 2.9		504.2 ± 3.9
30m	564.5 ± 0.3	1.028 ± 0.005	580.2 ± 3.1		574.2 ± 4.0
40.5m	450.6 ± 0.6	1.029 ± 0.006	463.5 ± 2.6		457.5 ± 3.7
51m	544.1 ± 0.3	1.030 ± 0.006	560.5 ± 3.3		554.5 ± 4.2
61.5m	600.5 ± 0.5	1.031 ± 0.006	619.1 ± 3.7		613.1 ± 4.5
72m	532.3 ± 0.7	1.035 ± 0.007	551.0 ± 3.8		545.0 ± 4.7
¹⁴C dead blank 1	461.9 ± 0.4	1.036 ± 0.007	478.6 ± 3.3	0.0306 ± 0.0253	493.8 ± 13.4
¹⁴C dead blank 2	463.4 ± 0.3	1.035 ± 0.007	479.6 ± 3.2	0.0307 ± 0.0256	494.9 ± 13.5
¹⁴C modern blank 1	462.3 ± 0.3	1.034 ± 0.007	478.1 ± 3.1	0.0201 ± 0.0018	487.9 ± 3.3
¹⁴C modern blank 2	452.8 ± 0.4	1.030 ± 0.006	466.5 ± 2.7	0.0415 ± 0.0139	486.7 ± 7.6
¹⁴C dead std gas	498.3 ± 4.6				
¹⁴C modern std gas	492.8 ± 3.5				

the CH₄ mole fraction in the ice samples was further corrected for the 6.0±1.3 nmol/mol melting blank. The numbers shown here include the melting blank correction

Table S3. Pressure measurements and total air content (TAC) for the large volume samples. All errors presented indicate the 95% confidence interval. For the "30m" sample (marked with an asterisk*), the water level (and thus water volume) was not recorded for 1 (out of 3) melt-extractions. We thus assumed that the water volume for this extraction was equal to the average of all the other extractions for the field season and doubled the uncertainty. We used the SIO pressure measurements for TAC calculation, except for the "51m" sample (marked with two asterisks **) where UR pressure measurement is higher than the SIO pressure measurement, indicating a problem with the recorded SIO measurement. From the average pressure measurement differences within tanks, we assumed that the GC-MS and noble gas measurements at SIO consumed 221 ± 14 torr (95% CI), and used the UR pressure measurement, corrected for sample consumption at SIO, to calculate the TAC. All pressure measurements were taken at room temperature. On average (n=7), the SIO room temperature was 22.0 ± 0.1 °C and the UR room temperature was 21.7 ± 0.2 °C.

Sample name	SIO pressure corrected for vapor pressure (torr)	UR pressure corrected for vapor pressure (torr)	Pressure difference (SIO-UR) (torr)	Pressure used for air content calculation (torr)	Volume of air extracted (L STP)	Fraction of air in the headspace	Volume of ice extracted (water equivalent, L)	Total air content (cc STP / g ice)
SFC	2533 ± 20	2306 ± 18	227 ± 27	2533 ± 20	117.4 ± 3.9	0.956 ± 0.008	1188 ± 45	0.0989 ± 0.0050
19.5m	2156 ± 17	1927 ± 15	229 ± 23	2156 ± 17	99.7 ± 3.2	0.960 ± 0.007	1168 ± 45	0.0855 ± 0.0043
30m	2325 ± 19	2109 ± 17	216 ± 25	2325 ± 19	107.1 ± 3.5	0.962 ± 0.007	1154 ± 69*	0.0930 ± 0.0064
40.5m	2316 ± 19	2107 ± 17	209 ± 25	2316 ± 19	106.9 ± 3.5	0.961 ± 0.007	1160 ± 44	0.0922 ± 0.0046
51m	*2146 ± 17*	*2227 ± 18*	*-81 ± 25***	*2448 ± 35***	109.3 ± 4.6	0.960 ± 0.007	1163 ± 45	0.0941 ± 0.0054
61.5m	2391 ± 19	2171 ± 17	219 ± 26	2391 ± 19	110.5 ± 3.6	0.959 ± 0.008	1170 ± 45	0.0946 ± 0.0047
72m	2513 ± 20	2289 ± 18	224 ± 27	2513 ± 20	116.6 ± 3.9	0.954 ± 0.008	1193 ± 46	0.0979 ± 0.0050
		Average (n = 6)	221					
		2x standard deviations	14					

Table S4. Measurement of noble gases (δXe/N₂, δKr/N₂, and δXe/Kr) from the field procedural blanks. The large-volume samples are affected by anomalously increased gas solubility relative to the actual measured headspace pressure (P_{head}) due to rising gas bubbles during ice melting and the air recirculation step (which effectively increases the pressure of gas, $P_{exchange}$; see Petrenko et al., 2016). To constrain gas solubility, the ^{14}C-modern standard used in the field procedural blanks was spiked with artificially high Xe and Kr (Dyonisius et al., 2020). We measured the two field procedural blank samples (which undergo a similar air recirculation step as the samples) derived from this standards gas for δXe/N₂, δKr/N₂, and δXe/Kr relative to the standard gas and estimated the parameter alpha (α), which effectively accounts for the ratio of $P_{exchange}/P_{head}$. Alpha (α) is chosen to minimize the discrepancy between expected δXe/Kr vs. measured δXe/Kr for both modern ^{14}C field procedural blank samples.

Sample name	Field ^{14}C modern test 1	Field ^{14}C modern test 2
Tank #	SIO15	SIO18
δ(Xe/N₂), ‰ vs. CB10270 (modern ^{14}C std)	-202.1	-210.3
δ(Kr/N₂), ‰ vs. CB10270 (modern ^{14}C std)	-95.0	-131.5
δ(Xe/Kr), ‰ vs. CB10270 (modern ^{14}C std)	-95.0	-90.7
Constants and physical measurements for gas solubility calculation		
Water T during recirculation, K	282.3	279.6
Kr solubility constant (K_h) @ water T, M/atm	0.003573991	0.003820178
Xe solubility constant (K_h) @ water T, M/atm	0.006504131	0.007025663
Headspace volume, L	400	371
Headspace T, K	270	299
Mole fraction under Henry's Law		
Mole fraction of Xe in water	0.182	0.167
Mole fraction of Xe in headspace	0.818	0.833
Mole fraction of Kr in water	0.109	0.098
Mole fraction of Kr in headspace	0.891	0.902
δ(Xe/Kr) predicted under full eq, ‰	-82.0	-76.0
Mole fraction under increased gas solubility due to recirculation step		
α, tuneable parameter for $P_{exchange}/P_{head}$	1.221	1.221
Mole fraction of Xe in water, with α	0.214	0.196
Mole fraction of Xe in headspace, with α	0.786	0.804
Mole fraction of Kr in water, with α	0.130	0.117
Mole fraction of Kr in headspace, with α	0.870	0.883
d(Xe/Kr) tuned with α, ‰	-96.2	-89.5
δ(Xe/Kr) final offset with tuned α vs. measured, ‰	1.224	-1.230

Table S5. CO mole fraction, [14]CO measurements, and estimates of in-situ cosmogenic [14]CO content in the large volume samples and field procedural blanks. All errors presented indicate the 95% confidence interval

Sample name	CO measured (nmol/mol)	[14]CO measured (pMC)	[14]CO corrected for dilution with 10 µmol/mol [CO] ^{14}C-depleted gas		[14]CO corrected for procedural blanks (molec/cc STP)	Cosmogenic [14]CO after corrections (molec/per g ice)**
			(pMC)	(molec/cc STP)		
SFC	166.3 ± 5.9	88.1 ± 2.0	7541 ± 383	394.5 ± 14.2	371.3 ± 14.7	36.7 ± 2.3
19.5m	166.7 ± 5.8	67.0 ± 0.8	5732 ± 266	300.5 ± 9.2	277.3 ± 9.7	23.7 ± 1.4
30m	2149.1 ± 5.9	60.9 ± 0.9	415 ± 12	280.6 ± 8.3	257.4 ± 8.8	23.9 ± 1.8
40.5m	179.8 ± 5.8	35.0 ± 0.5	3419 ± 156	193.4 ± 6.2	170.2 ± 6.9	15.7 ± 1.0
51m	208.0 ± 5.9	98.8 ± 1.0	2485 ± 96	162.6 ± 4.5	139.4 ± 5.5	13.1 ± 0.9
61.5m	117.8 ± 5.9	88.5 ± 1.0	3835 ± 216	142.0 ± 4.0	118.9 ± 5.1	11.2 ± 0.7
72m	110.0 ± 5.8	82.7 ± 0.9	3845 ± 227	133.0 ± 3.8	109.8 ± 5.0	10.7 ± 0.7
[14]C dead blank 1	40.1 ± 6.0	19.0 ± 0.5	1919 ± 294	24.1 ± 0.9		
[14]C dead blank 2	41.7 ± 5.8	16.3 ± 0.3	1562 ± 226	20.4 ± 0.7		
[14]C modern blank 1	40.1 ± 5.9	19.0 ± 0.4	1774 ± 272	22.2 ± 0.8		
[14]C modern blank 2	42.0 ± 5.9	8.9 ± 0.2	1758 ± 261	23.1 ± 1.1		
[14]C dead dilution gas	10020 ± 130	0.17 ± 0.6				

this sample yielded an anomalously high CO mole fraction, indicating some form of contamination
**includes the solubility correction for CO mole fraction because CO is slightly more soluble than air*

Table S6. [14]CH_4 corrections for the large volume samples. All errors presented indicate the 95% confidence interval.

Sample name	Measured [14]CH_4 (pMC)	[14]CH_4 corrected for processing blanks (pMC)	[14]CH_4 corrected for processing blanks (molec/cc STP)	[14]CH_4 amount per gram ice (molec/g ice)
Sfc sample	61.1 ± 2.2	62.7 ± 2.5	8.555 ± 0.357	0.840 ± 0.054
19.5m	15.4 ± 0.6	15.4 ± 0.7	2.270 ± 0.144	0.193 ± 0.016
30m	13.9 ± 0.6	13.9 ± 0.7	2.322 ± 0.152	0.214 ± 0.020
40.5m	10.1 ± 0.4	9.9 ± 0.5	1.284 ± 0.122	0.118 ± 0.013
51m	7.0 ± 0.5	6.7 ± 0.5	1.031 ± 0.133	0.096 ± 0.013
61.5m	5.4 ± 0.4	5.0 ± 0.5	0.831 ± 0.127	0.078 ± 0.013
72m	5.9 ± 0.4	5.5 ± 0.5	0.817 ± 0.124	0.079 ± 0.013
[14]C dead blank 1	0.8 ± 0.1			
[14]C dead blank 2	1.0 ± 0.1			
[14]C modern blank 1	132.9 ± 1.6			
[14]C modern blank 2	132.5 ± 1.6			
[14]C dead "true"	0.31 ± 0.03			
[14]C modern "true"	137.2 ± 1.4			

Table S7. Measured ^{14}C activities of commensurately-sized ^{14}C standards and their expected ^{14}C activities. The 50µg and standard 15µg set are used to empirically correct the ^{14}CO and $^{14}CO_2$ sample pMC values, respectively (Fig. S1a and S1b). The measured ^{14}C activities are corrected for $\delta^{13}C$ and the errors represent 68% (1σ) confidence interval. The expected ^{14}C activity of the OxII standard is based on consensus value reported by Wacker et al. (2019). The expected ^{14}C activities of the IAEA-C7 and C8 standard are based on values reported by Le Clercq et al. (1997). Finally, the expected ^{14}C activities of ANSTO internal "dead CO_2" and L733 standard are based on large (1mg) samples graphitized with the ANSTO conventional furnaces (Hua et al., 2004).

Sample name	Measured ^{14}C activity (pMC)	Error (pMC)	Expected ^{14}C activity (pMC)	Error (pMC)
50 µg set (^{14}CO sample set)				
Dead CO2	0.20	0.03		
Dead CO2	0.15	0.03	0.03	0.02
Dead CO2	0.17	0.03		
STD OxII	134.90	0.48		
STD OxII	133.31	0.61	134.06	0.08
STD OxII	134.93	0.60		
IAEA-C7	49.89	0.29	49.53	0.24
IAEA-C7	50.09	0.33		
STD L733	86.83	0.36	86.27	0.53
STD L733	87.51	0.43		
15 µg set ($^{14}CO_2$ sample set)				
Dead CO2	0.41	0.05		
Dead CO2	0.45	0.20	0.03	0.02
Dead CO2	0.36	0.11		
Dead CO2	0.40	0.06		
STD OxII	134.96	0.85		
STD OxII	134.54	0.82	134.06	0.08
STD OxII	133.23	0.80		
STD OxII	133.33	0.72		
IAEA-C7	49.99	0.47	49.53	0.24
IAEA-C8	14.99	0.27	15.03	0.34
STD L733	83.81	0.55	86.27	0.53

Table S8. $^{14}CO_2$ measurements on laboratory-made bubble-free ice (BFI) samples, including measured ^{14}C, ^{14}C corrected for ANSTO processing, measured carbon mass (M_g), expected carbon mass (M_s), extraneous carbon mass (M_{ext}), and calculated ^{14}C activity of extraneous carbon. The "true" $^{14}CO_2$ activities for the standard gases are 102.48 ± 0.42 and 0.38 ± 0.06 pMC for the "modern" and "dead" standards respectively. All errors presented indicate the 95% confidence interval.

Standard gas used	Measured $^{14}CO_2$	$^{14}CO_2$ corrected for ANSTO processing ($^{14}C_g$)	M_g	M_s	M_{ext}	^{14}C activity of extraneous C ($^{14}C_{ext}$)
	(pMC)	(pMC)	(µg)	(µg)	(µg)	(pMC)
Modern	102.5 ± 1.6	102.7 ± 2.2	12.3 ± 0.2	11.8 ± 0.2	0.5 ± 0.3	108.5 ± 141.2
Modern	103.0 ± 1.4	103.2 ± 2.0	12.0 ± 0.2	11.7 ± 0.2	0.3 ± 0.3	130.8 ± 222.5
Modern	104.7 ± 1.4	104.9 ± 2.0	11.9 ± 0.2	11.6 ± 0.2	0.3 ± 0.3	198.3 ± 268.4
Dead	3.9 ± 0.4	3.7 ± 1.0	11.7 ± 0.2	11.4 ± 0.2	0.3 ± 0.3	111.9 ± 105.7
Dead	3.8 ± 0.4	3.6 ± 1.0	13.3 ± 0.2	13.0 ± 0.3	0.4 ± 0.3	122.9 ± 127.0
Dead	3.2 ± 0.4	3.0 ± 1.0	13.5 ± 0.2	13.2 ± 0.3	0.3 ± 0.3	116.4 ± 140.3
Dead	3.2 ± 0.3	3.0 ± 1.0	13.1 ± 0.2	12.7 ± 0.3	0.3 ± 0.3	104.7 ± 114.9
Modern	100.7 ± 1.3	101.0 ± 1.9	14.2 ± 0.2	13.9 ± 0.2	0.4 ± 0.3	44.2 ± 163.2
Modern	103.6 ± 1.5	103.9 ± 2.1	12.0 ± 0.2	11.8 ± 0.2	0.2 ± 0.3	195.0 ± 461.3
				Average (n=9)		125.9
				Standard deviation		94.2
				Standard error		31.4

Table S9. $^{14}CO_2$ measurements, CO_2 mole fraction measurements, total air content (TAC), corrections, and error-propagated uncertainties. Most samples, with the exception of the ones with *next to their depths were collected from 2015/16 deep borehole #2. All errors presented indicate the 95% confidence interval.

Depth	Measured ^{14}C	CO_2 mole fraction	^{14}C corrected for ANSTO processing ($^{14}C_g$)	Measured mass (M_g)	Expected mass (M_s)	Extraneous mass M_{ext}	^{14}C corrected for extraneous C ($^{14}C_s$)		Total air content	^{14}C corrected for postcoring ^{14}C production
(m)	(pMC)	(nmol/mol)	(pMC)	(µg)	(µg)	(µg)	(pMC)	(molec/g ice)	cc STP/g ice	(molec/g ice)
2.25	31.0 ± 0.8	208.69 ± 1.81	30.9 ± 1.2	13.1 ± 0.2	12.6 ± 0.4	0.5 ± 0.5	27.1 ± 5.1	153.7 ± 29.0	0.0839 ± 0.0005	145.5 ± 32.0
2.25	27.6 ± 1.2		27.5 ± 1.5	12.6 ± 0.2	12.0 ± 0.3	0.5 ± 0.4	23.2 ± 4.4	131.4 ± 24.9		123.3 ± 28.5
3.65	19.4 ± 0.7	208.19 ± 1.81	19.3 ± 1.1	13.6 ± 0.2	13.0 ± 0.3	0.6 ± 0.4	14.3 ± 4.3	96.7 ± 28.8	0.1001 ± 0.0007	88.5 ± 31.9
3.65	18.9 ± 0.9		18.7 ± 1.2	13.3 ± 0.2	13.0 ± 0.3	0.4 ± 0.4	15.7 ± 4.1	106.2 ± 27.9		98.0 ± 31.1
5.25	17.8 ± 0.7	212.56 ± 1.81	17.7 ± 1.1	13.3 ± 0.2	12.9 ± 0.3	0.4 ± 0.4	14.0 ± 4.1	98.8 ± 28.6	0.1022 ± 0.0007	90.6 ± 31.8
5.25	18.4 ± 0.6		18.3 ± 1.0	13.8 ± 0.2	13.3 ± 0.3	0.5 ± 0.4	14.6 ± 4.1	103.0 ± 28.8		94.8 ± 31.9
6.85	14.2 ± 0.7	212.31 ± 1.81	14.1 ± 1.1	12.7 ± 0.2	12.3 ± 0.3	0.4 ± 0.4	10.4 ± 4.1	72.4 ± 28.3	0.1015 ± 0.0004	64.2 ± 31.6
6.85	14.4 ± 0.6		14.2 ± 1.0	12.8 ± 0.2	12.5 ± 0.3	0.3 ± 0.4	11.1 ± 4.0	77.6 ± 28.1		69.4 ± 31.3
10	13.4 ± 0.6	214.98 ± 1.81	13.3 ± 1.0	12.8 ± 0.2	12.4 ± 0.3	0.5 ± 0.4	8.9 ± 4.1	58.8 ± 26.9	0.0946 ± 0.0004	50.6 ± 30.3
10	13.2 ± 0.7		13.1 ± 1.1	13.0 ± 0.2	12.6 ± 0.3	0.4 ± 0.4	9.5 ± 4.1	62.5 ± 26.7		54.3 ± 30.0
15*	13.7 ± 0.8	220.65 ± 1.81	13.6 ± 1.2	11.6 ± 0.2	11.2 ± 0.3	0.3 ± 0.3	10.2 ± 4.0	69.1 ± 27.4	0.0952 ± 0.0007	60.9 ± 30.7
15*	12.2 ± 0.6		12.0 ± 1.0	10.3 ± 0.2	10.1 ± 0.2	0.2 ± 0.3	9.2 ± 3.9	62.8 ± 26.7		54.6 ± 30.2
19.5	12.0 ± 0.5	221.37 ± 1.81	11.9 ± 1.0	10.7 ± 0.2	10.6 ± 0.2	0.1 ± 0.3	10.3 ± 3.9	60.5 ± 22.9	0.0821 ± 0.0004	52.4 ± 26.6
19.5	11.8 ± 0.7		11.6 ± 1.1	11.9 ± 0.2	11.7 ± 0.3	0.2 ± 0.3	9.8 ± 3.9	57.8 ± 22.9		49.6 ± 26.7
30**	13.1 ± 0.6	223.22 ± 1.81	12.9 ± 1.0	13.9 ± 0.2	13.6 ± 0.5	0.3 ± 0.6	10.2 ± 5.8	67.4 ± 38.3	0.0918 ± 0.0007	59.2 ± 40.8
40.5	9.0 ± 0.5	231.71 ± 1.81	8.8 ± 1.0	11.8 ± 0.2	11.6 ± 0.3	0.2 ± 0.3	6.7 ± 4.0	44.6 ± 26.5	0.0887 ± 0.0007	36.4 ± 29.9
40.5	10.4 ± 0.5		10.3 ± 1.0	12.3 ± 0.2	11.9 ± 0.3	0.4 ± 0.3	6.8 ± 3.9	45.4 ± 26.0		37.2 ± 29.5
51	8.7 ± 0.5	227.75 ± 1.81	8.5 ± 1.0	13.2 ± 0.2	12.9 ± 0.3	0.3 ± 0.4	5.5 ± 3.9	39.3 ± 27.7	0.0965 ± 0.0002	31.1 ± 30.9
51*	8.5 ± 0.7	229.17 ± 1.81	8.3 ± 1.1	14.5 ± 0.2	14.1 ± 0.3	0.4 ± 0.4	5.2 ± 3.9	36.2 ± 27.4	0.0940 ± 0.0004	28.0 ± 30.6
61.5	8.2 ± 0.4	239.82 ± 1.81	8.1 ± 0.9	14.3 ± 0.2	14.0 ± 0.3	0.3 ± 0.4	5.2 ± 3.8	39.2 ± 28.5	0.0961 ± 0.0005	31.0 ± 31.8
61.5*	7.4 ± 0.4	238.35 ± 1.81	7.3 ± 0.9	14.2 ± 0.2	13.8 ± 0.3	0.3 ± 0.4	4.3 ± 3.8	30.3 ± 27.0	0.0918 ± 0.0002	22.1 ± 30.3
72	7.2 ± 0.4	239.92 ± 1.81	7.0 ± 0.9	12.4 ± 0.2	12.0 ± 0.3	0.4 ± 0.3	2.7 ± 3.9	20.0 ± 29.2	0.0960 ± 0.0003	11.8 ± 32.4
72	7.0 ± 0.4		6.8 ± 0.9	13.4 ± 0.2	13.0 ± 0.3	0.4 ± 0.4	2.9 ± 3.9	21.7 ± 29.0		13.6 ± 32.1

*these samples were collected from borehole #3

**replicate sample was lost

Table S10. $^{14}CO_2$ **measurements corrected for ANSTO processing, CO_2 mole fraction, and "total air content" of the laboratory-produced and field-produced BFI samples that were run with the ^{14}C-dead standard.** The CO_2 mole fraction in the BFI samples was determined from the ratio of the amount of CO_2 and air collected, measured in the manometers. The "air content" of the BFI samples was determined from the ratio of the amount of air collected in the manometer and the amount of bubble-free-ice sublimated. All errors presented indicate the 95% confidence interval.

Sample Name	^{14}C corrected for ANSTO processing (pMC)	CO_2 mole fraction (μmol/mol)	"Air content" (ccSTP/g ice)	$^{14}CO_2$ content (molecule/g ice)
Field#1	3.8 ± 0.5	308.3 ± 4.0	0.096 ± 0.007	34.5 ± 11.6
Field#5	2.5 ± 0.5	306.7 ± 4.0	0.100 ± 0.007	23.4 ± 10.6
Field#4	4.3 ± 0.6	308.9 ± 4.0	0.074 ± 0.007	30.5 ± 10.0
Field#2	4.2 ± 0.5	313.0 ± 4.1	0.074 ± 0.007	30.1 ± 9.4
Lab#5	3.7 ± 0.5	310.8 ± 4.1	0.071 ± 0.007	24.8 ± 8.7
Lab#6	3.6 ± 0.5	309.8 ± 4.0	0.070 ± 0.007	24.1 ± 8.4
Lab#8	3.0 ± 0.5	308.6 ± 4.0	0.070 ± 0.007	19.9 ± 7.9
Lab#9	3.0 ± 0.5	309.4 ± 4.0	0.059 ± 0.007	16.9 ± 6.5
Average field ± stdev				**29.7 ± 4.6**
Average lab ± stdev				**21.4 ± 3.7**
Average postcoring ± stdev				**8.2 ± 5.9**

REFERENCES

Baggenstos, D., Bauska, T. K., Severinghaus, J. P., Lee, J. E., Schaefer, H., Buizert, C., Brook, E. J., Shackleton, S., and Petrenko, V. V.: Atmospheric gas records from Taylor Glacier, Antarctica, reveal ancient ice with ages spanning the entire last glacial cycle, 13, 943, 2017.

Balco, G., Stone, J. O., Lifton, N. A., and Dunai, T. J.: A complete and easily accessible means of calculating surface exposure ages or erosion rates from 10Be and 26Al measurements, 3, 174–195, 2008.

Bereiter, B., Eggleston, S., Schmitt, J., Nehrbass-Ahles, C., Stocker, T. F., Fischer, H., Kipfstuhl, S., and Chappellaz, J.: Revision of the EPICA Dome C CO2 record from 800 to 600 kyr before present, Geophys. Res. Lett., 42, 2014GL061957, https://doi.org/10.1002/2014GL061957, 2015.

Chappellaz, J., Stowasser, C., Blunier, T., Baslev-Clausen, D., Brook, E. J., Dallmayr, R., Faïn, X., Lee, J. E., Mitchell, L. E., and Pascual, O.: High-resolution glacial and deglacial record of atmospheric methane by continuous-flow and laser spectrometer analysis along the NEEM ice core, 9, 2579–2593, 2013.

Clercq, M. L., Plicht, J. V. D., and Gröning, M.: New 14C Reference Materials with Activities of 15 and 50 pMC, 40, 295–297, https://doi.org/10.1017/S0033822200018178, 1997.

Hua, Q., Zoppi, U., Williams, A. A., and Smith, A. M.: Small-mass AMS radiocarbon analysis at ANTARES, Nuclear Instruments and Methods in Physics Research Section B: Beam Interactions with Materials and Atoms, 223–224, 284–292, https://doi.org/10.1016/j.nimb.2004.04.057, 2004.

Loulergue, L., Schilt, A., Spahni, R., Masson-Delmotte, V., Blunier, T., Lemieux, B., Barnola, J.-M., Raynaud, D., Stocker, T. F., and Chappellaz, J.: Orbital and millennial-scale features of atmospheric CH4 over the past 800,000 years, 453, 383, 2008.

McNaught, A. D. and Wilkinson, A.: Compendium of chemical terminology, Blackwell Science Oxford, 1997.

Mitchell, L., Brook, E., Lee, J. E., Buizert, C., and Sowers, T.: Constraints on the Late Holocene Anthropogenic Contribution to the Atmospheric Methane Budget, *Science*, **342**, 964–966, 2013.

Menking, J. A., Brook, E. J., Shackleton, S. A., Severinghaus, J. P., Dyonisius, M. N., Petrenko, V., McConnell, J. R., Rhodes, R. H., Bauska, T. K., and Baggenstos, D.: Spatial pattern of accumulation at Taylor Dome during Marine Isotope Stage 4: stratigraphic constraints from Taylor Glacier, *Clim. Past.*, **15**, 1537–1556, 2019.

Mitchell, L. E., Brook Edward J., Sowers Todd, McConnell J. R., and Taylor Kendrick: Multidecadal variability of atmospheric methane, 1000–1800 C.E., Journal of Geophysical Research: Biogeosciences, 116, https://doi.org/10.1029/2010JG001441, 2011.

Petrenko, V. V., Severinghaus, J. P., Brook, E. J., Reeh, N., and Schaefer, H.: Gas records from the West Greenland ice margin covering the Last Glacial Termination: a horizontal ice core,

Quaternary Science Reviews, 25, 865–875, https://doi.org/10.1016/j.quascirev.2005.09.005, 2006.

Petrenko, V. V., Smith, A. M., Brailsford, G., Riedel, K., Hua, Q., Lowe, D., Severinghaus, J. P., Levchenko, V., Bromley, T., Moss, R., Mühle, J., and Brook, E. J.: A New Method for Analyzing 14C of Methane in Ancient Air Extracted from Glacial Ice, 50, 53–73, https://doi.org/10.2458/azu_js_rc.50.3033, 2008.

Petrenko, V. V., Severinghaus, J. P., Schaefer, H., Smith, A. M., Kuhl, T., Baggenstos, D., Hua, Q., Brook, E. J., Rose, P., Kulin, R., Bauska, T., Harth, C., Buizert, C., Orsi, A., Emanuele, G., Lee, J. E., Brailsford, G., Keeling, R., and Weiss, R. F.: Measurements of 14C in ancient ice from Taylor Glacier, Antarctica constrain in situ cosmogenic 14CH4 and 14CO production rates, Geochimica et Cosmochimica Acta, 177, 62–77, https://doi.org/10.1016/j.gca.2016.01.004, 2016.

Rasmussen S. O., Andersen K. K., Svensson A. M., Steffensen J. P., Vinther B. M., Clausen H. B., Siggaard-Andersen M.-L., Johnsen S. J., Larsen L. B., Dahl-Jensen D., Bigler M., Röthlisberger R., Fischer H., Goto-Azuma K., Hansson M. E., and Ruth U.: A new Greenland ice core chronology for the last glacial termination, Journal of Geophysical Research: Atmospheres, 111, https://doi.org/10.1029/2005JD006079, 2006.

Rasmussen, S. O., Abbott, P. M., Blunier, T., Bourne, A. J., Brook, E., Buchardt, S. L., Buizert, C., Chappellaz, J., Clausen, H. B., Cook, E., Dahl-Jensen, D., Davies, S. M., Guillevic, M., Kipfstuhl, S., Laepple, T., Seierstad, I. K., Severinghaus, J. P., Steffensen, J. P., Stowasser, C., Svensson, A., Vallelonga, P., Vinther, B. M., Wilhelms, F., and Winstrup, M.: A first chronology for the North Greenland Eemian Ice Drilling (NEEM) ice core, Clim. Past, 9, 2713–2730, https://doi.org/10.5194/cp-9-2713-2013, 2013.

Turney, C., Fogwill, C., Van Ommen, T. D., Moy, A. D., Etheridge, D., Rubino, M., Curran, M. A., and Rivera, A.: Late Pleistocene and early Holocene change in the Weddell Sea: a new climate record from the Patriot Hills, Ellsworth Mountains, West Antarctica, 28, 697–704, 2013.

Shackleton, S., Baggenstos, D., Menking, J. A., Dyonisius, M. N., Bereiter, B., Bauska, T. K., Rhodes, R. H., Brook, E. J., Petrenko, V. V., McConnell, J. R., Kellerhals, T., Häberli, M., Schmitt, J., Fischer, H., and Severinghaus, J. P.: Global ocean heat content in the Last Interglacial, *Nat. Geosci.*, **13**, 77–81, 2020.

van De Wal, R. S. W., Meijer, H. a. J., De Rooij, M., and Van Der Veen, C.: Radiocarbon analyses along the EDML ice core in Antarctica, *Tellus. B,* **59**, 157–165, 2007.

van der Kemp, W. J. M., Alderliesten, C., Van der Borg, K., Holmlund, P., de Jong, A. F. M., Karlöf, L., Lamers, R. A. N., Oerlemans, J., Thomassen, M., and Van de Wal, R. S. W.: Very little in situ produced radiocarbon retained in accumulating Antarctic ice, *Nucl. Instrum. Meth. B*, **172**, 632–636, 2000.

Veres, D., Bazin, L., Landais, A., Toyé Mahamadou Kele, H., Lemieux-Dudon, B., Parrenin, F., Martinerie, P., Blayo, E., Blunier, T., and Capron, E.: The Antarctic ice core chronology (AICC2012): an optimized multi-parameter and multi-site dating approach for the last 120 thousand years, 9, 1733–1748, 2013.

Wacker, L., Bollhalder, S., Sookdeo, A., and Synal, H.-A.: Re-evaluation of the New Oxalic Acid standard with AMS, Nuclear Instruments and Methods in Physics Research Section B: Beam Interactions with Materials and Atoms, 455, 178–180, https://doi.org/10.1016/j.nimb.2018.12.035, 2019.